SANDIA REPORT
SAND2009-8316
Unlimited Release
Printed December 2009

Analysis of Micromixers and Biocidal Coatings on Water-Treatment Membranes to Minimize Biofouling

Susan J. Altman, Malynda Cappelle, Paul G. Clem, Adam W. Cook, Christopher H. Cornelius, William E. Hart, Michael R. Hibbs, Clifford K. Ho, Howland D. T. Jones, Siri S. Khalsa, Rachel Noek, Amy C. Sun, Stephen W. Webb, Lucas K. McGrath, Andres Sanchez, Darryl L. James, Atar Adout, Menachem Elimelech, and Seokatae Kang

Prepared by
Sandia National Laboratories
Albuquerque, New Mexico 87185 and Livermore, California 94550

Sandia is a multiprogram laboratory operated by Sandia Corporation,
a Lockheed Martin Company, for the United States Department of Energy's
National Nuclear Security Administration under Contract DE–AC04–94AL85000.

Issued by Sandia National Laboratories, operated for the United States Department of Energy by Sandia Corporation.

Available to DOE and DOE contractors from
U.S. Department of Energy
Office of Scientific and Technical Information
P.O. Box 62
Oak Ridge, TN 37831

Telephone: (865)576–8401
Facsimile: (865)576–5728
E–Mail: reports@adonis.osti.gov
Online ordering: http://www.doe.gov/bridge

Available to the public from
U.S. Department of Commerce
National Technical Information Service
5285 Port Royal Rd
Springfield, VA 22161

Telephone: (800)553–6847
Facsimile: (703)605–6900
E–Mail: orders@ntis.fedworld.gov
Online order: http://www.ntis.gov/ordering.htm

SAND2009–8316
Unlimited Release
Printed December 2009

Analysis of Micromixers and Biocidal Coatings on Water-Treatment Membranes to Minimize Biofouling

Susan J. Altman[1], Malynda Cappelle[1], Paul G. Clem[2], Adam W. Cook[2], Christopher H. Cornelius[3], William E. Hart[4], Michael R. Hibbs[3], Clifford K. Ho[5], Howland D. T. Jones[6], Siri S. Khalsa[5], Rachel Noek[6], Amy C. Sun[5], Stephen W. Webb[7], Lucas K. McGrath[8], Andres Sanchez[8], Darryl L. James[9], Atar Adout[10], Menachem Elimelech[10], and Seokatae Kang[10]

[1]Geochemistry Department
[2]Ceramic Processing and Inorganic Materials Department
[3]Materials, Devices & Energy Technology Department
[4]Discrete Math and Complex Systems Department
[5]National Security Applications Department
[6]Bioenergy and Defense Technology Department
[7]Geotechnology & Engineering Department
Sandia National Laboratories
P.O. Box 5800
Albuquerque, NM 87185

[8]LMATA Government Services LLC
P.O. Box 5800, MS-0754
Albuquerque, NM 87185

[9]Department of Mechanical Engineering
Texas Tech University
Lubbock, TX 79409

[10]Environmental and Chemical Engineering Department
Yale University
New Haven, CT 06520

Abstract

Biofouling, the unwanted growth of biofilms on a surface, of water-treatment membranes negatively impacts in desalination and water treatment. With biofouling there is a decrease in permeate production, degradation of permeate water quality, and an increase in energy expenditure due to increased cross-flow pressure needed. To date, a universal successful and cost-effect method for controlling biofouling has not been implemented. The overall goal of the work described in this report was to use high-performance computing to direct polymer, material, and biological research to create the next generation of water-treatment membranes. Both physical (micromixers – UV-curable epoxy traces printed on the surface of a water-treatment membrane that promote chaotic mixing) and chemical (quaternary ammonium groups) modifications of the membranes for the purpose of increasing resistance to biofouling were evaluated. Creation of low-cost, efficient water-treatment membranes helps assure the availability of fresh water for human use, a growing need in both the U. S. and the world.

EXECUTIVE SUMMARY

Section 1: Biofouling, the unwanted growth of biofilms on a surface, of water-treatment membranes has a negative economic impact in desalination and water treatment. With biofouling there is a decrease in permeate production and an increase in energy expenditure due to increased cross-flow pressure needed. Biofouling leads to increased cleaning expenditures, it accelerates the degradation of the membranes, and degrades the water quality of the permeate. To date, a universal successful and cost-effect method for controlling biofouling has not been implemented. The goal of this project is to use high-performance computing to direct polymer, material, and biological research to create the next generation of water-treatment membranes. Both physical (micromixers – UV-curable epoxy traces printed on the surface of a water-treatment membrane that promote chaotic mixing) and chemical (quaternary ammonium groups) modifications of the membranes for the purpose of increasing resistance to biofouling were evaluated.

Section 2: Features (micromixers) that promote chaotic mixing were fabricated on reverse-osmosis membrane surfaces and evaluated using computational models and laboratory experiments to determine their effectiveness in reducing biofouling. Computational fluid dynamics models of membrane feed channels were developed using different patterns of micromixers on the membrane surface. The shear-stress distribution along the membrane surface was simulated for steady flows along the different micromixer configurations. In addition, the hypothetical mass transfer of a tracer from the membrane surface was used as a metric to compare the amount of scouring and mixing in configurations with and without micromixers. Epoxy micromixers were printed directly onto membrane surfaces, and different patterns were evaluated experimentally. Fluorescence hyperspectral imaging results showed that regions of simulated high shear stress on the membrane corresponded to regions of lower bacterial growth in the experiments, while regions of simulated low shear stress corresponded to regions of higher bacterial growth. In addition, the presence of the micromixers appeared to reduce the overall biofouling concentration in one series of experiments, but the results were inconclusive in another series of experiments. These results indicate that while the enhancement of mixing and shear stress via micromixers may delay or mitigate the onset of localized membrane fouling from biofilms or other contaminants, the impact of micromixers on the overall performance of reverse-osmosis membranes needs further investigation.

Section 3: Micromixers, UV-curable epoxy traces printed on the surface of a reverse osmosis membrane, were tested on a cross-flow system to determine their success at reducing biofouling. Biofouling was quantified by measuring the rate of permeate flux decline and the median bacteria concentration on the surface of the membrane (as determined by fluorescent intensity counts due to nucleic acid stains as measured by hyperspectral imaging). The micromixers do not appear to significantly increase the pressure needed to maintain the same initial permeate flux and salt rejection. Chevrons helped prevent biofouling of the membranes in comparison with blank membranes. The chevron design controlled where the bacteria adhered to the membrane surface. However, blank membranes with spacers had a lower rate of permeate flux decline than the membranes with chevrons despite having greater bacteria concentrations on their

surfaces. With better optimization of the micromixer design, the micromixers could be used to control where the bacteria will adhere to the surface and create a more biofouling resistant membrane that will help to drive down the cost of water treatment.

Section 4: A pilot-scale apparatus for testing small-scale spiral-wound membranes was built and successfully tested commercial membranes. This system can be used to not only test the membranes with micromixers, but also other novel membranes beyond this study. Spiral-wound membrane elements with two separate patterns of micromixers were built for testing in the pilot system. Unfortunately, the results were not as favorable as those tests run on commercial membranes. Salt rejection values were very low for the 5 non-commercial membrane elements, indicating a failure in the membrane. However, FD&C Blue Dye #2 was not visible in the permeate water stream. A more systematic study needs to be performed to determine at what step in the imprinting process the membranes fail (UV exposure, chevron printing, wrapping the membranes, etc.).

Section 5: A new concept for the modification of reverse osmosis (RO) membranes by coating the surface with a hydrophilic biocidal polymer is reported. The synthesis of a series of poly(sulfone)s with attached quaternary ammonium (QA) groups is described along with a method for spraying alcoholic solutions of the QA polymers to form water-permeable coatings. The hydrophilicity and surface charges of the coatings were measured by contact angle measurement and streaming potential analysis. Interaction forces between the coatings and a negatively charged particle probe were also investigated. Exposure of the coated membranes to suspensions of *E. coli* cells and subsequent testing for metabolic activity showed that all of the coatings exhibited significant biotoxictiy. Testing of coated RO membranes in a crossflow RO system showed increased biofilm growth on the coated membranes, presumably due to growth on top of a layer of dead cells that were in contact with the coating.

Section 6: A design analysis was conducted to optimize the shape of small protrusions (micromixers) fabricated on reverse-osmosis membranes with the objective of reducing biofouling by increasing the amount of turbulent mixing along the membrane surface. Micromixers have been experimentally and computationally shown to induce chaotic mixing and increase shear stress on the membrane surface. Computational fluid dynamics models of membranes imprinted with different micromixer patterns were developed to simulate the hydraulics and mass transfer within a membrane feed channel. The total simulated mass transfer of a tracer from the surface of the membrane and the pressure drop across the feed channel were used as metrics to compare the scouring effectiveness among the various micromixer patterns. The parameterization results indicate that the greatest scouring occurs when the chevron protrusion depth is maximized and the chevron pattern wavelength and spacing between chevrons are minimized. The same features that maximize scouring also increase the pressure drop. Operational factors and limitations need to be considered in real-world applications to maximize scouring while maintaining an acceptable pressure drop.

Section 7: The FLUENT computational fluid dynamics (CFD) code has been used to simulate membrane processes including water and salt flow across the membrane, concentration polarization, and particle trajectories. Simulation of these membrane processes with chevrons including detailed velocity and concentration fields is important to evaluating the change in membrane salt rejection due to these chevrons and as flow conditions for particle tracking

simulations. The biofouling potential is assumed to be related to the ability of particles to contact and stick to the membrane surface. The model successful ran simulating 0.25%, 2.3% and 4.6% of the particles trapped for cases with no chevrons, in-phase chevrons, and out-of-phase chevrons respectively. Patterns in particle trapping are not in agreement with those observed experimentally (Section 3). Additional forces that are not included in the present scheme but that might influence the results include turbulent deposition and modification of the drag parallel to the membrane surface due to the presence of a wall. In addition, the present model used a steady-state flow field to track the particles. Using a transient flow field would change the results due to the unsteady nature of turbulent flow. The inclusion of additional phenomena such as re-entrainment or resuspension would be expected to significantly improve the predictions.

Section 8: An automated search algorithm was developed for geometries that either maximizes fluid mixing while minimizing the area covered by the chevrons or maximizing the trans-membrane flux. The trade-off between the available membrane area for filtration and enhanced mass transfer due to the micromixers is evaluated by coupling the CFD model to an optimization algorithm. Two numerical studies were conducted, one two-dimensional (2D) and the second three-dimensions (3D). The objective of work is to demonstrate the coupling between a rigorous, parallel CFD analysis tool (Section 7) and a parallel optimization tool, which has not been carried out for this type of application. A complete, fully coupled run between the CFD models and the optimization code (DAKOTA) was automated. The potential for this application is high given the number of high-fidelity models Sandia create. In this study, point-by-point algorithm is used to seek the mixer geometry that maximizes salt rejection. A gradient-based algorithm is not recommended unless there is confidence that each search point generates an acceptable finite-element mesh. The geometry that yields the highest apparent salt rejection coefficient has parameters that reflect a high number of waves, large spacing, and small amplitude.

ACKNOWLEDGMENTS

This research was funded by the Sandia National Laboratories Laboratory Directed Research and Development (LDRD) program, Science Based Engineering and Technology and National Institute for NanoEngineering Investment Area. Menachem Elimelech, Mose Herzberg, and Atar Adout from Yale University are thanked for their advice in designing and conducting the experiments presented in Section 3. Laura Halbleib assisted with the Design of Experiments Analysis (Section 3).

This page is intentionally left blank

CONTENTS

ABSTRACT 3

EXECUTIVE SUMMARY 4

ACKNOWLEDGMENTS 7

TABLE OF CONTENTS 9

LIST OF TABLES 13

LIST OF FIGURES 15

1 INTRODUCTION 19

2 PRELIMINARY TESTING OF MICROMIXERS USING DRINKING WATER SOURCE OF BACTERIA 21

3 SYSTEMATIC ANALYSIS OF MICROMIXERS FOR MINIMIZING BIOFOULING ON REVERSE OSMOSIS MEMBRANES 31

3.1 Abstract 31

3.2 Introduction 31

3.3 Materials And Methods 32

3.3.1 Cultivation, Preparation And Enumeration Of Microorganisms 32

3.3.2 Micromixer Fabrication 33

3.3.3 Experimental Apparatus And Setup 33

3.3.4 Membrane Analysis 36

3.3.5 Data Analysis 37

3.4 Results 38

3.5 Discussion 42

3.6 Conclusions 44

3.7 REFERENCES 44

4 SCALE-UP OF MICROMIXERS TO SPIRAL-WOUND ELEMENTS 47

4.1 Introduction 47

4.2 Methods 47

4.2.1 Feedwater Preparation And Description 47

4.2.2 Membrane Description 48
4.2.3 Pilot Equipment Description 50
4.2.4 Experiment Description 52
4.2.5 Data Analysis 53
4.3 Results and Discussion 54
4.4 Recommendations for Future Work 58
4.5 References 59

5 SYNTHESIS AND EVALUATION OF BIOCIDAL COATINGS TO REDUCE BIOFOULING ON WATER-TREATMENT MEMBRANES 61
5.1 Abstract 61
5.2 Introduction 61
5.3 Experimental 63
5.3.1 Materials 63
5.3.2 Characterization And Measurements 64
5.4 Results And Discussion 65
5.4.1 Preparation Of Coatings 65
5.4.2 Interaction Forces With A Negatively Charged Particle Probe 68
5.4.3 Antimicrobial Effects Of Surface Coatings 68
5.4.4 Biofouling Of Coated Reverse Osmosis Membranes 70
5.5 Conclusions 70
5.6 References 71

6 DESIGN OPTIMIZATION OF ANTI-FOULING MICROMIXERS FOR REVERSE OSMOSIS MEMBRANES 75
6.1 Abstract 75
6.2 Introduction 75
6.3 Development of CFD Model 76
6.3.1 Parameter Definitions 76
6.3.2 Boundary Conditions 77
6.3.3 Performance Metrics 78
6.3.4 Grid Development 78
6.3.5 Parameterization 79
6.3.6 3D Model Examples 79
6.4 Results and Discussion 80

6.4.1 Statistical Analysis 80
6.4.2 Flow Analysis 82
6.5 Conclusions 85
6.6 References 86
7 COMPUTATIONAL FLUID DYNAMICS SIMULATIONS OF MEMBRANE PROCESSES 87
7.1 Flow Across Membranes 87
7.2 Particle Tracking 88
7.2.1 Electrostatic Forces 89
7.2.2 Drag Force 89
7.2.3 Repulsive Force 90
7.2.4 Lift force 93
7.2.5 Motion of particles 93
7.3 Model Domain Description 94
7.4 Simulation Results 95
7.5 References 100
8 OPTIMIZATION OF MICROMIXER DESIGN TO MINIMIZE BIOFOULING 103
8.1 Introduction 103
8.2 Optimization of Mixer Design in 2D Flow Channel using GOMA and DAKOTA. 103
8.2.1 Optimization Description 105
8.2.1 Coupling between GOMA and DAKOTA 106
8.2.2 Discussion 107
8.3 Optimization of Mixer Design in 3D Flow Channel using FLUENT and DAKOTA. 108
8.3.1 Membrane Description 108
8.3.2 Optimization Description 110
8.3.3 Discussion 112
8.4 References 112

This page is intentionally left blank

LIST OF TABLES

Table 2-1. Summary of experimental runs and computational simulations. 25

Table 2-2. Relative microbial concentrations (observed) and simulated mass transfer for different membrane configurations. 29

Table 3-1. Parameters defining chevron designs (see Figure 3-1 for further explanation). 34

Table 3-2. Measured rate of flux decline, median bacteria concentration and average pressure for the membranes tested with printed chevrons (see Table 1 for parameters describing the chevron design for the different reference numbers). The two values in each column represent the results for the tests on duplicate membranes.....38

Table 3-3. p-values and R^2 from of Design of Experiments analysis on results of tests using chevron membranes. p-values less than 0.05 show the factor is significant. N/A indicates a p-value greater than the term was removed from the model as it was determined not important due to high p-values in previously run models. 42

Table 4-1. Chemistry of tap water. 48

Table 4-2. Initial Membrane Test – Modified Membrane Characteristics 49

Table 4-3. Comparison of Measured Permeate Flow Rate and Salt Rejection to Reported Membrane Specifications. 56

Table 7-1. Results from particle tracking simulations with no repulsive force. 97

Table 8-1. Mesh refinement study for the 1mm-gap 2D model. 106

Table 8-2. Summary of geometries that have been tested for highest salt rejection. In all of the runs, height = 0.25 mm, width = 0.3 mm, and the lines are out-of-phase. 111

This page is intentionally left blank

LIST OF FIGURES

Figure 2-1. Robocasting printing platforms with a moving part (top left) or moving print head (top right). In-phase (middle left) and out-of-phase (middle right) chevron patterns with 25% membrane coverage. Bottom photo shows membrane printed with micromixers (dyed for display purposes only; membranes used in the testing were not dyed). 23

Figure 2-2. Schematic of cross-flow test apparatus. Arrows show direction of flow. 24

Figure 2-3. MCR results from the 25% coverage, inphase experimental condition. The plot shows the pure spectral components normalized to unit length. 26

Figure 2-4. Experimental and computational results for the following micromixer patterns: (a) blank (no micromixers); (b) 25% coverage, out-of-phase; and (c) 25% coverage, in-phase. The top image in each pair is the relative microbial concentration as observed by hyperspectral imaging; the bottom image in each pair is the simulated relative shear stress on the membrane surface. The contrast on the hyperspectral images above was enhanced to help illustrate the patterns of microbial growth. Micromixer ‘‘peaks’’ and ‘‘valleys,’’ referred to in the text, point to the left and right, respectively. 27

Figure 2-5. Simulated three-dimensional, swirling flow patterns induced by the micromixers. Flow is from left to right. 27

Figure 2-6. Histograms of propidium iodide (PI) concentration (fluorescence intensity) as determined by hyperspectral imaging for the following micromixer patterns: (a) blank (no micromixers); (b) 25% coverage, out-of-phase; and (c) 25% coverage, in-phase 28

Figure 2-7. Comparison of observed microbial concentration ratios (micromixer/blank) for different membrane configurations using Series 1 (top) and Series 2 (bottom) test data. The simulated mass transfer of a scalar applied to the membrane surface is also shown in each plot. Normalized values are taken from the ratios reported in Table 2 (inverse ratios are used for the simulated concentrations). 29

Figure 3-1. Schematic defining factors used to describe the chevron design. This example is the mid-point chevron design with 7 peaks per line, 7 lines per membrane and a chevron θ of 90˚. Out-of-phase membranes are shown on top and in-phase on the bottom. Rectangle on the top image shows hyperspectral image location. 35

Figure 3-2. Schematic of cross-flow testing system. 36

Figure 3-3. Box plots comparing rate of flux decline (A), Median fluorescent intensity due to bacteria on the membrane surface (B) and average pressure (C) for tests in this study. 39

Figure 3-4. SYTO® 59 fluorescence intensity counts (as measure of bacteria concentration) distributions on the surface of 6 membranes with designs of Cases (see Table 1 for reference number) 3(A), 2 (B), 7 (C), 8 (D),. A blank run with a spacer (E) and an untreated blank membrane (F). The median fluorescence counts for these cases are 573, 212, 116, 209, 907, and 2034, respectively. Note that different scales of bacteria intensity are used to emphasize pattern of bacterial accumulation. The contrast has been enhanced in each image, such that the largest value in each color bar represents fluorescence intensities equal to or greater than that value. 41

Figure 4-1. Schematic of Dow Filmtec TW30-1812-75 membrane element showing dimensions. 49

Figure 4-2. Schematic of modified membrane element showing chevrons.....50

Figure 4-3. Photographs of front and back sides of system for testing spiral would elements. 51

Figure 4-4. Results of testing commercial membrane. 55

Figure 4-5. Measured pressure loss (left) and permeate flow (right) for the two membrane elements run with the Case 1 chevron design (see Table 4–2). Note the difference in results for duplicate membranes. 57

Figure 4-6. Measured pressure loss and permeate flow for the two membrane elements run with the Case 2 chevron design (see Table 4-2). Note the difference in results for duplicate membranes. 57

Figure 4-7. Photograph of membrane element during dye test. Note clear signs of dye in the concentrate, but not in the permeate. 58

Figure 4-8. Photograph of feed side (A) and permeate side (B) of membrane after dye test. Note that dye penetration in relation to the chevrons are not observed. 59

Figure 5-1. Synthesis of poly(sulfone) with quaternary ammonium groups. 66

Figure 5-2. Efficiency of bromination in the synthesis of Br-TMPS. Equivalents of NBS are per polymer repeat unit. Degree of functionalization = number of bromomethyl groups per repeat unit. 67

Figure 5-3. SEM image of cross section of an ultrafiltration membrane with PS-QA1 coating. 67

Figure 5-4 . Streaming potential measurements. A is coated with PS-QA1, E is coated with PS-QA8, F is coated with PS-QA10, G is coated with PS-QA12, and H is not coated. 68

Figure 5-5. Contact Angles. A is coated with PS-QA1, E is coated with PS-QA8, F is coated with PS-QA10, G is coated with PS-QA12, and H is not coated. 68

Figure 5-6. Results of AFM force measurements between PS-QA coated membranes and a 3-micron silica colloid probe. (a) Average of normalized interaction force (n>60). (b) Representative retraction force curves. Interaction force of PS-QA12 was always larger than the detection limit (20.8 mN/m) of the cantilever during the measurements. A is coated with PS-QA1, E is coated with PS-QA8, F is coated with PS-QA10, G is coated with PS-QA12, and H is not coated. 69

Figure 5-7. Number of cells attached on coated membranes. A is coated with PS-QA1, E is coated with PS-QA8, F is coated with PS-QA10, G is coated with PS-QA12, and H is not coated. 69

Figure 5-8. Percentages of live and dead cells on coated membranes after 1h incubation with 10^6 *E. coli* cells/mL. Dead cells on the uncoated membrane could not be counted due to adsorption of the dye to the membrane. A is coated with PS-QA1, E is coated with PS-QA8, F is coated with PS-QA10, G is coated with PS-QA12, and H is not coated. 70

Figure 5-9. Concentration image of (a) SYTO® 9 stain and (b) PI stain on RO membrane after 60 hours in crossflow system test. The left half of the membrane was coated with PS-QA1. The right half was uncoated. SYTO® 9 stains both live and dead cells. PI stains only dead cells. 71

Figure 6-1. A membrane channel imprinted with micromixers is defined by seven dimensions. This figure shows one wavelength of the micromixer pattern. 77

Figure 6-2. The boundary conditions applied to a 3D channel model in CFdesign®. 77

Figure 6-3. The mesh of a configuration with 0.5 mm tetrahedral elements. The mesh is enhanced in high-gradient regions. 78

Figure 6-4. Four parameters are varied with low, middle, and high values. The chevron width is set at twice the chevron depth. 79

Figure 6-5. Depth = 1mm, Channel Width = 10mm, Channel Length = 50mm, Chevron Depth = 0.6mm, Chevron Width = 1.2mm, Chevron Angle = 90°, Chevron Spacing = 5mm 80

Figure 6-6. Channel Depth = 1mm, *Channel Width = 5mm*, Channel Length = 50mm, Chevron Depth = 0.6mm, Chevron Width = 1.2mm, Chevron Angle = 90°, Chevron Spacing = 5mm 80

Figure 6-7. Channel Depth = 1mm, Channel Width = 10mm, Channel Length = 50mm, *Chevron Depth = 0.9mm, Chevron Width = 1.8mm*, Chevron Angle = 90°, Chevron Spacing = 5mm 80

Figure 6-8. Channel Depth = 1mm, Channel Width = 10mm, Channel Length = 50mm, Chevron Depth = 0.6mm, Chevron Width = 1.2mm, *Chevron Angle = 45°*, Chevron Spacing = 5mm 80

Figure 6-9. Channel Depth = 1mm, Channel Width = 10mm, Channel Length = 50mm, Chevron Depth = 0.6mm, Chevron Width = 1.2mm, Chevron Angle = 90°, *Chevron Spacing = 1mm* 80

Figure 6-10. Pareto chart of standardized effects of the 4 3-level factors on the outlet scalar...81

Figure 6-11. Pareto chart of standardized effects of the 4 3-level factors on the inlet pressure. 82

Figure 6-12. Velocity vectors indicate that flow downstream of peaks is accelerated toward the membrane in the case of deep chevron protrusions. 82

Figure 6-13. Flow traces for the deep chevron case, colored by the component of the velocity normal to the membrane surface. The flow converges downstream of the 'peaks' and diverges downstream of the 'valleys'....83

Figure 6-14. Pressure distributions downstream of a peak and a valley for the deep chevron case. The high pressure gradient downstream of the peak accelerates the flow toward the membrane surface. 84

Figure 6-15. Flow traces for the shallow chevron case, colored by the component of the velocity normal to the membrane surface. The flow convergence is less pronounced, and the flow is not significantly accelerated toward the membrane surface. 84

Figure 6-16. Pressure distributions downstream of a peak and a valley in the shallow chevron case. The pressure gradient is not steep enough to significantly accelerate the flow toward the membrane surface. 85

Figure 7-1. Comparison of predicted correction to Stokes drag law for Eqs. 7-11 and 7-12…91

Figure 7-2. Predictions of Goren's corrective force for permeable surfaces. 92

Figure 7-3. Generalized modeled geometry for all cases. 94

Figure 7-4. Schematic and dimensions of the flow cell. Membrane chevrons are not shown. 95

Figure 7-5. In-phase (A) and out-of-phase (B) chevron configuration on RO membrane. Chevron height is 5 mm....96

Figure 7-6. Particle tracking results for no chevron case. 98

Figure 7-7. Particle tracking results for in-phase chevron case.. 98

Figure 7-8. Particle tracking results for out-of-phase chevron case. 99

Figure 8-1. Schematic and dimensions of the flow cell. Membrane chevrons are not shown. 104

Figure 8-2. Two dimensional side view of the flow cell with chevrons (seen as lines in 2D). 104

Figure 8-3. Simple schematic of DAKOTA-GOMA coupling. 107

Figure 8-4. Mass fraction (A) and velocity (B) profiles of a 1-mm channel simulation. 108

Figure 8-5. Optimization history as a function of line diameter (A) and area coverage (B). Simulations used a 1-mm channel depth. 109

Figure 8-6. Coupling schematic of DAKOTA-FLUENTcodes. 111

1 INTRODUCTION

Biofouling of water-treatment membranes has a negative economic impact in desalination and water treatment. With biofouling there is a decrease in permeate production and an increase in energy expenditure due to increased cross-flow pressure needed. Biofouling leads to increased cleaning expenditures. Frequent membrane cleanings and biofouling also accelerates the degradation of the membranes increasing membrane replacement costs. Finally, due to the concentration polarization caused by biofouling the water quality of the permeate degrades. Even when wastewater is being pretreated by microfiltration, biofilms grow on the downstream reverse osmosis (RO) membranes (Sadr Ghayeni et al., 1998). Flemming (1997) estimates that approximately 30% of the total operating costs for Water Factory 21, a RO plant in Orange County, CA, used for wastewater reuse, is for controlling biofouling.

Biofouling is the unwanted growth of biofilms on a surface. In the case of water-treatment membranes, if microorganisms exist in the feed water it is likely that they will adhere to the membrane. Once adhesion has occurred, colonies can grow with the associated extracellular polymeric substance (EPS) forming biofilms thus fouling the membranes. The intention of this work is to minimize the chance for this initial cell adhesion.

To date, a universal successful and cost-effective method for controlling biofouling has not been implemented. Methods for controlling biofouling include minimizing microorganisms and potential nutrients in the feedwater, disinfection of the system, and cleaning of the membranes. Pre-treatment methods for controlling biofouling are site-specific and time and cost intensive (Flemming, 1997). Oxidizing biocides can degrade the polyamide RO membranes (da Silva et al., 2006). Cleaning has been found to temporarily improve the flux through the membrane, but biofouling continues to degrade the membrane performance and with subsequent cleanings, the amount of improvement decreases [(Vrouwenvelder et al., 1998)]. Use of biofouling-resistant membranes is a cost-savings alternative to minimize biofouling.

This SAND report summarizes work conducted under a Sandia National Laboratories Laboratory Directed Research and Development (LDRD) project. The overall goal was to use high-performance computing to direct polymer, material, and biological research to create the next generation of water-treatment membranes. Creation of low-cost, efficient water-treatment membranes helps assure the availability of fresh water for human use, a growing need in both the U. S. and the world. Both physical (micromixers – UV-curable epoxy traces printed on the surface of a water-treatment membrane that promote chaotic mixing) and chemical (quaternary ammonium groups) modifications of the membranes for the purpose of increasing resistance to biofouling were evaluated.

This report is divided into eight Sections, including this Introduction. Sections 2 – 4 describe experimental work on use micromixers to minimize biofouling. Sections 2 and 3 describe testing of centimeter-scale flat membrane sheets. Section 4 describes the testing o larger-scale spiral-wound membranes. Section 4.5 describes the research conducted to evaluate biocidal coatings on the surface of existing reverse osmosis membranes. Sections 2, 6 and 7 describe computational fluid dynamics (CFD) modeling to simulate flow patterns and mass transfer on the

surface of a membrane with different patterns of micromixers. Section 2 describes a comparison of the CFD simulations to experimental results. Section 6 describes a design analysis to optimize the shape of micromixers with the objective of reducing biofouling by increasing the amount of turbulent mixing along the membrane surface. Section 7 describes a different CFD model that includes the flow of water and brine through the membrane as well as particle tracking. The biofouling potential is assumed to be related to the ability of particles to contact and stick to the membrane surface. Salt rejection can be calculated with this model. The ultimate goal was to have the CFD model described in Section 7 fully linked to an optimization code for a complete optimization of the chevron configuration to minimize the attachment of the particles to the membrane surface. This optimization model along with its linking to the CFD model is described in Section 8.

2 PRELIMINARY TESTING OF MICROMIXERS USING DRINKING WATER SOURCE OF BACTERIA

Clifford K. Ho, Susan J. Altman, Howland D.T. Jones, Siri S. Khalsa, Lucas K. McGrath, and Paul G. Clem

The following paper was published in the Journal Environmental Progress:

Ho, C. K., S. J. Altman, H. D. T. Jones, S. S. Khalsa, L. K. McGrath, and P. G. Clem (2008), Analysis of micromixers to reduce biofouling on reverse-osmosis membranes, *Environmental Progress*, *27*, 195-203.

AIChE

Analysis of Micromixers to Reduce Biofouling on Reverse-Osmosis Membranes

Clifford K. Ho, Susan J. Altman, Howland D.T. Jones, Siri S. Khalsa, Lucas K. McGrath, and Paul G. Clem

Sandia National Laboratories, Albuquerque, NM 87185; ckho@sandia.gov and sjaltma@sandia.gov (for correspondence)

Published online 5 May 2008 in Wiley InterScience (www.interscience.wiley.com). DOI 10.1002/ep.10274

Features (micromixers) that promote chaotic mixing were fabricated on reverse-osmosis membrane surfaces and evaluated using computational models and laboratory experiments to determine their effectiveness in reducing biofouling. Computational fluid dynamics models of membrane feed channels were developed using different patterns of micromixers on the membrane surface. The shear-stress distribution along the membrane surface was simulated for steady flows along the different micromixer configurations. In addition, the hypothetical mass transfer of a tracer from the membrane surface was used as a metric to compare the amount of scouring and mixing in configurations with and without micromixers. Epoxy micromixers were printed directly onto membrane surfaces, and different patterns were evaluated experimentally. Fluorescence hyperspectral imaging results showed that regions of simulated high shear stress on the membrane corresponded to regions of lower bacterial growth in the experiments, while regions of simulated low shear stress corresponded to regions of higher bacterial growth. In addition, the presence of the micromixers appeared to reduce the overall biofouling concentration in one series of experiments, but the results were inconclusive in another series of experiments. These results indicate that while the enhancement of mixing and shear stress via micromixers may delay or mitigate the onset of localized membrane fouling from biofilms or other contaminants, the impact of micromixers on the overall performance of reverse-osmosis membranes needs further investigation. © 2008 American Institute of Chemical Engineers Environ Prog, 27: 195–203, 2008

Keywords: biofouling, membrane, CFD modeling, micromixer, hyperspectral imaging

INTRODUCTION

Membrane-based separation processes, such as reverse osmosis (RO) and ultra- or nano-filtration, are commonly used in industrial applications such as desalination, waste-water treatment, and power generation. The major problems associated with membrane-based separation processes include fouling and high pressure loss, which decrease the efficiency of the filtration while increasing operation costs. Fouling from mineral deposition and biofilms has been correlated with "dead zones" of low flow and mixing. Novel designs for *in situ* chaotic micromixers that incorporate different patterns of spacers and features within the membrane channel are investigated in this work to maximize mixing within the membrane.

The potential for enhanced mixing of flow through membrane channels has been investigated previously using computational fluid dynamics modeling. Flow patterns and particle deposition around conventional spacer geometries and their effects on permeate flux and pressure drop have been simulated in both steady and unsteady models [1, 2]. In addition, unconventional shapes for spacers in membrane feed channels have been simulated, where the simulated filaments had concave surfaces (hourglass shape) as opposed to convex (cylindrical) surfaces [3, 4]. These studies focused on optimizing the hydraulics (i.e., minimizing the pressure drop) across the membrane feed channel for different spacer designs.

While computational analysis and evaluation of spacer designs has been prevalent in the literature,

fewer studies have integrated computational studies and experiments to investigate biofouling and the impact of spacers (or turbulence promoters) on the onset and distribution of biofouling on membrane surfaces. Neal *et al.* [5] performed experiments that illustrated the deposition pattern of particles in the vicinity of different filament orientations, but observed deposition patterns were not rigorously compared or correlated to computational simulations. Scott *et al.* [6] performed experiments in a cross-flow test cell using flat and corrugated membranes. They found that the corrugated membranes yielded greater permeate flux than the flat membranes due to a combination of increased surface area and increased scouring via enhanced mixing, which Scott *et al.* [6] postulated helped to disrupt the formation of concentration polarization and fouling. A primary difference between the corrugated designs and the micromixer designs used in this study is that the corrugations in Scott *et al.* [6] were unidirectional, as opposed to the multidirectional chevrons investigated in this study. In addition, the available surface area of the membranes is decreased with the presence of the micromixers.

Previous studies in microfluidic applications have shown that the use of chevron-shaped features can produce chaotic mixing in microchannels, even at low Reynolds numbers [7]. In Stroock et al. [7] small ridges in the shape of chevrons were fabricated on the floor of smooth microchannels and were shown to create twisting, three-dimensional flows that enhanced mixing along the microchannel. The current work attempts to exploit the findings of Stroock *et al.* [7] by employing different patterns of chevrons (micromixers) on membrane surfaces to induce chaotic mixing (swirling, three-dimensional flows) in feed channels near the membrane surface.

The purpose of this article is to provide computational and experimental analyses of the effectiveness of micromixers in reducing biofouling on membrane surfaces. Correlations between simulated metrics (shear stress and mass transfer) and observed biofouling trends, as measured by the amount of microorganisms on the membrane surface, are evaluated for different micromixer patterns. An overview of the empirical methods is provided first, including a description of the membranes, micromixer fabrication, testing, and imaging. A description of the computational analyses is then provided, followed by a discussion and comparison of the computational and experimental results.

EXPERIMENTAL APPROACH

Micromixer Fabrication

Micromixers were printed on polyamide brackish water reverse-osmosis membranes (GE Osmonics) using a robotic syringe-dispense method (Robocasting) developed at Sandia for solid freeform fabrication of high density ceramic components [8, 9]. Robocasting utilizes a three-axis translational robot to quantitatively dispense a high-solids loading slurry or viscous liquid in a syringe through a small tip. Two types of Robocasting platforms are shown in Figure 1: stage motion and gantry motion. In these two types of platforms, either the part under construction is moved in the *x-y* plane under a stationary dispensing tip, or the dispensing tip on a gantry is moved in the *x-y* plane over the stationary part. In both cases, the dispensing tip is moved in the *z*-axis over a stationary part. The Sandia Advanced Materials Laboratory (AML) prints with both types of these instruments. The construction of the part is enabled by custom software that allows computer-aided design of the part, calculation of the syringe path, and numerical control of the motion paths and slurry extrusion rate during construction. Depending on the materials and application, there are different requirements for the rheological properties of the slurry; a review of the requirements for printable slurries is discussed in [10]. In this work, the Robocasting platform was used to enable CAD/CAM printing of UV-curable epoxy traces to directly fabricate micromixers with quantifiable height, spacing, area coverage, and intermixer registry on blank membranes to enable evaluation of varying surface-feature effects (height, spacing, phase relationship) on membrane performance.

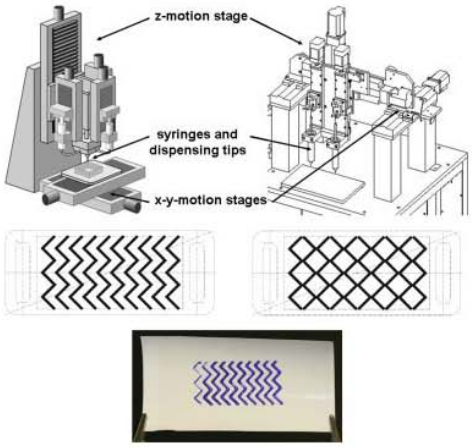

Figure 1. Robocasting printing platforms with a moving part (top left) or moving print head (top right). In-phase (middle left) and out-of-phase (middle right) chevron patterns with 25% membrane coverage. Bottom photo shows membrane printed with micromixers (dyed for display purposes only; membranes used in the testing were not dyed). [Color figure can be viewed in the online issue, which is available at www.interscience.wiley.com.]

The blank membrane (without chevrons) is designed for a typical flux of approximately 44 L/m^2/h at a pressure of 1.55 MPa (225 psi). A UV-curable epoxy (Masterbond UVTK15) was printed directly on the RO membranes, and then UV-cured to develop bioinert micromixer patterns defined by CAD/CAM design and printing. The UV exposure time and intensity (5 min at room temperature using an 8 W, 254

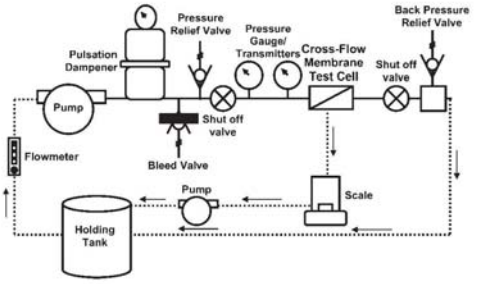

Figure 2. Schematic of cross-flow test apparatus. Arrows show direction of flow.

nm wavelength UV source located 4 cm from the membrane surface) were minimized to avoid membrane oxidation, which can be observed either by visual yellowing of the membrane or a measured decrease in flux. The impact of UV curing on the performance of the membrane was tested by comparing the flux through a membrane that had been UV cured to that of a membrane that had not, and results were similar. FTIR analyses of the membrane were also conducted to examine the chemical changes in the membrane after UV curing and significant changes were not detected.

The printed mixers are qualitatively hemispherical in shape with a 500 μm diameter. The spacing of the rows of chevrons was varied to yield 10 and 25% coverage on the membrane surface, and chevrons were printed both in- and out-of-phase (the phase represents the direction of the chevrons in adjacent rows; if the chevrons in adjacent rows are pointing in the same direction, they are referred to as "in-phase." If the chevrons in adjacent rows are pointing in opposite directions, they are referred to as "out-of-phase"). Representative patterns and a photograph are shown in Figure 1.

Testing

Testing was conducted in a cross-flow apparatus schematically shown in Figure 2. In brief, tap water was transported from the feed tank through a pump to a cross-flow membrane test cell (modified Sterlitech CF042). The dimensions of the flow channel in the cell were approximately 86 mm × 35 mm × 1 mm. Pressure was controlled by a back pressure relief valve downstream of the cross-flow cell. Pressure and flow were monitored upstream of the cell with an Omega PX 303-1K5V pressure transducer and a GF Signet 3-2100-3L turbine flow meter. Temperature was monitored in the feed tank with a submersible T-type thermocouple from Omega. Permeate flowed into a beaker onto a scale to monitor permeate flux. A Campbell data logger (CR1000) was used to collect pressure, temperature, flow, and mass data at 10 min intervals.

Prior to starting a test, the system was cleaned with 0.005% sodium hypochlorite such that the free chlorine level was greater than 2 mg/L. This solution was transported through the system for approximately 1 h. The system was then rinsed three times with deionized (DI) water until the free chlorine was not detected. The membrane was placed in the system and compacted with DI water for at least 6 h at 1.72×10^6 Pa (250 psi). The water was then drained and dechlorinated drinking water derived from groundwater was added to the feed tank. This water had been prefiltered through a PENTEK carbon-impregnated cellulose filter cartridge and a 5-μm Harmsco industrial filter (model 801.5). The system was then run and monitored for approximately 6 days at a pressure of ~250 psi (1.72×10^6 Pa).

At the end of the test, the membrane was removed from the system and stained with 15 μg/mL propidium iodide for 15 min. The higher-than-typical concentration and longer contact time was chosen so that the stain would penetrate both live and dead cells. The membrane was then ready for hyperspectral imaging.

Two series of tests were performed for a total of eight tests (Table 1). Four tests, Series 1, were run between July and September, 2006. In the second series, four tests were run in October and November, 2007. Four different micromixer patterns and a blank membrane with no micromixers were used. The protocol for the two series of experiments were similar with a few exceptions: 20 L of drinking water were used in the Series 1 tests, and only 5 L of drinking water were used in the Series 2 tests; temperature was not controlled in the Series 1 tests, but temperature was controlled at 25°C in the Series 2 tests. In Series 1, a Campbell data logger (CR1000) was used to collect pressure, temperature, flow, and mass data at 10 min intervals. For the Series 2 tests, a National Instruments data acquisition device (CompactDAQ) linked to LabVIEW version 8.2 was used for data collection at 1 min time intervals. Another difference is that the amount of bacteria in the drinking water used for the tests could have changed over time, though the source of the drinking water was the same.

Hyperspectral Imaging

One challenge with imaging fouled membranes is the high degree of autofluorescence emanating from the membrane itself. The autofluorescence is similar in intensity and spectrally overlaps the fluorophore used to selectively stain the biofilm microorganisms. This autofluorescence complicates the use of traditional filter-based fluorescent microscopes for separating membrane-based features from those resulting from the microorganisms itself. We combine the fluorescence hyperspectral imaging with multivariate curve resolution (MCR) algorithms to separate several overlapping fluorophores and create interpretable quantitative images for monitoring the microorganisms on the membrane surfaces. The hyperspectral imager is a line imaging microscope that was origi-

Table 1. Summary of experimental runs and computational simulations.

Micromixer configuration	Series*	End date	Average inlet flow rate (SD) (L/min)	Inlet Reynolds number	Average trans-membrane pressure (SD) (Pa)	Initial permeate flux ($L/m^2/h$)	Test duration (h)
No chevrons	1	August 22, 2006	1.1 (0.03)	546	1.68×10^6 (5.5×10^3)	82	138.7
No chevrons	2	November 15, 2007	1.0 (0.01)	529	1.67×10^6 (2.8×10^3)	86	138.1
10% Out-of-phase	2	October 11, 2007	1.0 (0.02)	522	1.63×10^6 (3.7×10^3)	84	137.7
10% Out-of-phase	2	November 8, 2007	1.0 (0.03)	523	1.67×10^6 (3.7×10^3)	89	139.3
10% In-phase	1	July 12, 2007	1.2 (0.02)	604	1.66×10^6 (1.05×10^4)	76	135.8
10% In-phase	2	November 1, 2007	1.0 (0.03)	513	1.68×10^6 (2.90×10^3)	99	138.5
25% Out-of-phase	1	August 29, 2006	1.1 (0.08)	566	1.67×10^6 (1.7×10^4)	95	138.3
25% In-phase	1	September 5, 2006	1.2 (0.03)	633	1.66×10^6 (7.6×10^3)	93	137.2

*Series 1 tests were performed between July and September, 2006, and Series 2 tests were performed between October and November, 2007 (see Testing section for more details).
SD, standard deviation.

nally developed to improve the scanning of microarrays [11].

MCR, when combined with hyperspectral imaging, is a powerful technique since it has the ability to extract pure-component spectra from the images and provide relative quantitative determinations of each component for each pixel in the image. Thus, MCR can provide quantitative analysis of the image data without the need for standards, and it can discover all the emitting species present in an image, even those about which we have no *a priori* information. A discussion of the MCR analysis algorithms can be found elsewhere in the literature [12–15]. Figure 3 shows the pure spectral components generated using MCR from one of the experimental conditions imaged. This figure shows the degree of spectral overlap between the membrane autofluorescence and the propidium iodide (used to stain the microorganisms) and demonstrates the importance of using hyperspectral imaging and MCR when dealing with highly overlapping fluorophores.

The membrane and biofilm were completely dried and placed onto an elongated microscope slide prior to imaging. The dried membrane was excited using a 532 nm Nd:YVO4 laser and the resultant fluorescence emission was collected onto an electron multiplying CCD detector (Andor Techologies DV465). An infinity-corrected 10× apochromatic objective (NA 0.45) was used for these measurements with the final spatial resolution being 30 μm. Each pixel of the image contained an entire emission spectrum composed of 465 data points from 540 to 900 nm with a spectral resolution of 3 nm. Each image consisted of between 900,000 and 1.2 million spectra. After the collection of the image data, these data were preprocessed to remove cosmic spikes that may have been inadvertently collected on the CCD and to remove image curvature from the spectrometer. MCR was then used to generate the final images.

Hyperspectral images were analyzed in two ways. First, the relative concentration of the propidium iodide on the membrane surface was used for qualitative comparisons to the computational calculations of shear stress on the surface of the membrane. Second, quantitative values of median microorganism concentrations on the membrane were compared to a computationally calculated outlet scalar concentration, as discussed below. The median microorganism concentrations were standardized across the runs to ensure that the concentration variance across experiments was not due to intensity differences resulting from the alignment of the imager. A virgin membrane (no biofouling present) was used as the standard to adjust for intensity differences across different days. Because the size of the membrane samples extracted for imaging was slightly different in each run, the cumulative mass (fluorescence intensity) observed during hyperspectral imaging could not be used. However, the median concentration was found to be a good measure of the representative concentration and a useful metric for comparing membranes. The footprint of the chevrons was not considered in the calculation of the median microbial concentration.

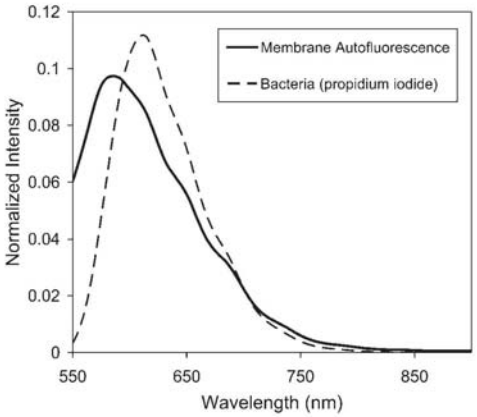

Figure 3. MCR results from the 25% coverage, in-phase experimental condition. The plot shows the pure spectral components normalized to unit length.

COMPUTATIONAL APPROACH

Computational fluid dynamics models were developed to simulate flow patterns and mass transfer in the feed channel with membranes consisting of different patterns of micromixers. SolidWorks® was used to generate the three-dimensional geometry, and CFdesign® was used to mesh the geometry and perform the analysis. The dimensions of the cross-flow test cell used in the experiments were used to create the model domain, and a flow rate of 1.1 L/min (average result of the experiments) was applied as an inlet boundary condition. The flow was laminar ($Re < 1000$) in all cases. Tetrahedral elements were used to conform to the complex shapes of the micromixers, and the mesh was resolved to ensure grid independence. The resulting mesh for each model consisted of over 500,000 elements.

The metrics used in the simulations included the shear-stress distribution on the membrane surfaces and the mass transfer within the feed channel. To simulate mass transfer, a normalized scalar (tracer) was applied to the membrane surfaces (excluding the micromixer surfaces). The average scalar concentration at the outlet of the feed channel was then recorded as a metric to determine the amount of scouring and mixing that was simulated along the membrane surface for each micromixer configuration. The simulated shear-stress distribution and average outlet scalar concentration were compared against the observed microorganisms distribution on the membranes in the experiments to determine if a correlation existed.

Permeation through the membrane was not simulated in these models since the total amount of permeate flux was less than 1% of the total flow in the experiments. Instead, the objective of these simulations was to determine if a correlation existed between the simulated metrics (e.g., shear stress and mass transfer along the membrane surface) and observed biofouling trends (distribution and amount) using the different micromixer patterns. Vrouwenvelder *et al.* [16, 17] suggest that permeation is not an important control of biofouling since they observed similar fouling behavior in their membrane fouling simulator, which does not have any cross-flow, and spiral-wound membrane modules. In addition, Kang *et al.* [18] state that cross-flow velocity does not effect initial deposition for Reynolds numbers below 600.

RESULTS AND DISCUSSION

Flux Measurements

The transmembrane pressure was kept constant for each experiment, and the resulting initial permeate fluxes ranged from ~76 to 99 L/m^2/h, depending on the chevron coverage and resulting flow resistance (Table 1). Trends in the permeate flux over time were difficult to quantify and compare because of these initial differences and other issues. In particular, an initial sharp decrease in permeate flux was noted in many of the tests. We speculate that this initial decrease was due to particulate matter in the drinking water, not biofouling. Measurements of the tap water from the same building yielded the following results: total alkalinity—110 mg/L as $CaCO_3$, SiO_2—40 mg/L, total hardness—130 mg/L as $CaCO_3$, specific conductivity—30-μS/cm. A membrane from an early test was examined under a scanning electron microscope and mineral deposits were not observed. When previous tests were conducted in a synthetic wastewater made with DI water spiked with microorganisms and nutrients (as opposed to tap water used in the current experiments), this initial, rapid flux decline was not observed [19]. Therefore, the permeate flux may have been significantly affected by particulates in the drinking water at early times, and it is not possible to distinguish the influence of biofouling on permeate flux in these experiments. We therefore use the relative microorganism concentration on the surface of the membranes, as measured by the hyperspectral imaging with MCR, as our measure of biofouling.

Examination of the permeate flux data raises questions about the validity of the Series 2 tests. First, there was more variability in the Series 2 flux curves than those of Series 1. Curves from the Series 2 experiments show both the fastest and slowest flux declines. Second, the 10% out-of-phase membrane was evaluated twice for the Series 2 experiments to assess repeatability of the results. The permeate fluxes for the replicate experiments were quite different from each other. In fact, there were greater qualitative differences between both of these tests than the four Series 1 tests.

Correlation between Localized Fouling and Shear Stress

Images generated with hyperpspectral imaging and MCR showed that the micromixers induced spatial variability in the microbial distribution on the membrane surface relative to the blank membrane with

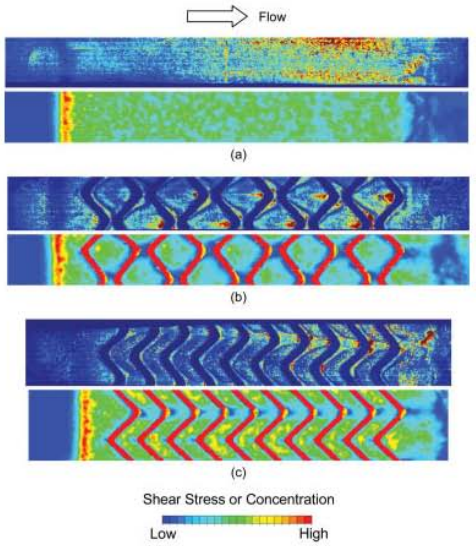

Figure 4. Experimental and computational results for the following micromixer patterns: (a) blank (no micromixers); (b) 25% coverage, out-of-phase; and (c) 25% coverage, in-phase. The top image in each pair is the relative microbial concentration as observed by hyperspectral imaging; the bottom image in each pair is the simulated relative shear stress on the membrane surface. The contrast on the hyperspectral images above was enhanced to help illustrate the patterns of microbial growth. Micromixer "peaks" and "valleys," referred to in the text, point to the left and right, respectively.

no micromixers (see Figure 4). Higher concentrations of microbes were found close to the micromixer, presumably because of stagnant or low flow and mixing. In particular, the microbial concentration was highest just upstream and downstream of chevrons that were pointed downstream ("valleys"). This is more pronounced in the in-phase chevron configuration. In contrast, a distinctive band of low microbial concentration was observed just downstream of the upstream-pointing chevrons ("peaks"). This behavior was observed in both sets of tests that were performed (Series 1 and 2).

We postulate that the bands of relatively low microorganism concentrations are caused by swirling three-dimensional flows induced by the chevrons (see Figure 5). The chaotic flow trajectories shown in Figure 5 just downstream of a "peak" correspond to the band of low microbial concentration seen in the hyperspectral images in Figures 4b and 4c. These swirling flows are believed to increase the local scouring and mixing near the membrane, thereby reducing the fouling in those locations.

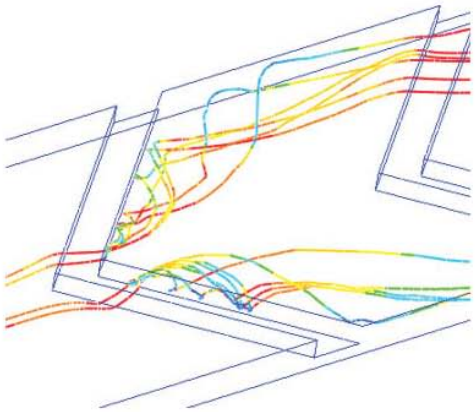

Figure 5. Simulated three-dimensional, swirling flow patterns induced by the micromixers. Flow is from left to right. [Color figure can be viewed in the online issue, which is available at www.interscience.wiley.com.]

Computational simulations of the shear-stress distribution are also shown in Figure 4 for each of the membrane configurations. Regions of higher simulated shear stress are generally correlated to regions of lower observed microbial concentration, and regions of lower simulated shear stress are generally correlated to regions of higher observed microbial concentration. This correlation is consistent with the previous postulation that chaotic, swirling flows increased the localized scouring and mixing on the membrane surface. In Figure 4, the vertical band of high shear stress and low microbial concentration seen toward the left end of each image is caused by the inlet flow, which is normal to the membrane surface, impinging on the membrane.

Performance of Micromixers

The previous section presented results displaying the spatial variation of the microbial concentration on the surface of different membrane configurations, along with correlations to the simulated shear-stress distribution. This section presents a quantitative comparison of the amount of microbial fouling present on each of the membranes to the simulated and mass transfer from the membrane surface.

Figure 6 displays the histograms of the measured microbial concentrations from representative runs. Table 2 and Figure 7 summarize the observed median microbial concentrations for each of the membrane configurations relative to the blank. In the Series 1 tests, the membranes with micromixers yielded lower median microbial concentrations when compared with the blank membrane. The median concentration on the blank membrane (without micromixers) is nearly two–three times greater than the median concentrations on the membranes with micromixers in these tests. Also, it appears that the membranes with

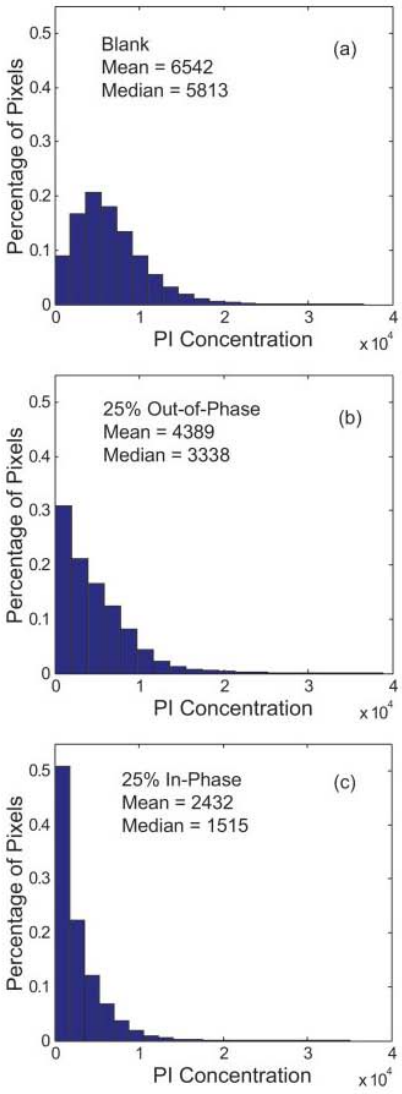

Figure 6. Histograms of propidium iodide (PI) concentration (fluorescence intensity) as determined by hyperspectral imaging for the following micromixer patterns: (a) blank (no micromixers); (b) 25% coverage, out-of-phase; and (c) 25% coverage, in-phase. [Color figure can be viewed in the online issue, which is available at www.interscience.wiley.com.]

greater micromixer coverage (25% vs. 10%) yielded less fouling in the Series 1 tests.

The results of the Series 2 tests show that median concentration on the membranes with micromixers (10% coverage) is greater than the median concentration on the blank membrane. However, as discussed in Flux Measurements section, interpretation of the Series 2 experiments is difficult because of the large variability in the results. In each subsequent experiment in Series 2, the microbial concentration decreased. The largest concentration of microorganisms was observed in the first Series 2 experiment (10% out-of-phase; Table 2), and the observed concentrations systematically decreased over time by more than a factor of four through the last run, which was the blank membrane. This systematic trend was not observed in the Series 1 tests. The exact cause of this apparent time-dependent trend in the Series 2 experiments is uncertain. Differences in the testing protocol are presented in Testing section.

For future experiments, additional controls are being implemented. The biofouling protocol is being modeled after the work of Herzberg and Elimelech [19], where a known concentration of bacteria is added to a system with a known water chemistry. In addition, the amount of bacteria in the feed tank will be monitored throughout the experiment to better understand the quality of the source water. Finally, a design of experiments matrix with replicates will be employed so that systematic trends and variability in results can be assessed.

Table 2 and Figure 7 also display the results of the simulated scalar (tracer) concentration at the outlet of the feed channel for the different micromixer configurations. Ratios (and inverse ratios) of the simulated outlet scalar concentrations relative to the blank are presented. The scalar was applied as a boundary condition to the membrane surface, so the simulated tracer concentration at the outlet provides a measure of the amount of mass transfer (scouring and mixing) along the membrane surface. Larger simulated tracer concentrations at the outlet indicate more scouring and mass transfer along the membrane. Results show that the simulated scalar concentration is generally correlated (inversely) to the observed relative concentration of microbial fouling on the membrane surface in the Series 1 tests. Configurations with larger simulated outlet scalar concentrations correspond to configurations with lower observed microbial fouling. The 25% in-phase chevron configuration yields the highest simulated scalar concentration, and this configuration also corresponds to the least amount of fouling in the Series 1 tests. The 25% in-phase configuration also appears to perform better than the 25% out-of-phase configuration, both computationally and experimentally. However, as mentioned above, more controlled tests with replicates are needed to confirm the impact of different micromixer patterns. These tests are ongoing to investigate the impact of different chevron heights, widths, angles, and spacing.

SUMMARY AND CONCLUSIONS

Laboratory experiments and computational simulations have been performed to investigate the impact of membrane-based micromixers on biofouling. Different patterns of micromixers that have been shown to produce chaotic mixing at low Reynolds numbers

Table 2. Relative microbial concentrations (observed) and simulated mass transfer for different membrane configurations.

Micromixer configuration	Observed membrane microbial concentration ratios (chevron/blank) using median values		Simulated outlet concentration ratios (chevron/blank) for a tracer applied to the membrane*
	Series 1	Series 2	
No chevrons (blank)	1	1	1.00 (1.00)
10% Out-of-phase (October 11, 2007)	N/A	4.65	1.70 (0.59)
10% Out-of-phase (November 8, 2007)	N/A	1.90	1.70 (0.59)
10% In-phase	0.50	4.31	1.73 (0.58)
25% Out-of-phase	0.57	N/A	2.00 (0.50)
25% In-phase	0.26	N/A	2.80 (0.36)

*Inverse ratios are shown in parentheses.

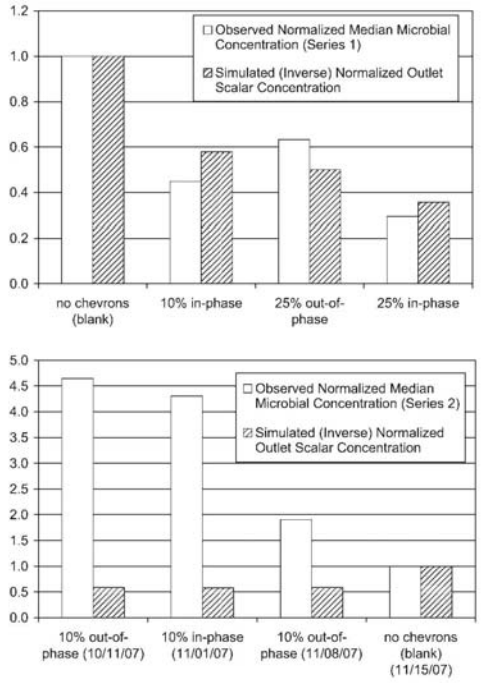

Figure 7. Comparison of observed microbial concentration ratios (micromixer/blank) for different membrane configurations using Series 1 (top) and Series 2 (bottom) test data. The simulated mass transfer of a scalar applied to the membrane surface is also shown in each plot. Normalized values are taken from the ratios reported in Table 2 (inverse ratios are used for the simulated concentrations).

in microfluidic channels have been applied to reverse-osmosis membranes. Computational fluid dynamics simulations of the different micromixer patterns were performed to identify correlations between simulated hydraulic parameters and observed biofouling.

One series of tests provided evidence that micromixers may effectively reduce the amount of biofouling on membrane surfaces. Correlation with simulated shear-stress distributions, flow trajectories, and scalar mass-transfer processes demonstrated that the micromixers may induce swirling, three-dimensional flow patterns that increase the localized scouring and mixing along the membrane surface. Regions of low simulated shear stress were observed to have the largest amount of biofouling, and regions of higher simulated shear stress were observed to have the least amount of biofouling. This locally enhanced mixing may reduce the amount of biofouling on membrane surfaces.

In the second series of tests, the correlation between the biofouling patterns and simulated shear-stress distributions were still observed, but the biofouling concentrations were greater on the membranes with micromixers. Greater variability in the results and potential time-dependent factors made it difficult to evaluate the impact of the micromixers in the second set of tests. A more controlled series of experiments with replicates needs to be run to more definitively assess the impact of the micromixers.

ACKNOWLEDGMENTS

The authors would like to thank Mike Niehaus and Adam Cook for printing the chevrons and Rachel Noek, Jerilyn Timlin, and Michael Sinclair for their assistance with the hyperspectral imaging. They also wish to thank Michael Keenan, Mark Van Benthem, and David Melgaard for their MCR algorithm and software development. Finally, Malynda Aragon is thanked for the water quality data. Sandia is a multiprogram laboratory operated by Sandia Corporation,

a Lockheed Martin Company for the United States Department of Energy's National Nuclear Security Administration under contract DE-AC04-94AL85000.

LITERATURE CITED

1. Schwinge, J., Neal, P.R., Wiley, D.E., Fletcher, D.F., & Fane, A.G. (2004). Spiral wound modules and spacers: Review and analysis, Journal of Membrane Science, 242, 129–153.
2. Li, Y.-L., Chang, T.-H., Wu, C.-Y., Chuang, C.-J., & Tung, K.-L. (2006). CFD analysis of particle deposition in the spacer-filled membrane module, Journal of Water Supply Research and Technology-AQUA, 55, 589–601.
3. Karode, S.K., & Kumar, A. (2001). Flow visualization through spacer filled channels by computational fluid dynamics. I. Pressure drop and shear rate calculations for flat sheet geometry, Journal of Membrane Science, 193, 69–84.
4. Dendukuri, D., Karode, S., & Kumar, A. (2005). Flow visualization through spacer filled channels by computational fluid dynamics. II. Improved feed spacer designs, Journal of Membrane Science, 249, 41–49.
5. Neal, P.R., Li, H., Fane, A.G., & Wiley, D.E. (2003). The effect of filament orientation on critical flux and particle deposition in spacer-filled channels, Journal of Membrane Science, 214, 165–178.
6. Scott, K., Mahmood, A.J., Jachuck, R.J., & Hu, B. (2000). Intensified membrane filtration with corrugated membranes, Journal of Membrane Science, 173, 1–16.
7. Stroock, A.D., Dertinger, S.K.W., Ajdari, A., Mezic, I., Stone, H.A., & Whitesides, G.M. (2002). Chaotic mixers for microchannels, Science, 295, 647–650.
8. Smay, J.E., Cesarano, J., & Lewis, J.A. (2002). Colloidal inks for directed assembly of 3-D periodic structures, Langmuir, 18, 5429–5437.
9. Smay, J.E., Cesarano, J., Tuttle, B.A., & Lewis, J.A. (2004). Directed colloidal assembly of linear and annular lead zirconate titanate arrays, Journal of the American Ceramic Society, 87, 293–295.
10. Stuecker, J.N., Cesarano, J., & Hirschfeld, D.A. (2003). Control of the viscous behavior of highly concentrated mullite suspensions for robocasting, Journal of Materials Processing Technology, 142, 318–325.
11. Sinclair, M.B., Timlin, J.A., Haaland, D.M., & Werner-Washburne, M. (2004). Design, construction, characterization, and application of a hyperspectral microarray scanner, Applied Optics, 43, 2079–2088.
12. Haaland, D.M., Timlin, J.A., Sinclair, M.B., Van Benthem, M.H., Martinez, M.J., Aragon, A.D., & Werner-Washburne, M. (2003). Multivariate curve resolution for hyperspectral image analysis: Applications to microarray technology. In Levenson, R.M., Bearman, G.H., & Mahadevan-Jansen, A. (Eds.), Proceedings of SPIE, Vol. 4959: Spectral imaging: Instrumentation, applications, and analysis II (pp. 55–66), Bellingham, WA: SPIE.
13. Kotula, P.G., Keenan, M.R., & Michael, J.R. (2003). Automated analysis of SEM X-ray spectral images: A powerful new microanalysis tool, Microscopy and Microanalysis 9, 1–17.
14. Van Benthem, M.H., & Keenan, M.R. (2004). Fast algorithm for the solution of large-scale non-negativity-constrained least squares problems, Journal of Chemometrics, 18, 441–450.
15. Timlin, J.A., Haaland, D.M., Sinclair, M.B., Martinez, M.J., & Werner-Washburne, M. (2005). Hyperspectral microarray scanning: Impact on the accuracy and reliability of genomic data, BMC Genomics, 6, 72.
16. Vrouwenvelder, J.S., Bakker, S.M., Wessels, L.P., & van Paassen, J.A.M. (2007). The membrane fouling simulator as a new tool for biofouling control of spiral-wound membranes, Desalination, 204, 170–174.
17. Vrouwenvelder, J.S., van Paassen, J.A.M., Wessels, L.P., van Dama, A.F., & Bakker, S.M. (2006). The membrane fouling simulator: A practical tool for fouling prediction and control, Journal of Membrane Science, 281, 316–324.
18. Kang, S.T., Subramani, A., Hoek, E.M.V., Deshusses, M.A., & Matsumoto, M.R. (2004). Direct observation of biofouling in cross-flow microfiltration: Mechanisms of deposition and release, Journal of Membrane Science, 244, 151–165.
19. Herzberg, M., & Elimelech, M. (2007). Biofouling of reverse osmosis membranes: Role of biofilm-enhanced osmotic pressure, Journal of Membrane Science, 295, 11–20.

3 SYSTEMATIC ANALYSIS OF MICROMIXERS FOR MINIMIZING BIOFOULING ON REVERSE OSMOSIS MEMBRANES

Susan J. Altman, Lucas. K. McGrath, Howland Jones, Andres Sanchez, Rachel Noek, Paul Clem, Adam Cook, and Clifford K. Ho

3.1 ABSTRACT

Micromixers, UV-curable epoxy traces printed on the surface of a reverse osmosis membrane, were tested on a cross-flow system to determine their success at reducing biofouling. Biofouling was quantified by measuring the rate of permeate flux decline and the median bacteria concentration on the surface of the membrane (as determined by fluorescent intensity counts due to nucleic acid stains as measured by hyperspectral imaging). The micromixers do not appear to significantly increase the pressure needed to maintain the same initial permeate flux and salt rejection. Chevrons helped prevent biofouling of the membranes in comparison with blank membranes. The chevron design controlled where the bacteria adhered to the membrane surface. However, blank membranes with spacers had a lower rate of permeate flux decline than the membranes with chevrons despite having greater bacteria concentrations on their surfaces. With better optimization of the micromixer design, the micromixers could be used to control where the bacteria will adhere to the surface and create a more biofouling resistant membrane that will help to drive down the cost of water treatment.

3.2 INTRODUCTION

Biofouling of water-treatment membranes has a negative economic impact in desalination and water treatment. With biofouling there is a decrease in permeate production and an increase in energy expenditure due to increased cross-flow pressure needed. Biofouling leads to increased cleaning expenditures. It also accelerates the degradation of the membranes increasing membrane replacement costs. Finally, due to the concentration polarization caused by biofouling the water quality of the permeate degrades. Even when wastewater is being pre-treated by microfiltration, biofilms grow on the downstream reverse osmosis (RO) membranes (Sadr Ghayeni et al., 1998). Flemming (1997) estimates that approximately 30% of the total operating costs for Water Factory 21, a RO plant in Orange County, CA, used for wastewater reuse, is for controlling biofouling.

Biofouling is the unwanted growth of biofilms on a surface. In the case of water-treatment membranes, if microorganisms exist in the feed water it is likely that they will adhere to the membrane. Once adhesion has occurred, colonies can grow with the associated extracellular polymeric substance (EPS) forming biofilms thus fouling the membranes. The intention of this work is to minimize the chance for this initial cell adhesion.

To date, a universal successful and cost-effect method for controlling biofouling has not been implemented. Methods for controlling biofouling include minimizing microorganisms and potential nutrients from the feedwater, disinfection of the system, and cleaning of the

membranes. Pre-treatment methods for controlling biofouling are site-specific and time and cost intensive (Flemming, 1997). Oxidating biocides can degrade the polyamide RO membranes (da Silva et al., 2006). Cleaning has been found to temporarily improve the flux through the membrane, but biofouling continues to degrade the membrane performance and with subsequent cleanings, the amount of improvement decreases (Vrouwenvelder et al., 1998). Use of biofouling-resistant membranes is a cost-savings alternative to minimize biofouling.

Studies on the use of corrugated membranes and spacers show promise as a method to improve membrane performance. Corrugated membranes are said to enhance flux by promoting turbulence near the membrane wall region. This, in turn, reduces concentration polarization and improves performance (Scott et al., 2000, Vanderwaal et al., 1989, Racz et al., 1986). Scott et al. (2000) illustrate that corrugations can lead to energy savings up to 88% and the savings is dependent on the angle of the corrugations relative to the direction of flow with the largest savings occurring when corrugations were 90^{o} to the direction of flow. Likewise, spacer thickness and configuration can influence localized turbulence, thus decreasing concentration polarization and increasing flux (Lipnizki and Jonsson, 2002, Sablani et al., 2002). Li et al. (2002a, Li et al., 2002b) used computational fluid dynamic modeling to show vortices leading to enhanced mass transfer, presumably due to reduced concentration polarization. They indicate that there is an optimal spacer geometry to maximize mass transfer and minimize power consumption.

Control of critical flux, the flux condition at which particles irreversibly adhere to a membrane, can also assist in minimizing biofouling. Wang et al. (2005) did not observe pressure losses or fouling below the critical flux. Neal et al. (2003) demonstrate that critical flux can, in part, be controlled by spacer orientation.

The goal of our studies is to determine whether micromixers can be used to minimize biofouling on the surface of a membrane. We define micromixers as features on the surface of a water-treatment membrane that promote chaotic mixing. By maximizing localized turbulence and the critical flux, we intend to minimize the amount of initial bacterial adhesion to a membrane. The hope is that bacterial adhesion can be reduced to the extent that biofilms will not form or only minimally form, thus minimizing biofouling. Initial studies showed some promise that micromixers could reduce biofouling (Ho et al., 2008). However, the mixed results in that study suggested that a more systematic study, presented here, is needed.

3.3 MATERIALS AND METHODS

3.3.1 Cultivation, preparation and enumeration of microorganisms

For each experiment, a new stock of Pseudomonas fluorescens (ATCC 700830) was prepared using a CryobankTM bead (Copan Diagnostics Inc) with the P. fluorescens culture. The beads were stored in a -20 °C freezer prior to use. For each test, two vials of inoculum were incubated for 24 hours at 30 °C, each with one bead and 9 ml of Trypticase Soy Broth (TSB). Two of these samples were then vortexed and centrifuged and the pellets combined and reconstituted in 9 ml of sterile DI water. 500 μL of this inoculum was added to 9 mL TSB. This was repeated for 7 vials. The 7 vials were placed on a shaker table set to approximately 50 RPM and incubated at

room temperature overnight. The optical density at 600 nanometers (O.D.600) was determined from one of the vials and recorded. The average O.D.600 value was 0.8 with a range from 0.7 to 1.1. The remaining 6 vials were combined and centrifuged at 10,000 × g. The supernatant was disposed of and replaced with 15 ml of synthetic waste water. This rinsing step was repeated 3 times. The synthetic waste water use by Herzberg and Elimelech (2007) was created by adding chemicals so the final concentrations were 1.16mM sodium citrate, 0.45mM KH2PO4, 0.5mM CaCl2·2H2O, 0.5mM NaHCO3, 2.0mM NaCl, and 0.6mM MgSO4·7H2O. The final pellet was vortexed with 15 ml of synthetic wastewater. One ml of this solution was plated and the rest used to inoculate the cross-flow system. Inoculum counts ranged from 5 × 108 to 2 × 109 CFU/ml.

The amount of P. fluorescens introduced in the feed tank and periodic measurements of P. fluorescens in the tanks were quantified using traditional pour plating methods. Quadruplicate plates with Trypticase™ Soy Agar (TSA) were used to culture the organism. Triphenyl Tetrazolium Chloride (BD Biosciences) was added to the TSA at a final volume of 0.01% to facilitate P. fluorescens enumeration. Plates were incubated at 30 ˚C for approximately 48 hours prior to enumerating. Results are reported as the mean of the counts from the four plates. Samples from the feed tank were collected three times for each test: after cleaning and sterilization of the system, just after inoculation and 20 hours after inoculation just prior to removing the membrane from the test cell. Inoculum concentrations ranged from 4.6 × 106 to 1.8 × 109, with a mean of 1.2 × 109. Concentrations of bacteria in the tank just after inoculation ranged from 1.5 × 106 to 6.0 × 106, with a mean of 3.7 × 106. Concentrations of bacteria in the tank at the end of the experiments ranged from 6.9 × 107 to 1.7 × 108, with a mean of 9.4 × 107.

3.3.2 Micromixer Fabrication

Chevrons were imprinted on commercially available brackish water reverse osmosis (RO) desalination polyamide membranes (GE Sepa™ AG). These membranes are designed for typical flux of 44 L/m^2/hr at 225 psi. Robocasting as described in Ho et al. (2008) using UV-curable epoxy traces was used to directly fabricated the micromixers (Stuecker et al., 2003). For this study, chevron designs were chosen as the micromixer pattern. Robocasting allows for precisely printing and quantifying the height, spacing, chevron angle, wavelength and amplitude and phase-relationship of the chevrons on the membranes surface. A total of 10 chevron configurations were tested in duplicate (Table 3-1 and Figure 3-1). In addition, after analysis of the first 20 tests, the “optimal” membrane design was tested in duplicate (Table 3-1).

3.3.3 Experimental apparatus and setup

Biofouling tests were conducted in two cross-flow systems using a modified Sterlitech CF042 test cell (Figure 3-2). An accelerated biofouling protocol presented in Herzberg and Elimelech (2007) was slightly modified for these tests. The cleaning steps were comprised of first disinfecting the system with 20% household bleach (Clorox) for 1 hour and then rinsed three

Table 3-1. Parameters defining chevron designs (see Figure 3-1 for further explanation).

Ref. #	Peaks	Lines	Height (mm)	θ	Phase	Spacing (mm)	Wavelength (λ) (mm)	Amplitude (mm)	% Coverage
1	4	4	0.25	110	Out	21.4	9.8	3.4	1.4
2	4	4	0.75	110	In	21.4	9.8	3.4	1.4
3	4	10	0.75	70	In	8.6	9.8	7.0	5.1
4	4	10	0.25	70	Out	8.6	9.8	7.0	5.1
5	10	4	0.75	70	Out	21.4	3.9	2.8	2.0
6	10	4	0.25	70	In	21.4	3.9	2.8	2.0
7	10	10	0.75	110	Out	8.6	3.9	1.4	3.6
8	10	10	0.25	110	In	8.6	3.9	1.4	3.6
9	7	7	0.5	90	In	12.2	5.6	2.8	2.9
10	7	7	0.5	90	Out	12.2	5.6	2.8	2.9
Optimal	4	4	0.75	110	Out	21.4	9.8	3.4	1.4

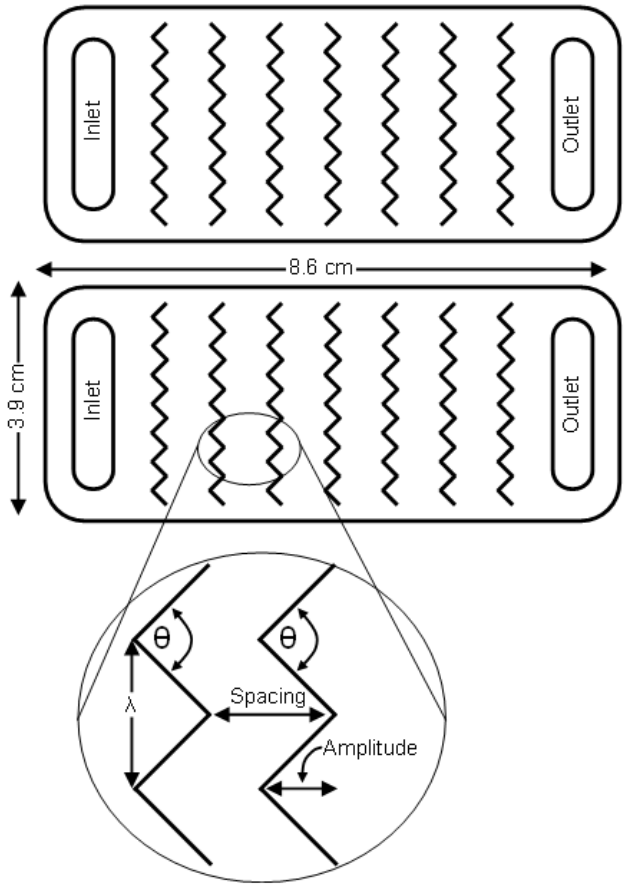

Figure 3-1. Schematic defining factors used to describe the chevron design. This example is the mid-point chevron design with 7 peaks per line, 7 lines per membrane and a chevron θ of 90˚. Out-of-phase membranes are shown on top and in-phase on the bottom. Rectangle on the top image shows hyperspectral image location.

times with deionized (DI) water. Cleaning of trace organic matter was then conducted by circulating 5 mM EDTA through the system for 30 minutes and then rinsing 3 times with DI water. Another step of tracer organic matter cleaning circulated 2 mM of the surfactant sodium dodecyl sulfate (SDS) through the system for 30 minutes and the rinsing 3 times with DI water. Finally, the system was disinfected by circulating 1% NaOCl through the system for 1 hour followed by rinsing the system 4 times with sterile DI water.

After cleaning, the membrane was placed in the test cell and 5 L of sterile DI water added to the feed tank. The system was then started and pressure was set to 300 pounds per square inch (psi). The system was run overnight (packing) at this pressure (minimum of 14 hours). Once flow started, a sample was collected from the feed tank for plating to confirm sterilization of the system (< 10 CFU/ml). After packing, the pressure was adjusted so the permeate flux was close to 40 $L/m^2/hr$ and the synthetic wastewater chemicals were added. The system was then inoculated 5 hours after addition of the wastewater chemicals described above with 14 mL of

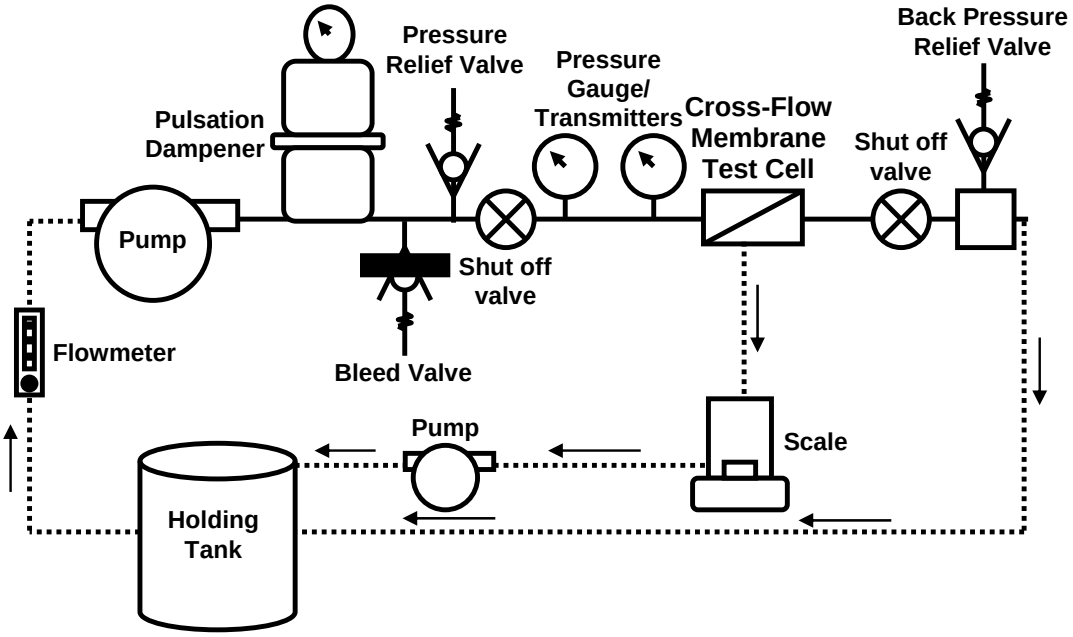

Figure 3-2. Schematic of cross-flow testing system.

inoculum prepared as described above. Thirty minutes after addition of the inoculum, nutrients were added: 5 ml of Luria-Bertani (LB) broth and 20 ml of ammonium chloride. The membrane sample was removed from the system approximately 20 hours after nutrient addition. During operation, the system monitored inlet and outlet pressure, flow rate, water temperature in the holding tank, flow rate, and permeate flux gravimetrically. Flow rates were set at 0.06 gallons per minute (gpm) and ranged from 0.055 to 0.063 gpm. Temperature of the system was set to 25 ˚C. Average temperatures ranged from 24.9 to 26.3 ˚C with temperature variations ranging between 0.3 to 1.4 ˚C within an experiment.

In addition to testing the chevron designs discussed above, a series of "blank" RO membranes were investigated as controls. The blanks included untreated membranes, blank membranes treated with the same UV exposure needed to set the epoxy on the membranes with printed chevrons (UV treated blanks), untreated membranes combined with commercial spacers (blanks with spacers), and finally UV-exposed membranes with commercial spacers (UV-treated blanks with spacers). At least 3 of each "blank" membrane configurations were tested.

3.3.4 Membrane Analysis

Following the cross-flow testing, the membrane was removed and stained with SYTO® 59, a cell-permeant nucleic acid stain. 1 ml of 10 μM SYTO® 59 was pipetted onto the membrane sample and incubated in the dark for 30 minutes. The sample was rinsed 3 times by carefully pipetting 1 ml of 0.1 M sodium bicarbonate over the membrane. The membrane was completely dried and taped onto a flat glass surface using double-sided tape in preparation for imaging.

Membranes were then imaged using a line scanning hyperspectral microscope (Sinclair et al., 2004) and the acquired images were analyzed using multivariate curve resolution (MCR)

(Haaland et al., 2003, Timlin et al., 2005, Kotula et al., 2003, Van Benthem and Keenan, 2004). The dried membrane was excited using a 532 nm Nd:YVO4 laser and the resultant fluorescence emission was collected onto an electron multiplying CCD detector (Andor Techologies DV465). An infinity-corrected 10x apochromatic objective (NA 0.45) was used for these measurements with the final spatial resolution being 30 μm. Each pixel of the image contained an entire emission spectrum composed of 465 data points from 540 to 900 nm with a spectral resolution of 3 nm. Each image consisted of between 650 thousand and 850 thousand spectra. After the collection of the image data, these data were preprocessed to remove cosmic spikes that may have been inadvertently collected on the CCD and to remove image curvature and keystone from the spectrometer. MCR was then used to extract the pure spectral components and their corresponding concentrations (or intensities) from the hyperspectral images.

The use of hyperspectral imaging and multivariate curve resolution allowed for differentiation between the autofluorescence of the membrane and the nucleic acid stain fluorescence (Ho et al., 2008). The quantitative measurement of the SYTO® 59 fluorescence intensity at each pixel within the image is proportional to the microorganism concentration for each pixel within the same image. These SYTO® 59 fluorescence intensities were standardized across the membrane experiments to ensure that the variations in microorganism concentrations across experiments were not due to differences resulting from the alignment and laser fluctuations of the imager. A virgin membrane (no biofouling present) was used as the standard to adjust for these intensity differences across different imaging days. The median fluorescence intensity of SYTO® 59 was calculated using all viable membrane pixels (the footprint of the chevrons was not included in the calculation of this median). This median value was then used to compare the amount of bacteria present across the different membrane configurations. For simplicity, we refer to the results of the imaging as the median measured bacteria concentration, where technically, we mean the median fluorescent intensity across the surface of the membrane due to the SYTO® 59.

3.3.5 Data Analysis

Two metrics were used to quantify biofouling: the rate of permeate flux decline and the median SYTO® 59 fluorescence intensity across the surface of the membrane, which is proportional to the microorganism concentration. Rate of flux decline is defined as the slope of the ln(flux) versus time (in hours) plot. The slope was taken on the line of the initial steep decline in flux.

A Design of Experiments (DOE) analysis was conducted using Minitab® 15 on data to determine which factors have the greatest impact on flux decline and median microorganism concentration and the optimal chevron configuration for minimum microorganisms on the membrane and minimum flux decline. In interpreting DOE analyses, note that the lower the p-value, the more impact the parameter has on the DOE model. If the p-values is greater than 0.05 it is not significant, unless it is involved in an interaction. An interaction is where one factor depends on the level of another factor. The R^2 value indicates the extent to which the DOE model accounts for the variation in the observed data, with a R^2 value of 100% a perfect fit. The optimal chevron design was determined by examining main effects plots to determine the extent to which a change in a factor or term (e.g., number of peaks on a membrane increases or decreases) impacts the membrane performance (e.g., increases or decreases the rate of flux decline). Mid-points in the factorial design were run in the experimental matrix and it was determined that curvature in

the main effects plots did not have to be accounted for to develop the optimal design. The response optimizer in Minitab® was also used to confirm the results.

The non-parametric Mann-Whitney test was used to determine whether the medians of two different data sets are significantly different from each other. The significance level for the Mann-Whitney tests was set to 95%. Minitab® 15 was also used for these statistical analyses.

3.4 RESULTS

Comparisons of the testing results for the different membranes are presented in Figure 3-3. The values of the different parameters used to generate the box plots are included in Table 3-2. The lowest rates of flux decline (the lower the rate of flux decline, the less fouling) were for the membranes without chevrons (blanks) tested with spacers (Figure 3-3A). The membranes with printed chevrons had the next lowest rate of flux decline and the untreated blank membranes had the highest rate of flux decline. There were statistically significant differences between the untreated membranes (blanks) and the chevron printed membranes. The p-value from the Mann-Whitney test was 0.0013 (p-values less than 0.05 demonstrate that the factor is significant). Only two outlier points for the membranes with chevrons were in the same range as the rate of flux decline for the blanks (and at the lower end of the range), indicating less fouling on the chevron printed membranes. There is also a statistically significant difference between the membranes

Table 3-2. Measured rate of flux decline, median bacteria concentration and average pressure for the membranes tested with printed chevrons (see Table 1 for parameters describing the chevron design for the different reference numbers). The two values in each column represent the results for the tests on duplicate membranes.

Ref. #	Rate of Flux Decline	Median Bacteria Concentration	Average Pressure (psi)
1	0.076/0.075	143/146	192/342
2	0.045/0.045	188/212	235/268
3	0.043/0.061	310/573	227/336
4	0.067/0.082	188/285	217/305
5	0.059/0.061	282/643	244/247
6	0.118/0.132	464/717	--- / ---
7	0.065/0.066	116/320	283/ ---
8	0.061/0.063	209/346	232/250
9	0.069/0.060	227/ ---	283/300
10	0.054/0.078	65/380	196/235
Optimal	0.041/0.072	574/184	214/ ---

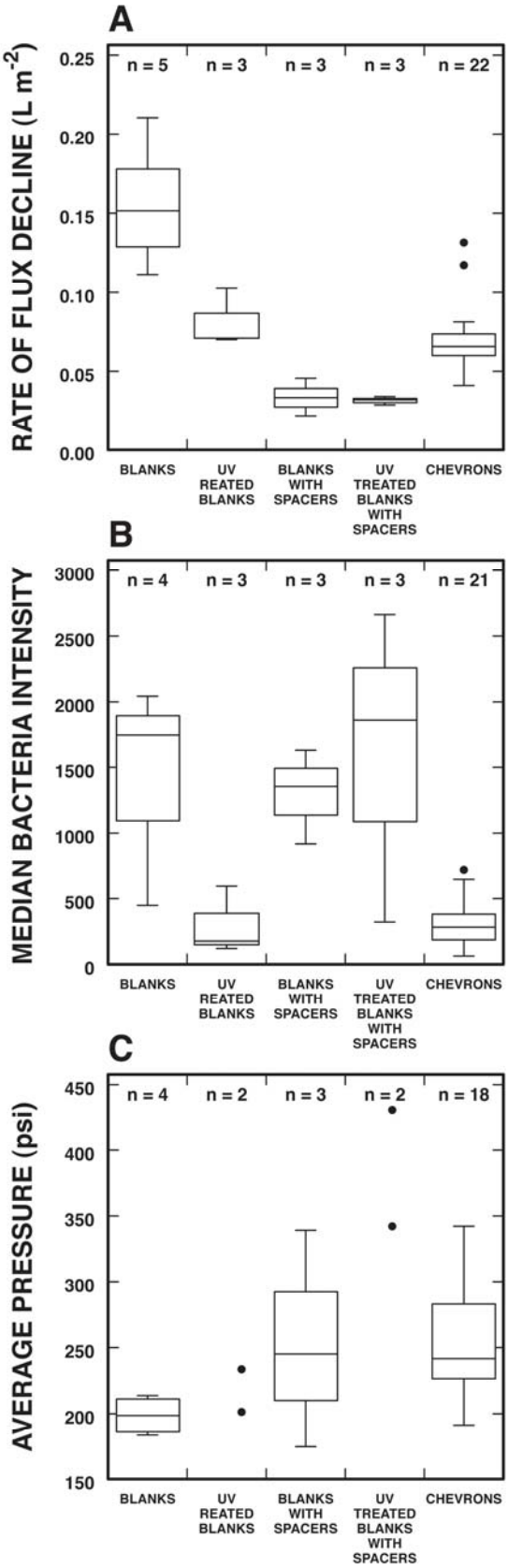

Figure 3-3. Box plots comparing rate of flux decline (A), Median fluorescent intensity due to bacteria on the membrane surface (B) and average pressure (C) for tests in this study.

with chevrons and the blank membranes with a spacer (p-value = 0.0171) (the flux decline is less for the blanks with a spacer). Finally there was a statistically significant difference between the blanks and the blank membranes treated with the same UV exposure needed to set the epoxy on the chevron membranes (p-value = 0.0369), indicating UV exposure alone reduces biofouling.

When examining the membranes run without spacers (blanks, UV blanks, and chevrons), the median fluorescent intensity due to bacteria approximately decreases with decreasing rates of flux decline (compare Figure 3-3A to 3-3B). However, the membranes run with spacers had much higher median bacteria concentrations than would be expected based on the rate of flux decline. The UV treated blanks and the membranes printed with chevrons had the smallest measurement of bacteria on the membranes. Examining the median fluorescent intensity from the bacteria on the blanks, blanks with spacers and UV-treated blanks with spacers show that there can be a large variability in the amount of bacteria measured on a membrane from test to test. The amount of bacteria measured on the blanks with chevrons is significantly less than that measured on the membranes tested that do not have chevrons (p-value = 0.0025).

A trend between the percent area covered by the chevrons and the average pressure needed to maintain the same initial permeate flux of approximately 40 $L/m^2/hr$ was not observed (Figure 3-3C). Nor was there a significant difference between the average pressure used on the blanks and that on the chevron membranes (p-value = 0.3568). A significant difference between the mean salt rejection through the chevron membranes and the blanks membranes was also not observed (p-value = 0.2255) (no shown).

Qualitative observation of the distribution of the bacteria on the membrane surface shows that the chevrons can control the patterns of bacterial accumulation on the membranes surface (Figure 3-4). While the patterns were not always predictable, the trend of less bacterial accumulation in areas of modeled higher shear stress for the in-phase chevron patterns as observed by (Ho et al., 2008) was observed (Figure 3-4A and B). The smaller the chevron angle the narrower the path of higher bacteria concentration (compare Figure 3-4A to Figure 3-4B). The amount of bacteria on each path can also vary as seen in Figure 3-4B. These paths are not as apparent on the out-of-phase chevron patterns, where the prevalent trend observed is trapping of the bacteria in the vicinity of the chevrons (Figure 3-4C). This trapping was observed in half of the membranes with out-of-phase chevrons. There is evidence that higher chevrons trap the bacteria close to the chevrons. The higher bacterial concentration close to the chevrons seen in Figure 3-4C was observed in half of the membranes (both in- and out-of-phase) with a chevron height of 0.75 and none of the membranes with a chevron height of 0.25 mm (compare Figure 3-4C to D). Four of the five membranes with out-of-phase chevrons where trapping was not as apparent had the smallest chevron heights of 0.25 mm. The trapping of the bacteria close to the chevrons did not necessarily lead to overall higher median bacteria concentrations. There were just localized areas of high bacteria. Spacers also clearly impacted the patterns of bacterial adhesion on the membrane surface (Figure 3-4E). In comparison, the bacterial accumulation on the blanks membranes was more random (Figure 3-4F).

Results of the DOE analysis show that the following parameters have the most impact on the rate of flux decline (in order of their impact): chevron height, peaks per line, chevron angle, and line spacing (Table 3-3, remember the lower the p-value, the more impact the parameter has on the DOE model). The numerical sensitivity study of Khalsa and Ho (2008) also showed chevron

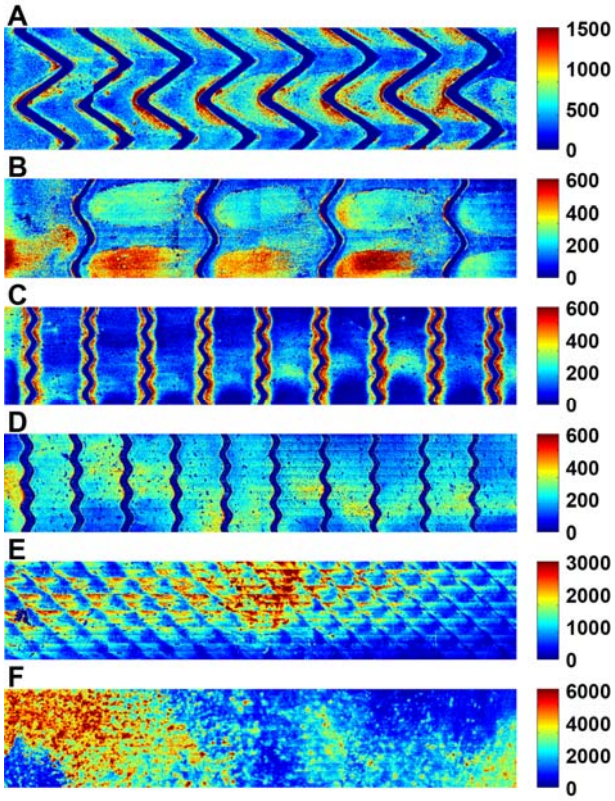

Figure 3-4. SYTO® 59 fluorescence intensity counts (as measure of bacteria concentration) distributions on the surface of 6 membranes with designs of Cases (see Table 1 for reference number) 3(A), 2 (B), 7 (C), 8 (D). A blank run with a spacer (E) and an untreated blank membrane (F). The median fluorescence counts for these cases are 573, 212, 116, 209, 907, and 2034, respectively. Note that different scales of bacteria intensity are used to emphasize pattern of bacterial accumulation. The contrast has been enhanced in each image, such that the largest value in each color bar represents fluorescence intensities equal to or greater than that value.

height, peaks per line, chevron angle, and line spacing as sensitive parameters, although in a different order of impact. The phase of the chevron does not have a significant impact except that it interacts with the number of lines on the membrane. The number of lines on the membrane also interacts with chevron height. The R^2 for the model fitting the flux rate data was relatively high (86.4%). Chevron angle had the largest impact on the median microorganism concentration on the membrane. However, the R^2 for that model was relatively low (45.5%). Both rate of flux decline and median microorganism concentration showed that the optimal design was fewer peaks on a line of chevrons, larger line spacing, and larger chevron angle. The flux decline rate data indicated that larger chevron height was optimal and the median microorganism concentration data indicated that out-of phase chevrons were optimal. Thus, the parameters defining the optimal design as defined by the DOE analysis are shown in Table 3-1.

Table 3-3. p-values and R^2 from of Design of Experiments analysis on results of tests using chevron membranes. p-values less than 0.05 show the factor is significant. N/A indicates a p-value greater than the term was removed from the model as it was determined not important due to high p-values in previously run models.

Factor	Rate of Flux Decline	Median Bacteria Concentration
Height	0.000	N/A
Lines × Height	0.001	N/A
Peaks	0.001	0.088
Theta	0.002	0.005
Lines × Phase	0.002	N/A
Lines	0.010	N/A
Phase	0.614	0.131
R^2	86.36%	45.54%

Two membranes were tested using the optimal design suggested by the DOE analysis of the original 20 membranes tested. The rate of flux decline for these two optimal membranes were in the range of the best performing chevron membranes, but not any smaller (Table 3-2). The concentration of the bacteria measured on the optimal design spanned the range of measured values for the membranes with printed chevrons.

3.5 DISCUSSION

It is clear that membranes with printed chevrons perform better than untreated or blank membranes when they are tested without spacers. This is indicated by both the slower rates in flux decline (and therefore less fouling) and the lower measured median bacteria concentration on the membrane surface. This observation helps to confirm our hypothesis that micromixers can work to decrease bacterial adhesion and thus biofilm growth on the surface of a water-treatment membrane.

However, the flux decline on the blank membranes with spacers had an even lower rate of flux decline, indicating that the spacers could be a sufficient method for increasing localized turbulence. The contradicting information is that the membranes with spacers had higher bacteria concentration in comparison with the membranes with chevrons. Our staining and imaging methods give an incomplete picture of the biofouling as SYTO®59 is not necessarily a good indicator of the amount of EPS on the membrane surface. Therefore, one explanation for our results could be that there is more EPS production on the membranes run without spacers, though it is unclear why this would be. It is also possible that since the spacers were not sterilized they could be introducing bacteria to the system and increasing the bacteria concentration on the membrane surface. However, we find this hypothesis unlikely as the EPS production of these bacteria would have to be small and their impact compared to the bacteria introduced in the accelerated biofouling protocol relatively large. If, in fact, the observed results

of less bacteria on the surface of membranes with chevrons is purely due to the flow patterns, then we would expect that with longer-term tests the membranes with chevrons could out-perform the blank membranes with spacers. That is, with time, the bacteria on the surface of the membranes run with spacers would produce more EPS and foul the membrane more.

The methods used to print the chevrons on the membrane do not appear to impact the performance of the membrane. This includes both the printing of epoxy on the membrane surface and the UV exposure the membrane needed to cure the epoxy. There is no significant difference in salt rejection and pressure needed to maintain the same initial permeate flux between the membranes with chevrons and the other blank membranes. It was anticipated that with the decreased surface area from the chevron coverage, a higher pressure would be needed to maintain the same initial permeate flux, but this correlation was not observed. It should be noted that these tests were conducted on relatively small flat sheets of RO membrane. Printing on larger sheets, and the winding needed to create spiral-would membranes could lead to different results. To truly test the impact of micromixers in controlling biofouling, they must be tested in a spiral wound configuration.

There is some evidence that the UV treatment alone helps the performance of the membrane. This is seen by the significantly lower rates of flux decline for the UV treated blanks in comparison to the untreated blanks (without spacers) and also the lower measured bacteria concentration on these membranes. However, there is a lot of variability in the measured bacteria on the UV-treated membranes with spacers. It is possible that the UV sterilization of the membranes somehow aides in decreasing the biofouling on the membrane surface. However, with the accelerating biofouling protocol used to foul these membranes, the importance of this initial sterilization remains unclear.

The median concentration of bacteria on the membrane surface does not seem to be a good indicator of fouling on the membrane surface. This is seen by both the lower R^2 value in the DOE model, the range of fluorescent intensities measured on different membranes undergoing the same treatment, and the lack of strong correlation between rate of flux decline and median bacterial fluorescent intensity for the membranes run with spacers. An explanation for this observation is that biofouling is more likely controlled by the EPS produced by the bacteria, not necessarily the bacteria themselves.

The optimal chevron design determined by the DOE analysis did not produce a chevron design that led to a slower rate of flux decline than the membranes with chevrons. However, the rate of flux decline measured from the tests of the membranes with the optimal chevron design was on the lower end of the range of the measurements. These results either indicate that: 1) with further refinement, our methods could be used to optimize the chevron designs or 2) that given the variability in our test results, it is not possible to further optimize the chevron designs. Optimization could be conducted with empirical studies such as this or through simulation as initiated by Ho et al. (2008), Khalsa and Ho (2008) and Webb et al. (Section 7).

Our qualitative assessment of the bacterial distribution on the membrane surface indicates that printed micromixer chevrons can better control where the bacteria will adhere to the membrane in comparison with spacers. Perhaps with a more detailed study of different configurations of the micromixers, both with different chevron patterns and other designs beyond chevrons, it will

be possible to produce a membrane that is less likely to foul and perform better than the current standard of using spacers. In addition, while an economic assessment has not been performed, it may be more cost effective to print chevrons directly on the surface of a membrane and eliminate the need for the use of a spacer.

3.6 CONCLUSIONS

The micromixer designs tested in this study show promise as a method to control where bacteria will adhere to a water-treatment membrane, and therefore controlling biofouling. This is seen by both the slower rate of flux decline and the lower bacteria concentration on the membrane surface as compared to an untreated membrane. However, for micromixers to work the design needs to be further optimized in order to outperform the rate of flux decline on untreated membranes with spacers. The membranes with spacers had lower rates of permeate flux decline, but they had higher amounts of bacterial concentration. We postulate that with longer-term tests, the higher amounts of bacteria on the membranes with spacers could eventually produce more EPS and reduce the permeate flux relative to the permeate flux reduction resulting from membranes with micromixers, which yielded lower median bacterial concentrations. With the optimization of the micromixers to minimize biofouling on a water-treatment membrane, an incremental step will be taken to improve water-treatment methods by increasing water quality due to a decrease in concentration polarization, increasing the life time of water-treatment membranes, and reducing the cost of water treatment through decreasing energy usage and operational costs.

3.7 REFERENCES

da Silva, M.K., Tessaro, I.C. and Wada, K. (2006) Investigation of oxidative degradation of polyamide reverse osmosis membranes by monochloramine solutions. Journal Of Membrane Science 282(1-2), 375-382.

Flemming, H.C. (1997) Reverse osmosis membrane biofouling. Experimental Thermal and Fluid Science 14(4), 382-391.

Haaland, D.M., Timlin, J.A., Sinclair, M.B., Van Benthem, M.H., Martinez, M.J., Aragon, A.D. and Werner-Washburne, M. (2003) Spectral Imaging: Instrumentation, Applications, and Analysis. Levenson, R.M., Bearman, G.H. and Mahadevan-Jansen, A. (eds), International Society for Optical Engineering, San Jose, CA.

Herzberg, M. and Elimelech, M. (2007) Biofouling of reverse osmosis membranes: Role of biofilm-enhanced osmotic pressure. Journal Of Membrane Science 295(1-2), 11-20.

Ho, C.K., Altman, S.J., Jones, H.D.T., Khalsa, S.S., McGrath, L.K. and Clem, P.G. (2008) Analysis of micromixers to reduce biofouling on reverse-osmosis membranes. Environmental Progress 27(2), 195-203.

Khalsa, S.S.S. and Ho, C.K. (2008) Design optimization of anti-fouling micromixers for reverse osmosis membranes, Dallas Texas.

Kotula, P.G., Keenan, M.R. and Michael, J.R. (2003) Automated analysis of SEM X-ray spectral images: A powerful new microanalysis tool. Microscopy and Microanalysis 9(1), 1-17.

Li, F., Meindersma, W., de Haan, A.B. and Reith, T. (2002b) Optimization of commercial net spacers in spiral wound membrane modules. Journal Of Membrane Science 208(1-2), 289-302.

Li, F., Meindersma, G.W., de Haan, A.B. and Reith, T. (2002a) Optimization of non-woven spacers by CFD and validation by experiments. Desalination 146(1-3), 209-212.

Lipnizki, J. and Jonsson, G. (2002) Flow dynamics and concentration polarisation in spacer-filled channels. Desalination 146(1-3), 213-217.

Neal, P.R., Li, H., Fane, A.G. and Wiley, D.E. (2003) The effect of filament orientation on critical flux and particle deposition in spacer-filled channels. Journal Of Membrane Science 214(2), 165-178.

Racz, I.G., Wassink, J.G. and Klaassen, R. (1986) Mass-Transfer, Fluid-Flow and Membrane-Properties in Flat and Corrugated Plate Hyperfiltration Modules. Desalination 60(3), 213-222

Sablani, S.S., Goosen, M.F.A., Al-Belushi, R. and Gerardos, V. (2002) Influence of spacer thickness on permeate flux in spiral-wound seawater reverse osmosis systems. Desalination 146(1-3), 225-230.

Sadr Ghayeni, B.S., Beatson, P.J., Schneider, R.P. and Fane, A.G. (1998) Water reclamation from municipal wastewater using combined microfiltration reverse osmosis (ME-RO): Preliminary performance data and microbiological aspects of system operation. Desalination 116(1), 65-80.

Scott, K., Mahmood, A.J., Jachuck, R.J. and Hu, B. (2000) Intensified membrane filtration with corrugated membranes. Journal Of Membrane Science 173(1), 1-16.

Sinclair, M.B., Timlin, J.A., Haaland, D.M. and Werner-Washburne, M. (2004) Design, construction, characterization, and application of a hyperspectral microarray scanner. Applied Optics 43(10), 2079-2088.

Stuecker, J.N., Cesarano, J. and Hirschfeld, D.A. (2003) Control of the viscous behavior of highly concentrated mullite suspensions for robocasting. Journal of Materials Processing Technology 142(2), 318-325.

Timlin, J.A., Haaland, D.M., Sinclair, M.B., Aragon, A.D., Martinez, M.J. and Werner-Washburne, M. (2005) Hyperspectral microarray scanning: impact on the accuracy and reliability of gene expression data. Bmc Genomics 6.

Van Benthem, M.H. and Keenan, M.R. (2004) Fast algorithm for the solution of large-scale non-negativity-constrained least squares problems. Journal Of Chemometrics 18(10), 441-450.

Vanderwaal, M.J., Stevanovic, S. and Racz, I.G. (1989) Mass-Transfer in Corrugated-Plate Membrane Modules .2. Ultrafiltration Experiments. Journal Of Membrane Science 40(2), 261-275.

Vrouwenvelder, H.S., vanPaassen, J.A.M., Folmer, H.C., Hofman, J.A.M.H., Nederlof, M.M. and vanderKooij, D. (1998) Biofouling of membranes for drinking water production. Desalination 118(1-3), 157-166.

Wang, S., Guillen, G. and Hoek, E.M.V. (2005) Direct observation of microbial adhesion to membranes. Environmental Science and Technology 39(17), 6461.

4 SCALE-UP OF MICROMIXERS TO SPIRAL-WOUND ELEMENTS

Malynda Cappelle, Susan J. Altman, and Lucas K. McGrath

4.1 Introduction

A small-scale pilot experiment was performed to test whether the micromixer designs described in Section 3 could be scaled up to a spiral-wound system and to attempt to verify the results from the cross-flow system at a larger, more relevant scale. One of the key objectives of this task was the building of system to test small scale spiral-would membranes in the laboratory. Once built this system could be used to not only test the membranes with micromixers, but also other novel membranes beyond this study.

Reverse osmosis (RO) technology has steadily improved over the years, in terms of efficiency, energy requirements, and overall cost. Water chemistry effects, in terms of the potential for scaling (e.g. calcium carbonate, silica) and inorganic fouling (e.g. iron) is fairly well understood and is usually controlled reliably. Biofouling, however, is not well understood nor well controlled. Part of the problem is the inability to predict water's propensity to biofoul. Most manufacturers will require that the silt density index (SDI) be below 3 for their warranties. However, the SDI test is only indicative of one type of fouling: particulates greater than 0.45 μm. It is equally possible to have an SDI greater than 3 and have no biofouling as it is possible to have an SDI less than 3 and have significant biofouling.

Biofouling of membrane processes leads to increased operational costs by way of higher operating pressures (more energy required), increased chemical costs (cleanings, biocides, etc.), and increased frequency of membrane replacements. Current membrane design includes a feed spacer, which is designed to increase local turbulence inside the feed channel of a membrane and reduce fouling potential. This increases the amount of feed pressure (and pressure drop) when biofouling does occur (Vrouwenvelder et al., 2009).

Current biofouling control practices are primarily physical and chemical processes upstream of the reverse osmosis systems. Physical systems consist of media filters, membrane filtration, and cartridge filters. Chemical processes used consist of flocculation and coagulation-filtration. Each of these can be used effectively to remove the majority of biofoulants, but the potential for biofouling is not eliminated. Proper operational and maintenance programs are critical to quickly detecting and removing biofoulants from reverse osmosis membrane systems.

4.2 Methods

4.2.1 Feedwater Preparation and Description

The source water for the feed to the experiments is the local tap water from Sandia National Laboratories, Albuquerque, New Mexico, Building 823. Water flowed directly from the tap

through a glass column of activated carbon (Calgon Filtrasorb 820) to dechlorinate the water. The water then flowed through another glass column filled with biologically activated carbon that was generated by filling a glass column with activated carbon. The flow direction was from the bottom of the columns to the top of the columns. The column was considered biologically activated when we could get growth when plating the water on Trypticase™ Soy Agar (TSA). The outflow solution was then collected and added to the feed tank of the pilot system, described in Section 4.2.3. Prior to placing water in the experimental feed tank, all water is filtered using 5 μm cartridge filters to remove particulates. Results from a water analyses of tap water collected on January 12, 2009 in a different laboratory in the same building is summarized in Table 4-1.

4.2.2 Membrane Description

Chevrons were imprinted on commercially available, brackish water reverse osmosis (RO) desalination polyamide thin-film composite membrane (Dow Filmtec XLE). Robocasting as described in Ho et al. (2008) and Section 3 using UV-curable epoxy traces was used to directly fabricated the micromixers (Stuecker et al., 2003). Robocasting allows for precise printing and quantifiable control of the height, spacing, chevron angle, wavelength and amplitude and phase-relationship of the chevrons on the membranes surface. Two different micromixer designs were printed on membrane sheets in duplicate (Table 4-2). Case 1 was meant to mimic existing RO membrane spacer geometry for direct comparison to a control. Case 2 is the optimal micromixer design determined by the Design of Experiments analysis described in Section 3.

Table 4-1. Chemistry of tap water.

Analyte	Value
pH	7.4 s.u.
SiO_2	43 mg/L
Fe	0.01 mg/L
Conductivity	1233 μS/cm
Fluoride	0.6 mg/L
Chloride	21.8 mg/L
Nitrate	2.20 mg/L
Sulfate	31.5 mg/L
Calcium	28.5 mg/L
Magnesium	5.3 mg/L
Alkalinity	124 mg/L as $CaCO_3$
Total Hardness	92.8 mg/L as $CaCO_3$

Spiral-wound membrane elements were designed to mimic the Dow Filmtec TW30-1812-75 (Figure 4-1). These elements are designed for home drinking-water systems. They can produce up to 75 gallons per day at a pressure of 50 psi. This design was chosen in order to facilitate micromixer printing, which is currently limited to a width of 12 inches at a time.

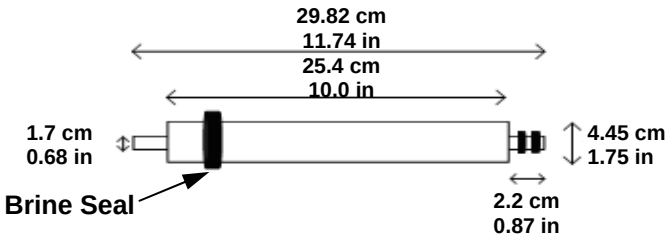

Figure 4-1. Schematic of Dow Filmtec TW30-1812-75 membrane element showing dimensions.

Table 4-2. Initial Membrane Test – Modified Membrane Characteristics (refer to Figure 3-1).

	Case 1	Case 2
spacing (mm)	6.0	18.0
wavelength (mm)	4.3	7.5
number of peaks on a line	213	122
amplitude (mm)	2.14	2.63
number of lines on a membrane	42	14
chevron height	0.6	0.6
chevron width	0.6	0.6
angle at peak of chevron (degrees)	90	110
% Coverage	14%	4.0%
Phase	Out of Phase	Out of Phase

A total of 6 membranes were tested. A commercially available spiral wound element (Osmotik® T112-75) was used as the control. This membrane is designed to run between approximately 30 and 150 psi. The specifications state that at 60 psi and 25 ˚C the expected permeate flow rate is 75 gallons per day (gpd). The specifications indicate typical salt rejection rates of 97 – 98% and a minimum rejection of 95%. Case 1 and Case 2 (Table 4-2) were run in duplicate, accounting for 4 of the 6 elements. The 6^{th} case was a membrane sheet without micromixers but exposed to the same UV exposure needed in the micromixer printing to determine the impact of the UV exposure.

Micromixers were printed on sheets 72 inches (1.83 m) × 12 inches (0.30 m). The micromixers printed on the surface of the membrane replace the feed spacer in a typical spiral wound membrane. This sheet size resulted in elements with diameters ranging from 1.48 in (3.75 cm) to 1.57 in (4.0 cm). Figure 4-2 describes the construction of the unrolled experimental element. The element is made by folding a membrane over the permeate tube such that there are two feed surfaces. The membrane sheet that was exposed to UV light but was not printed with chevrons was rolled as a typical membrane would be with both a feedspacer and a permeate carrier sheet.

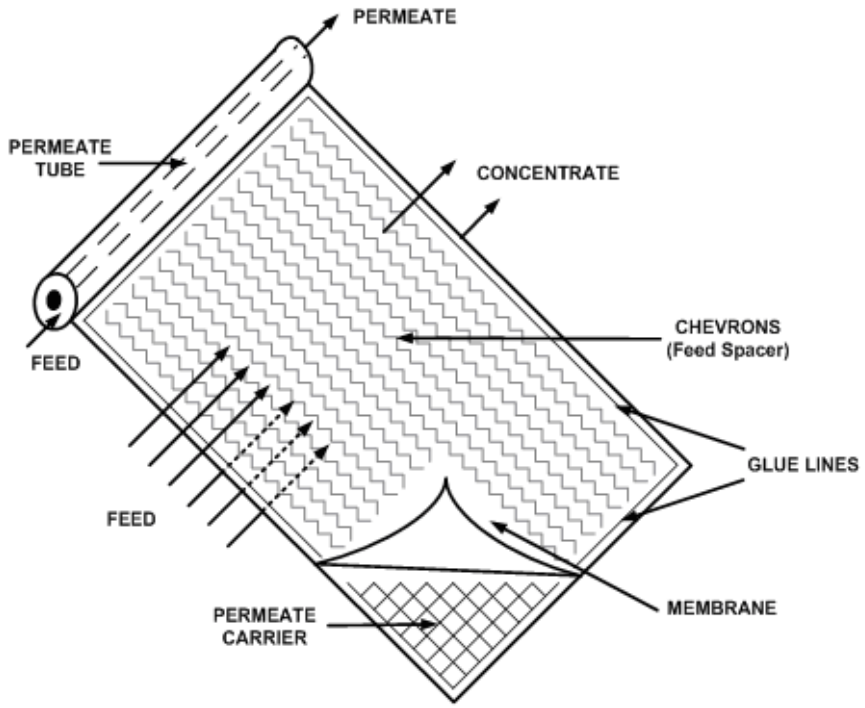

Figure 4-2. Schematic of modified membrane element showing chevrons.

4.2.3 Pilot Equipment Description

The pilot equipment set up allows for simultaneous testing of up to six 2" (nominal diameter) membrane elements (Figure 4-3). The system is currently designed for moderate pressure ratings (less than 100 psi operating pressures). A feed pump feeds water into a distribution manifold with a recycle stream back to the feed tank. Water pressure to the manifold is kept at 75 psi and water pressure is decreased to each individual membrane element using pressure control valves to maintain a pressure of 50 psi. Any water not needed for feed to membrane elements is recycled back to the feed tank. A pressure relief valve is set to 75 psi to prevent over pressurization of the system.

To monitor flux across the membranes, permeate water that has been transported through the membranes dripped into beakers which are placed on balances. Each membrane element's permeate flow (via mass) was monitored with a datalogger. Once the mass reaches a programmed value for the beaker at 75% capacity, a signal will be sent to turn a pump on to drain the beaker, sending water back to the feed tank. The concentrate stream is returned to the feed tank.

A chiller was installed to minimize the heat gain in the feed tank caused by the feed pump and the recycling of all streams of water through the pump back to the feed tank (in other words to control the RO feed water temperature). The chiller is rated to remove 1706 BTU per hour.

Figure 4-3. Photographs of front and back sides of system for testing spiral would elements.

The data logging system used for this project is controlled by LabVIEW, Version 8.6. The pilot system is design to independently monitor and record the following parameters for each membrane element:

- inflow water pressure
- outflow water pressure
- feedwater flow rate
- permeate flow rate
- permeate specific conductivity

In addition, the system monitors and records, room temperature and feed tank water level, specific conductivity and temperature. The datalogger records signals coming from the sensors on a defined interval. The sensors allow for continuous monitoring of the system for data collection and detection of failures of the system. If the pressure, temperature, or flow rate of the system exceeds the programmed thresholds, the pump will power off immediately. Water level monitoring in the supply tank is important to avoid cavitation. In the event that the water level becomes low a signal will be sent to the switch relay that will shut off the pump. Additional protection for the feed pump is provided by a pressure switch directly tied to the power.

4.2.4 Experiment Description

Two tests were run with the pilot system. The first test was a preliminary test with the objective of determining whether the testing system functioned properly and to ensure there were not any large problems with the fabricated membrane elements. Two elements with printed chevrons were run. This test was run for 24 hours between February 16 and 17, 2009.

After the preliminary testing, a dye test was run on the spiral wound membrane elements used in the preliminary test. The objective of this test was to evaluate whether membrane damage had occurred and the weaknesses of the membrane element. A FMI "Q" pump (model: QG150) was used to pump a blue saline liquid across the membrane. A small amount of FD&C Blue Dye #2 ($C_{16}H_{10}N_2O_2$, molecular weight 262.27 g/mol) was added to an inflow solution to obtain a rich blue color. NaCl was also added to the inflow solution to reach a conductivity of approximately 1087 μS. The solution was pumped across the membranes at 50 psi for 30 minutes until the blue dye was visualized in the concentrate. The conductivity of the permeate solution was measured with a handheld device at this time. After running the experiment, the membrane element was taken apart to observe the dye on the membrane surface. This experiment was run on February 23, 2009.

The final experiment commenced on April 15, 2009. The experiment ran smoothly for approximately 7 days. Sometime between April 21, 2009 and April 22, 2009 a scheduled reboot for the networked computer systems shut the experiments down. The system was started again on April 22, 2009 and ran for approximately 9 additional days. Between 15 and 16 days after the original start date, the data was determined to be faulty (feed conductivity less than permeate

conductivity and a sudden increase in feed pressure of more than 20 psi). There appeared to be a grounding issue with the conductivity and pressure date. At that point, it was clear that the membrane elements with printed chevrons on the surface were not performing adequately (see Section 4.3) and it was decided to shut the system down.

4.2.5 Data Analysis

Calculations and data analysis is based on the FTNORM spreadsheet from Dow Filmtec (obtained at http://www.dow.com/liquidseps/design/ftnorm.htm). FTNORM allows for normalization to initial conditions and corrects for temperature variations (reference conditions are 25°C and initial pressure). The temperature correction factor is specific to Dow membranes.

Most reverse osmosis systems would run for 24 – 48 hours, after which the initial or standard conditions for normalization purposes are reached. We chose to set our initial conditions for 48 hours after start of operations. The primary terms that were monitored were recovery ratio (Y), corrected permeate flow (CPF), salt rejection (SR), and the pressure drop.

Corrected permeate flow corrects for the temperature impact on flux through the membrane as well as variations in driving pressure over the duration of the experiment. If initial conditions were warmer than the current conditions, one would expect to see a decrease in flux (flux increases with increasing temperature). A drop in CPF (assuming the system is operating at constant flow rates) is an indicator of membrane fouling. Other factors such as pressure drop and salt rejection will assist in determining the actual cause of CPF decrease. CPF can be calculated as follows:

$$CPF = \frac{NPD_s}{NPD_o} \cdot \frac{TCF_s}{TCF_o} \cdot Q_o \qquad (4\text{-}1)$$

The subscripts "*s*" and "*o*" indicate standard and operating conditions, respectively. We used the initial conditions 48 hours after the start of the test as the standard conditions. Q_o is the permeate flow rate. Normalized permeate flow (NPF) rate is calculated as:

$$NPF = \frac{CPF_o}{CPF_s} \qquad (4\text{-}2).$$

Normalized Pressure Drop, or NDP, is defined as follows:

$$NDP = P_{feed} - \frac{\Delta P}{2} - P_{permeate} - \pi_{feed-concentrate} + \pi_{permeate} \qquad (4\text{-}3)$$

ΔP is the pressure drop calculated as the difference between the feed and concentrate pressure. The π terms are for the estimated osmotic pressure, which were calculated by the Dow Filmtec FTNORM spreadsheet.

The temperature correction factor (TCF) is defined in Equations 4-4 and 4-5:

$$TCF(T > 25^{o}C) = EXP\left[2640 \cdot \left(\frac{1}{298} - \frac{1}{273+T}\right)\right] \quad (4\text{-}4)$$

$$TCF(T < 25^{o}C) = EXP\left[3020 \cdot \left(\frac{1}{298} - \frac{1}{273+T}\right)\right] \quad (4\text{-}5)$$

where T is the feed temperature (˚C). The TCF normalizes permeate water flows to 25°C. The value of 2640 in Equation 4-4 and 3020 in Equation 4-5 are specific Dow Filmtec reverse osmosis membranes. It is possible that the value may be different for the membranes used in this experiment. However, differences are thought to be minimal.

Normalized salt passage (NSP), or its inverse salt rejection (SR), are used to evaluate the quality of water produced by a reverse osmosis or nanofiltration system. Salt passage increases with increasing temperature, so correcting for temperature is necessary to determine whether an observed increase in salt passage (increased permeate conductivity) is due to increased temperature or other conditions. Increased NSP (or decreased SR) can be an indication of membrane damage. NSP is calculated as follows:

$$NSP = \frac{TDS_{permeate}}{TDS_{feed}} \cdot \frac{NDP_o}{NDP_s} \cdot \frac{C_{fc,s}}{C_{fc,o}} \quad (4\text{-}6)$$

SR can be calculated as 1-NSP.

TDS is the total dissolved solids, which was estimated from specific conductivity. The C_{fc} terms are the average feed-concentrate TDS concentrations, which are calculated as follows:

$$C_{fc} = C_{feed} \cdot \frac{\ln\frac{1}{1-Y}}{Y} \quad (4\text{-}7)$$

The “s” and “o” subscripts are the same as in Equation 4-1 and Y is the recovery ratio defined as the ratio of product flow to feed flow.

4.3 Results and Discussion

We succeeded in our main goal of this project, which was to build a pilot-scale apparatus for testing small-scale spiral-wound membranes. This success can be seen in the results attained from running the commercial membrane element. Pressure loss across the membrane ranged from approximately 9 to 11 psi (Figure 4-4A). The initial permeate flow measure through the element (after two days of running the system to allow for stabilization) was approximately 47 gpd (0.033 gpm, 124 mL per minute) (Figure 4-4B). Temperatures varied by approximately 2 – 3 ˚C within a day were continually rising over the entire time of the experiment (Figure 4-4C). It is interesting to see how the measured permeate flow (before the temperature correction) varied with changes in temperature and how applying the temperature correction factor (Equation 4-1) removed these oscillations in permeate flow (Figure 4-4C). Feed specific conductivity

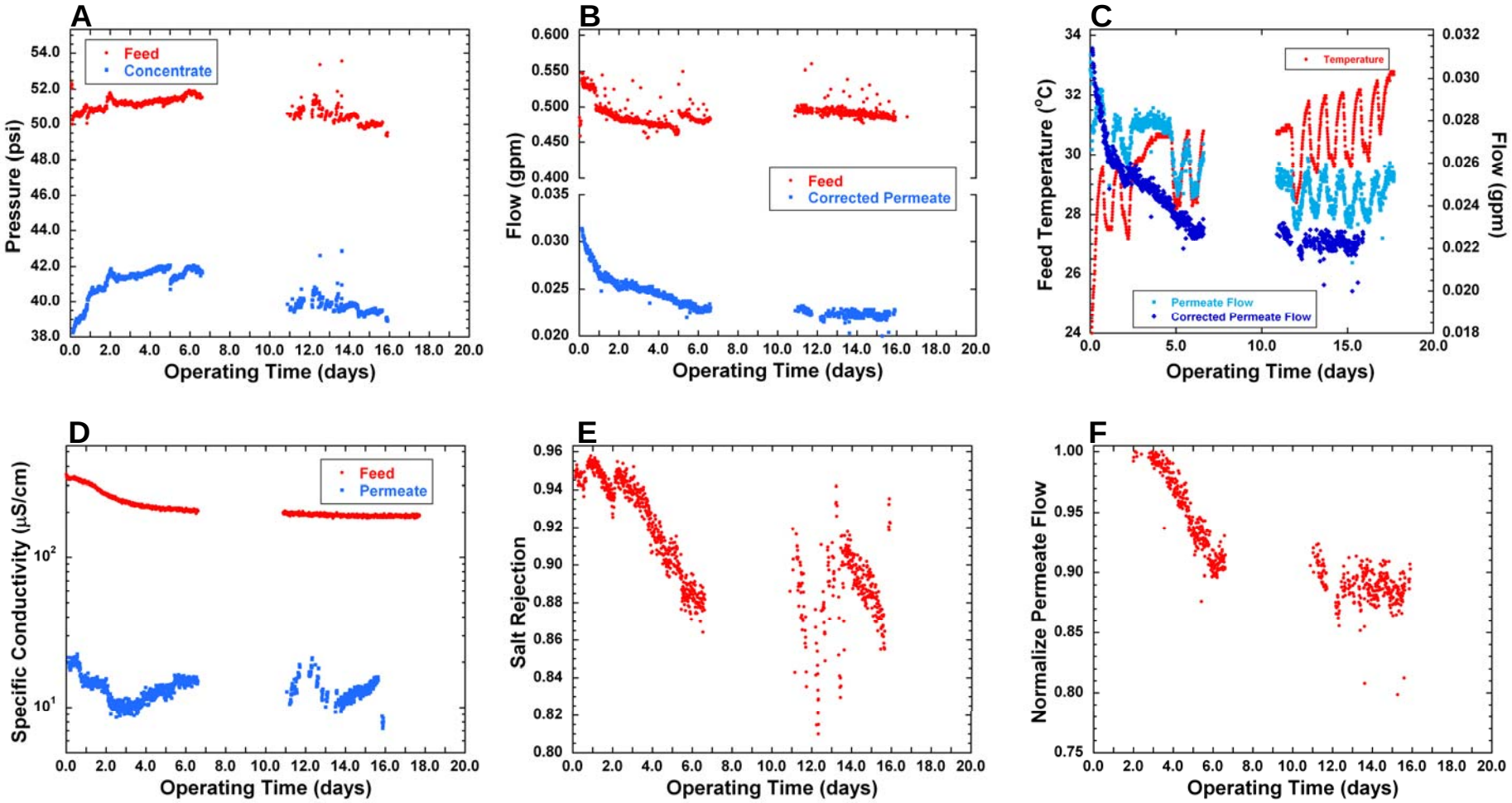

Figure 4-4. Results of testing commercial membrane.

Table 4-3. Comparison of Measured Permeate Flow Rate and Salt Rejection to Reported Membrane Specifications.

Parameter	Specified	Measured
Permeate Flow Rate (gpd)	75 at 60 psi and 25˚C	47 at 51 psi and 30˚C
Salt Rejection	95% - 98%	87% - 96%

decreased over approximately the first 4 days and then stabilized (Figure 4-4D). Permeate specific conductivity ranged between 9 and 17 μS/cm for days 2 – 7. Salt rejection started at approximately 96% and decrease to approximately 87% over approximately the first 7 days of operation (Figure 4-4E). After that time a lot of noise was observed in the salt rejection calculations. Fouling of the membrane was observed with a normalized permeate flux decreasing to approximately 90% after the 7 day period (Figure 4-4F). Note that the permeate flow rates were normalized to the flow after the 2 days it took for the system to stabilize (0.027 gpm). The flux decline appears to be correlated with a decrease in salt rejection (compare Figure 4.4E to 4.4F). Measured performance of the membrane was less than listed in the specifications for the membranes (Table 4-3). It is not surprising that permeate flow is less, as the system was run under lower pressure than listed in the specification. However, even with the pressure differences, the flow is less than expected. The initial salt rejection measured in the membrane is within the specifications of the membranes and may have decrease below specifications due to fouling of the membrane.

Unfortunately, the results of the test on the membrane elements with membranes printed with chevrons were not as favorable. This is true for both the tests run in February and those run in April. Salt rejection values were very low for the 5 non-commercial membrane elements, indicating a failure in the membrane. Note that this failure was observed both for the membranes with printed chevrons and also for the membrane that was exposed to the UV light, but did not have chevrons. In addition, the measured permeate flow rates and pressure losses were not the same for the duplicate membranes (Figure 4-5 and 4-6). It is also interesting to note that the permeate flow rates in the membranes with chevrons are approximately 1 order of magnitude lower than that measure on the commercial membrane. When flow rates are converted to permeate flux (accounting for the cross-sectional area of the membrane, the initial permeate flux (at 2 hours) for the membranes with chevrons range from 1.0 – 2.8 $L/m^2/hr$, in comparison to 12 $L/m^2/hr$ for the commercial membrane. Therefore, decreased cross-sectional area cannot account for the difference in permeate flow rates. There is also a possibility that different base membrane sheets were used, accounting for the differences. Flat sheet tests did not give any indication that the chevron printing impacted permeate flux (see Section 3.4). However, the impact of printing on larger sheets needs to be assessed.

A dye test was run in order to better understand the failure in the membranes. Dye potentially observed in the permeate stream is indicative of membrane damage. The dye was not observed in the permeate flow stream (Figure 4-7). However, the added NaCl was observed in the permeate stream with a conductivity increase from 194 μS/cm in one membrane element and 670 μS/cm in the other to 1087 μS/cm. We conclude that the brine seal did not fail because the dye was not observed in the permeate flow. However, there appears to be some damage within the

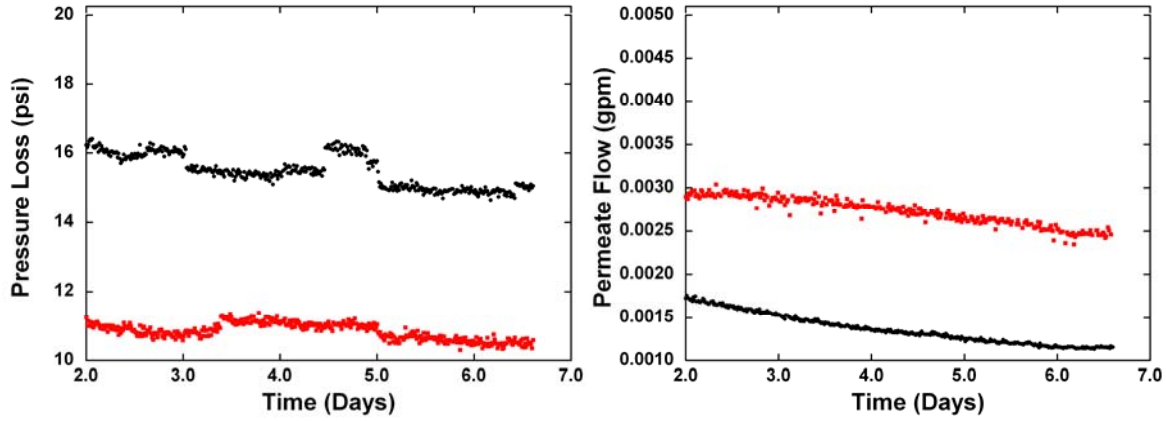

Figure 4-5. Measured pressure loss (left) and permeate flow (right) for the two membrane elements run with the Case 1 chevron design (see Table 4-2). Note the difference in results for duplicate membranes.

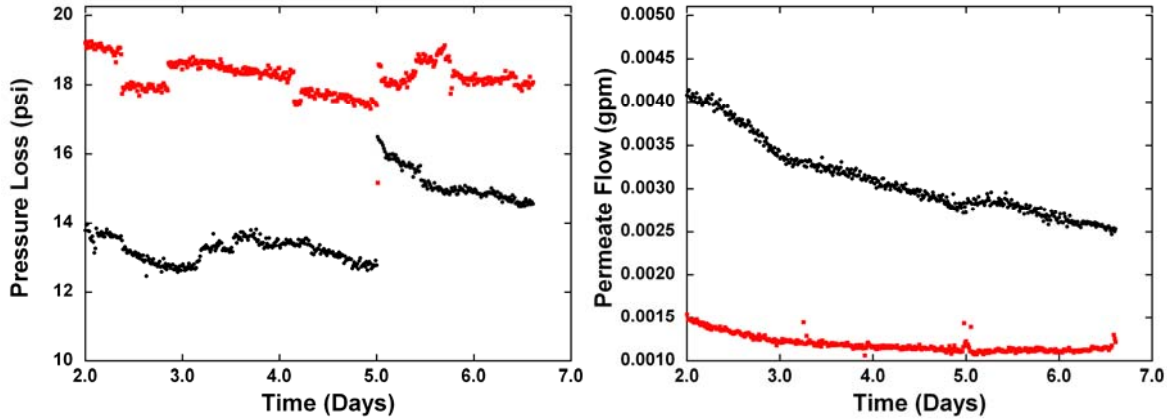

Figure 4-6. Measured pressure loss and permeate flow for the two membrane elements run with the Case 2 chevron design (see Table 4-2). Note the difference in results for duplicate membranes.

membrane, which can allow NaCl molecules through, but not FD&C Blue Dye #2 sized molecules. Salt rejection was also monitored on flat sheets. It was determined that neither the UV exposure nor the chevron printing damaged the membranes (see Section 3.4).

After the dye test was completed, the membrane elements were taken apart and examined to observe where the membrane had been compromised. Specifically, the areas near the chevrons were examined to see if the chevrons themselves may have compromised the membranes. Figure 4-8 presents photographs of the feed (A) and permeate (B) sides of the membrane. The chevrons are the vertical zigzags on membrane surface. Patterns of dye penetration along the chevrons were not observed. However, there are areas where the dye can be seen more prominently on the permeate side of the membrane (see red ovals in Figure 4-8B). These areas appeared to be associated with areas where the membrane has been "scuffed." Further work would be needed to determine why these membranes failed and the flat sheets did not.

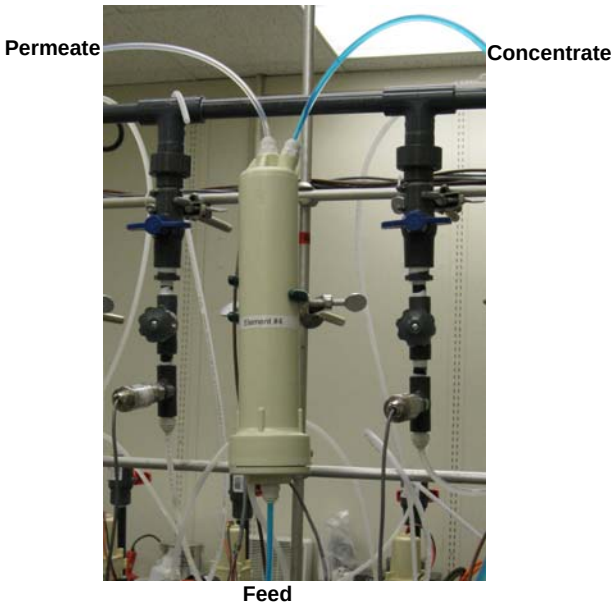

Figure 4-7 - Photograph of membrane element during dye test. Note clear signs of dye in the concentrate, but not in the permeate.

4.4 Recommendations for Future Work

It is first necessary to determine at what step in the imprinting process the membranes are being compromised. Due to time constraints on this study, it was only possible to conduct two rounds of experiments. A more systematic study needs to be performed to determine at what step the membranes fail (UV exposure, chevron printing, wrapping the membranes, etc.). Although dye penetration in association with the chevrons was not observed, we recommend that the epoxy used for chevron printing be re-examined to ensure it is flexible enough to be rolled into the spiral elements without damaging the polyamide surface.

It should be noted that chevron printing was conducted in an ad-hoc manner using equipment designed for printing at a smaller scale. If it was determined that more work will be conducted to evaluate spiral wound membranes with chevrons, larger scale equipment should be designed and built to assist in eliminating unidentified problems that may have been encountered in the current printing process.

In future experiments, we recommend using larger flat membrane sheets on which to print the membranes. Our goal was to have membrane elements with a diameter of approximately 1.7 in (4.3 cm) to mimic the commercial membranes. Our actual membranes were much smaller. Larger sheets would allow for a greater cross-sectional area for permeate flow without any negative impact.

Improvements could be made in the pilot system to better control the increase in temperature over time as the feed water flow through the pump. This could be done by selecting a variable frequency pump. Such a pump would allow the total flow to be adjusted to individual

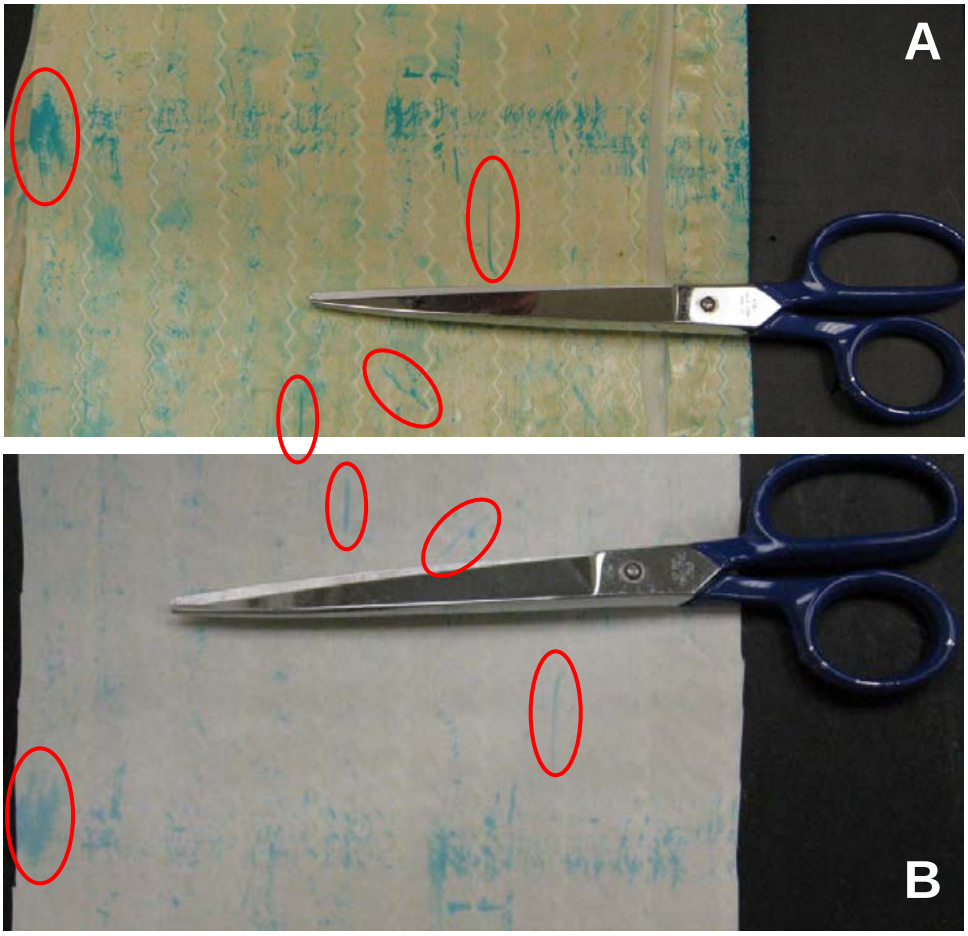

Figure 4-8. Photograph of feed side (A) and permeate side (B) of membrane after dye test. Note that dye penetration in relation to the chevrons are not observed.

experimental needs. This would, in turn, reduce the amount of times the water is recycled, thus decreasing the potential for water being heated by the pump.

4.5 References

Stuecker, J.N., Cesarano, J. and Hirschfeld, D.A. (2003) Control of the viscous behavior of highly concentrated mullite suspensions for robocasting. Journal of Materials Processing Technology 142(2), 318-325.

Vrouwenvelder, J.S., von der Schulenburg, D.A.G., Kruithof, J.C., Johns, M.L. and van Loosdrecht, M.C.M. (2009) Biofouling of spiral-wound nanofiltration and reverse osmosis membranes: A feed spacer problem. Water Research 43(3), 583-594.

This page is intentionally left blank

5 SYNTHESIS AND EVALUATION OF BIOCIDAL COATINGS TO REDUCE BIOFOULING ON WATER-TREATMENT MEMBRANES

Michael R. Hibbs, Susan J. Altman, Lucas K. McGrath, Howland Jones, Andres Sanchez, Christopher J. Cornelius, Seokatae Kang, Atar Adout, Menachem Elimelech

5.1 ABSTRACT

A new concept for the modification of reverse osmosis (RO) membranes by coating the surface with a hydrophilic biocidal polymer is reported. The synthesis of a series of poly(sulfone)s with attached quaternary ammonium (QA) groups is described along with a method for spraying alcoholic solutions of the QA polymers to form water-permeable coatings. The hydrophilicity and surface charges of the coatings were measured by contact angle measurement and streaming potential analysis. Interaction forces between the coatings and a negatively charged particle probe were also investigated. Exposure of the coated membranes to suspensions of E. coli cells and subsequent testing for metabolic activity showed that all of the coatings exhibited significant biotoxictiy. Testing of coated RO membranes in a crossflow RO system showed increased biofilm growth on the coated membranes, presumably due to growth on top of a layer of dead cells that were in contact with the coating.

5.2 INTRODUCTION

Solutions are needed to produce fresh water economically as populations and agricultural demands continue to grow. If future water needs are not addressed with improved desalination and water remediation technologies, it is anticipated that water shortages could escalate globally. Membrane-based separation processes, such as reverse osmosis (RO) are commonly used in industrial applications such as desalination, waste-water treatment, and power generation. RO is generally considered the simplest and most efficient method for desalination [*Rao et al.*, 1997]. Despite the successes of commercially-available RO membranes, they are susceptible to a variety of types of fouling which can reduce the flux of water through the membranes and lead to greater energy input requirements to produce desalinated water. Among these types of fouling, biofouling is considered as the most serious problem since it cannot be prevented using pretreatment [*Baker and Dudley*, 1998].

The polymeric membranes used for RO are typically comprised of a thin active layer supported on a porous substrate. The active layer is most commonly made of a crosslinked polyamide. Many attempts have been made to improve the performance of these membranes by modifying the surface of the active layer to minimize the interfacial energy at the polymer-water interface. Making a surface more hydrophilic has been shown to increase its resistance to the adsorption of foulants [*Krishnan et al.*, 2008]. Hydrophilic membrane surface modification procedures have included the brush-like attachment of both PEG [*Ju et al.*, 2006; *Mickols*, 2001] and poly(acrylate) [*Belfer et al.*, 1998] oligomers, the use of hydrophilic block copolymers as

coatings [*Louie et al*., 2006], and the incorporation of hydrophilic macromolecules directly into the polyamide active layer [*Tarboush et al*., 2008].

An alternative approach to reducing biofouling would be to modify the membrane surface in such a way that it would kill bacteria on contact. Various quaternary ammonium (QA) compounds have long been known to have excellent bacteriacidal properties. This is believed to be the result of two important structural features: (1) the positive charge on the nitrogen atom in the QA group which results in an electrostatic attraction and strong interaction with the negatively charged surface of bacterial cells and (2) a lipophilic hydrocarbon chain (usually 12-18 carbon atoms long) which can disorganize the cell membrane structure and interfere with the membrane function eventually causing the loss of cytoplasmic constituents thus killing the cell [*Ikeda et al*., 1990]. Furthermore, it has been shown that polymers that contain QA groups exhibit higher antibacterial activity against various types of bacteria than their monomeric analogues [*Rembaum et al*., 1970; *Ottenbrite and Myers*, 1973; *Ikeda and Tazuke*, 1983]. These polymers and several other reported QA polymers were all soluble in water however, making them unsuitable for coatings in aqueous environments.

A QA compound with a trimethoxysilyl functionality was developed by Dow Corning (Dow Corning® 5700 Antimicrobial Agent) as a means of imparting antimicrobial activity to treated surfaces. The trimethoxysilyl groups can react with hydroxyl groups on surfaces such as glass and cotton to form covalent bonds that keep the compound from dissolving in water. The trimethoxysilyl groups can also react with each other such that a crosslinked silane network coats the treated surfaces. These coatings have been shown to impart biocidal activity to surfaces in many applications without the release of chemical agents into the surrounding environment [*Isquith et al*., 1972; *Isquith et al*., 1973; *Speier and Malek*, 1982; *Walters et al*., 1973]. Unfortunately, this approach cannot be used to treat RO membranes because they have no hydroxyl surface groups and the hydrophobic silane network would inhibit the passage of water through the membrane. Other methods for activating surfaces for the subsequent attachment of QA species such as oxidative plasma treatment would be too damaging to the thin polyamide layer of an RO membrane and would have a detrimental effect on the performance of the membrane [*Cen et al*., 2003; *Rieser et al*., 1997]. A series of polyurethane coatings with pendant QA groups has been reported to show excellent biocidal activity and durability in water although the passage of water through these coatings is not reported and the required curing conditions could be damaging to a potential RO substrate [*Nurdin et al*., 1993; *Hazziza-Laskar et al*., 1995].

This report describes the preparation of a series of QA-containing polymers which can be applied to a membrane surface by spraying alcoholic solutions of the polymers. The idea is that the coatings will remain on the membrane surface when exposed to water and yet they will be hydrophilic enough that they will not interfere with the passage of water through the membranes. The objective is to determine whether coated RO membranes show a reduction in the rate of biofouling when tested in an RO system.

5.3 EXPERIMENTAL

5.3.1 Materials

4,4'-Isopropylidenebis(2,6-dimethylphenol) (tetramethyl bisphenol A or TMBPA) was recrystallized from toluene and dried under vacuum. 4-Fluorophenyl sulfone was recrystallized from ethanol and dried under vacuum. All other reagents and solvents were purchased from commercial vendors and used without further purification.

Synthesis of Tetramethyl Poly(sulfone) (TMPS)

The parent polysulfone with four methyl groups on each repeat unit (TMPS) was prepared by a variation of the method for preparing a similar poly(sulfone) described by *Harrison et al*. [2003]. TMBPA (8.53 g, 30 mmol), 4-fluorophenyl sulfone (7.63 g, 30 mmol), K_2CO_3 (8.29 g, 60 mmol), anhydrous *N*-methylpyrrolidinone (NMP, 98 mL), and toluene (49 mL) were charged to a 3-necked flask equipped with a mechanical stirrer and a nitrogen flow passing into the flask and out through a distillation head. The reaction was heated at 150 ^{o}C for 4 h while toluene and water were removed as an azeotrope by distillation. The temperature was raised to 160 ^{o}C and held there for 19 h. After cooling to room temperature, the reaction was poured into 0.1M HCl (0.5L) and mixed in a Waring blender. The precipitate was Soxhlet extracted with water for 24 hours and then dried under vacuum to yield a tan solid (14.66 g, 98%).

Synthesis of brominated TMPS (Br-TMPS)

TMPS (32.0 g) was dissolved in 1,1,2,2-tetrachloroethane (470 mL) in a flask equipped with a magnetic stir bar and a condenser. The solution was heated to 85 ^{o}C and *N*-bromosuccinimide (20.0 g, 112 mmol) and benzoyl peroxide (1.36 g, 5.62 mmol) were added. After 3 h, the reaction was cooled and poured into excess ethanol. The precipitate was mixed with ethanol in a Waring blender. The solid was then collected by filtration and triturated with water and then ethanol before being dried under vacuum at room temperature to yield a tan solid (37.01 g, 91%).

Synthesis of Poly(sulfone) with Benzytrimethyl Ammonium Groups (PS-QA1)

Br-TMPS (1.70 g) was dissolved in 42 mL dimethylacetamide. A 45 wt. % aqueous solution of trimethylamine (1.0 mL, 6.5 mmol) was added and the solution was stirred at room temperature for 48 h. The solution was poured into 1M HCl (200 mL), mixed, and filtered. The precipitate was mixed with water in a Waring blender and then triturated with more water before drying under vacuum at room temperature to yield a white solid (1.61 g, 92%).

The dry polymer was mixed with a solution of lauric acid in methanol (1 wt. %) to form a solution with a polymer concentration of 2 wt. %.

Synthesis of Poly(sulfone) with Benzydimethyl-n-octyl Ammonium Groups (PS-QA8)

This synthesis was the same as described for PS-QA1 except that dimethyl-n-octylamine was used instead of trimethylamine. The dry polymer was mixed with a solution of lauric acid (1 wt. %) in methanol to form a solution with a polymer concentration of 3 wt. %.

Synthesis of Poly(sulfone) with Benzydimethyl-n-decyl Ammonium Groups (PS-QA10)

This synthesis was the same as described for PS-QA1 except that dimethyl-n-decylamine was used instead of trimethylamine. The dry polymer was mixed with a solution of lauric acid (1 wt. %) in a mixture of methanol and ethanol (1:1 v/v) to form a solution with a polymer concentration of 2.5 wt. %.

Synthesis of Poly(sulfone) with Benzydimethyl-n-dodecyl Ammonium Groups (PS-QA12)

This synthesis was the same as described for PS-QA1 except that dimethyl-n-dodecylamine was used instead of trimethylamine. The dry polymer was mixed with a solution of lauric acid (1 wt. %) in ethanol to form a solution with a polymer concentration of 1.7 wt. %.

Application of coatings

An airbrush was used to spray known masses of the polymer solutions onto substrates in order to achieve coverages from 3 to 10 mg/in^2. The substrates were either poly(sulfone) EW ultrafiltration membranes manufactured by GE Osmonics or commercially available brackish water reverse osmosis (RO) desalination polyamide membranes (GE Sepa™ AG).

5.3.2 Characterization and Measurements

Gel permeation chromatography (GPC) was performed with a liquid chromatograph equipped with a Viscotek VE2001 isocratic pump and autosampler and a Viscotek VE3580 refractive index detector. The mobile phase was tetrahydrofuran and the system was operated at 25 °C with a flow rate of 1.0 mL min^{-1}. The weight-average molecular weights were measured by calibration with polystyrene standards.

^{1}H NMR spectra of the polymers were obtained on a Bruker spectrometer using 5 mm o.d. tubes. Sample concentrations were about 5 % (w/v) in $CDCl_3$ containing 1 % TMS as an internal reference.

The contact angle measurements were performed using a VCA-2500 system (AST Products, Bellerica, MA) after a drop (~2.5 μL) of DI water was placed on each membrane surfaces. Each measurement provided left and right contact angles, and the average of the 10 measurements (20 values) was calculated. Zeta potentials of the prepared membranes were determined from streaming potential measurements using an asymmetric clamping cell (EKA, Brookhaven Instruments, Holtsville, NY) [*Walker et al*., 2002].

Interaction forces with a negatively charged particle probe were measured by atomic force microscopy (AFM) (Digital Instruments, Santa Barbara, CA) as described on our previous study (Kang et al., JMS, 2007). A silica particle (Interfacial Dynamics Corp., Portland, OR), 3 μm in diameter, was glued to the end of a commercial 0.06 N/m SiN tipless cantilever (Veeco Metrology Group, Santa Barbara, CA). Force measurements were performed in 1 mM NaCl solution at a tip speed of 1 μm/s. The force was normalized to the radius of the particle, R. For a given system, F/R should be a good indicator of the membrane fouling potential [*Lee and Elimelech*, 2006].

Bacterial cell attachment assay followed the modified method suggested by *Campbell et al*. [1999]. Briefly, two pieces (1cm × 1 cm) of each membrane were placed in 100 mL of M63

media supplemented with 20 mg-glucose/L, and incubated for 1 hr at 37°C with *E. coli* cells ($1x10^6$ cells/mL) which were harvested in the exponential growth phase. After the incubation, membrane coupons were gently washed with M63 media to remove loosely bound cells, then stained with propidium iodide (PI) for 15 minutes followed by SYTO®-9 for 5 minutes to examine the viability of *E. coli* cells attached on each membrane surface. Metabolic activity of bound cells were further analyzed using 5-Cyano-2,3-ditolyl tetrazolium chloride (CTC). After incubation with cell suspension, the membrane coupons were washed and incubated again in M63 media supplemented with 0.2 % (w/v) glucose and 4 mM CTC for 1 h at 37°C. Experimental procedures for viability and metabolic activity tests were explained in detail in our previous publication [*Kang et al*., 2008].

Two tests were run to compare coated membranes to uncoated membranes using a cross-flow membrane testing system. Testing methods are described in detail in Section 3.3. In summary, an accelerated biofouling method using *Pseudomonas fluorescens* monitoring the reduction in permeate flux over a 24 hour time period. A third test was conducted using similar methods as described in Section 3.3.3. However, instead of using the accelerated biofouling protocol, dechorlinated tap water was used as described in Section 0. In these tests nutrients were not added to the system. These tests were run for approximately 60 hours after packing. After the test the membrane was imaged using a line scanning hyperspectral microscope (Sinclair et al., 2004) and the acquired images were analyzed using multivariate curve resolution (MCR) (Haaland et al., 2003, Timlin et al., 2005, Kotula et al., 2003, Van Benthem and Keenan, 2004) as described in Section 3.3.4.

5.4 RESULTS AND DISCUSSION

5.4.1 Preparation of coatings

The synthetic scheme for the preparation of the polymers is shown in Figure 5-1. The parent poly(sulfone), TMPS, was prepared by the condensation of 4-fluorophenyl sulfone with TMBPA. In order to drive the reaction to high molecular weights, the product water was removed by azeotropic distillation with toluene. The weight average moleculare weight for the batch of TMPS used to make the coatings in this study was 132,000 with a polydispersity of 2.1.

The benzylic methyl groups on TMPS could be brominated using *N*-bromosuccinimide (NBS) as a source of bromine and benzoyl peroxide as an initiator. The fraction of methyl groups converted to bromomethyl groups was controlled by adjusting the amount of NBS used. Figure 5-2 shows the relationship between the amount of NBS used and the number of bromomethyl groups formed for several different batches of Br-TMPS. In all cases, the reaction temperature was 85 °C, the reaction time was 3 hours, and 0.05 equivalents of benzoyl peroxide (based on NBS) were used. The degree of functionality (DF) is defined as the number of bromomethyl groups per polymer repeat unit and thus has a maximum possible value of 4. In all cases, the DF achieved was approximately 60 % of the DF that would have resulted if every NBS molecule had reacted to make a bromomethyl group.

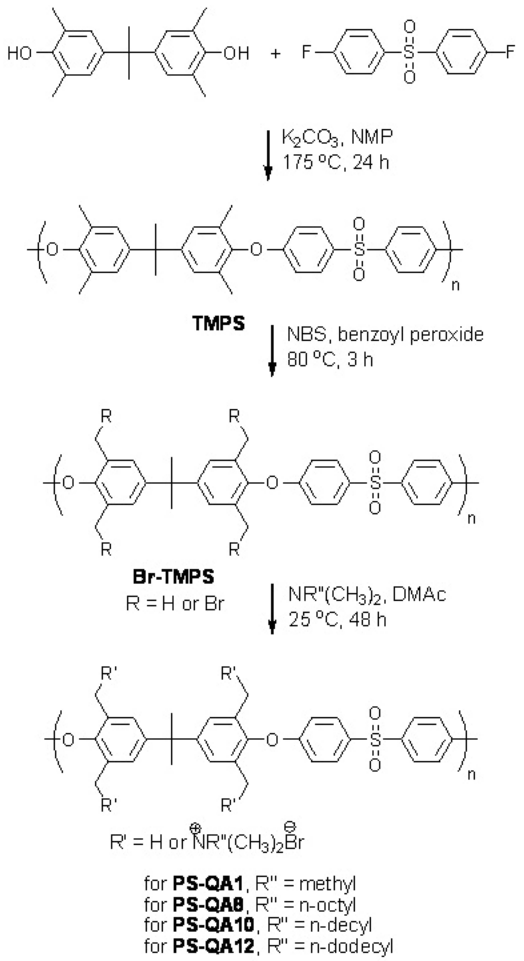

Figure 5-1. Synthesis of poly(sulfone) with quaternary ammonium groups.

All of the PS-QA polymers prepared for this study were made from a batch of Br-TMPS with a DF of 1.44. This value was chosen in order to allow for the maximum density of QA groups without rendering any of the polymers soluble in water. The substitution reaction to form the quaternary ammonium groups took place at room temperature by mixing the desired tertiary amine with a DMAc solution of Br-TMPS. In all cases the neat amine was used, except for trimethylamine which was an aqueous solution. When the QA groups were initially formed, the counter ions were bromide ions. Later during the work-up, the polymers were precipitated in 1 M HCl at which time the bromide ions were exchanged for chloride ions. In the chloride form, the PS-QA polymers were not very soluble in alcohols, so an excess of sodium laurate was added to help them dissolve. Exchange of the chloride ions for laurate ions caused the long, flexible chains of the laurate ions to become closely associated with the polymer chains. Although there was no covalent attachment of the laurate ions to the polymers, their presence enabled the PS-QA polymers to be dissolved in methanol, ethanol, or a mixture of both. Membrane surface characterization

Surface characterization was performed on samples of the PS-QA polymers coated on pieces of a poly(sulfone) ultrafiltration membrane with a coverage of 10 mg/in^2. Figure 5-3 shows an SEM

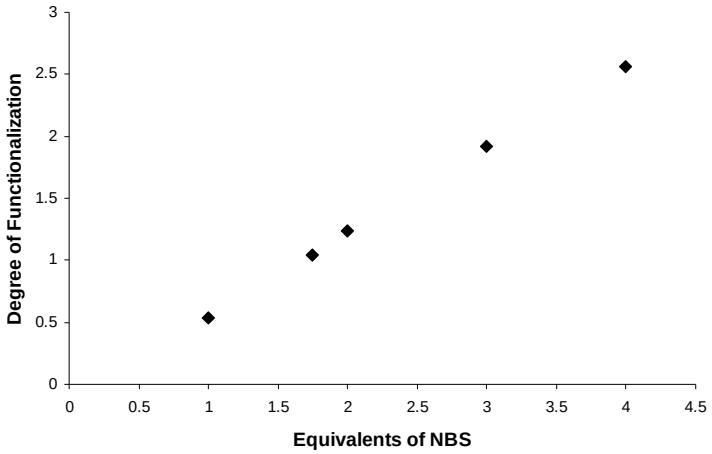

Figure 5-2. Efficiency of bromination in the synthesis of Br-TMPS. Equivalents of NBS are per polymer repeat unit. Degree of functionalization = number of bromomethyl groups per repeat unit.

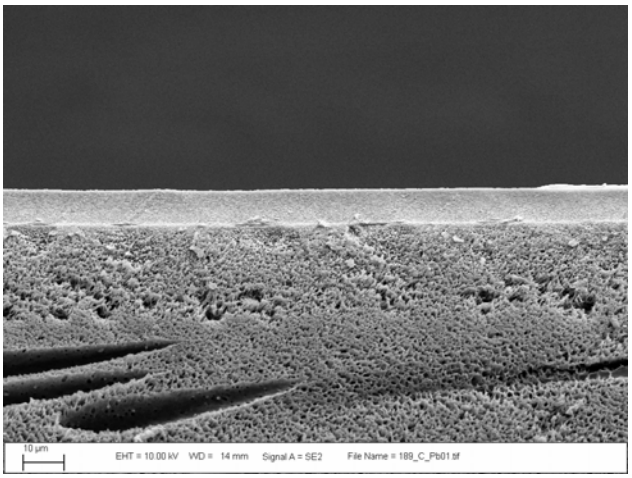

Figure 5-3 - SEM image of cross section of an ultrafiltration membrane with PS-QA1 coating.

image of a cross section of a coated membrane. A dense layer of PS-QA1 with a consistent thickness of 9 microns can clearly be seen on the porous poly(sulfone). Streaming potential measurements on these surfaces (Figure 5-4) showed that all of the coatings had positive charges consistent with the presence of quaternary ammonium groups on the polymers and in sharp contrast to the uncoated membrane which had a strongly negative surface charge. The electrostatic attraction between the negatively charged substrate and the positively charged coatings resulted in good adhesion of the coatings to the surface. The magnitude of the positive surface charge decreased as the length of the alkyl chain attached to the QA groups increased, indicating a tendency for the alkyl chains to mask the charged groups. Since all four PS-QA polymers were made from the same batch of Br-TMPS, the molar concentration of QA groups was the same for all of them. However, the number of QA groups per gram of polymer decreased slightly (from 1.9 to 1.7) as the length (and mass) of the alkyl chains was increased from one to twelve carbon atoms. Contact angle measurements (Figure 5-5) confirmed this

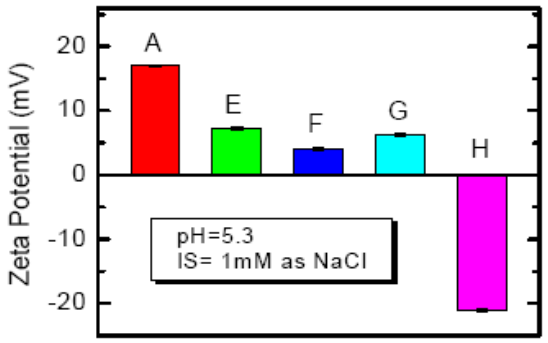

Figure 5-4 - Streaming potential measurements. A is coated with PS-QA1, E is coated with PS-QA8, F is coated with PS-QA10, G is coated with PS-QA12, and H is not coated.

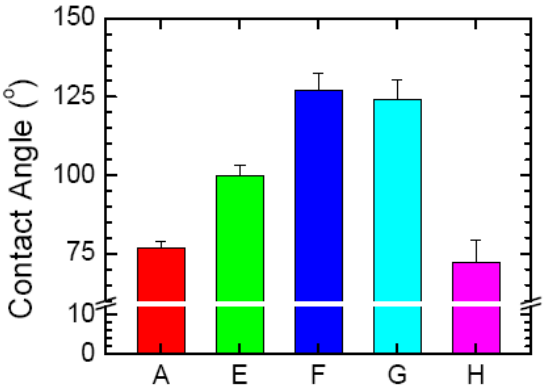

Figure 5-5 -Contact Angles. A is coated with PS-QA1, E is coated with PS-QA8, F is coated with PS-QA10, G is coated with PS-QA12, and H is not coated.

analysis by showing a trend in which the hydrophobicity of the surfaces generally increased as the length of the alkyl chains was increased.

5.4.2 Interaction forces with a negatively charged particle probe

Interaction forces between a silica colloid probe on an atomic force microscope tip and the coated surfaces were measured for both the approach (Figure 5-6a) and retraction (Figure 5-6b) of the probe. The interaction forces correlated strongly with the length of alkyl chains or hydrophobicity of the coated surfaces for both measurements. In the case of the retraction measurement on the PS-QA12 coating, the attractive force was always larger than the detection limit (20.8 mN/m) of the cantilever during the measurements. It is possible that the longer alkyl chain of the PS-QA12 polymer provided thicker polymer brush layer, and consequently, more chance to interact with the positively charged QA groups.

5.4.3 Antimicrobial effects of surface coatings

The attachment of *E. coli* cells to the coated surfaces also correlated well with the hydrophobicity (Figure 5-7). Experiments in two different media gave similar results, showing that the number of attached cells increased from about 1000 cells/cm^2 for PS-QA1 to an average of about 14,000 cells/cm^2 for PS-QA12. *E. coli* cells have a negative surface charge, so clearly the attraction between the cells and the coatings was not determined by electrostatic forces alone since the coating with the largest positive charge (PS-QA1) had the fewest cells attached. The PS-QA1 coated membrane even had fewer attached cells than the uncoated membrane (PS) which had a strongly negative surface charge. The attachment of cells appears to be most strongly influenced by the presence of hydrophobic alkyl chains attached to the QA groups. In a previous study of the interactions of cells with an immobilized QA coating with a 12-carbon alkyl chain, Nakagawa et al. concluded that the adsorption of cells was predominantly influenced by hydrophobic forces for samples with low QA salt content [*Nakagawa et al.*, 1984]. For that

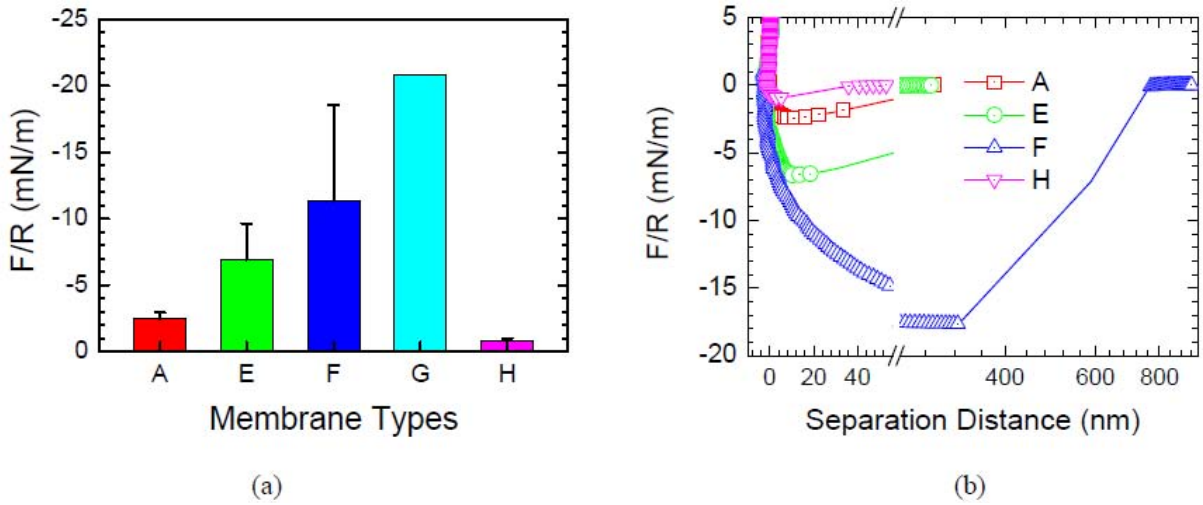

Figure 5-6 - Results of AFM force measurements between PS-QA coated membranes and a 3-micron silica colloid probe. (a) Average of normalized interaction force (n>60). (b) Representative retraction force curves. Interaction force of PS-QA12 was always larger than the detection limit (20.8 mN/m) of the cantilever during the measurements. A is coated with PS-QA1, E is coated with PS-QA8, F is coated with PS-QA10, G is coated with PS-QA12, and H is not coated.

case, the number of QA groups per gram of polymer (not including the glass substrate) was calculated to be approximately 2.7 for the coating with low QA salt content. Since the QA salt contents for all four PS-QA polymers were lower than that (1.9 to 1.7, as discussed above), our finding that the adhesion of cells corresponded strongly with the length of the alkyl chain on the QA groups was in agreement with the previous report.

The viability of the attached *E. coli* on the PS-QA coated membrane surfaces was measured by staining the cells with PI and CTC. PI stained only cells which had severe membrane damage or inactivated cells, while CTC stained metabolically active cells. In Figure 5-8, the numbers of live and dead cells are expressed as percentages of the total number of attached cells on each coating. All four PS-QA coatings showed significant biotoxicity with 80 to 90 % of the cells found to be inactivated as stained by PI. Conversely, no live cells were detected on any of the PS-QA surfaces as proven by CTC staining, whereas nearly all the cells on the uncoated membrane (PS) were determined to be metabolically active. The fact that all four QA coatings were approximately equally antimicrobial on contact was somewhat surprising, especially given the large variation in the number of attached cells on the coatings. Reports of

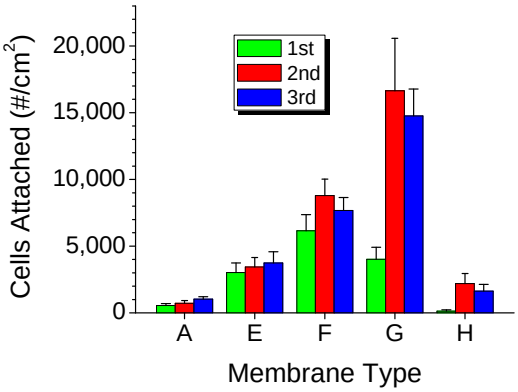

Figure 5-7 - Number of cells attached on coated membranes. A is coated with PS-QA1, E is coated with PS-QA8, F is coated with PS-QA10, G is coated with PS-QA12, and H is not coated.

water-soluble QA-containing polymers have indicated that their effectiveness against Gram-negative bacteria (such as E. coli) decreases as the hydrophobicity of the QA groups increase (i.e., longer alkyl chains) [*Ikeda and Tazuke*, 1984; *Dizman et al*., 2006]. Our results have shown that the most hydrophobic coating killed the greatest number of *E. coli* cells, however, this may simply be because more cells were attached to it than the other coatings.

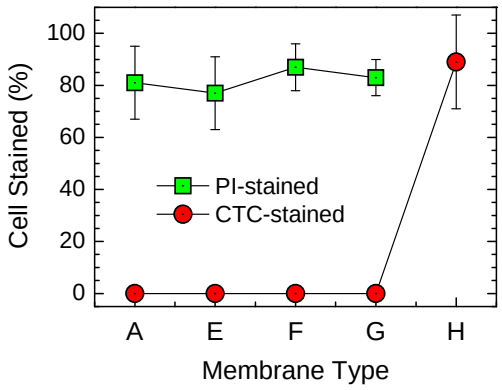

Figure 5-8 - Percentages of live and dead cells on coated membranes after 1h incubation with 10^6 *E. coli* cells/mL. Dead cells on the uncoated membrane could not be counted due to adsorption of the dye to the membrane. A is coated with PS-QA1, E is coated with PS-QA8, F is coated with PS-QA10, G is coated with PS-QA12, and H is not coated.

5.4.4 Biofouling of coated reverse osmosis membranes

Based on the results from Figures 5-7 and 5-8, it was determined that PS-QA1 was the most promising candidate for RO testing since it had the fewest cells attached and showed a biotoxicity equal to the other coatings. In accelerated biofouling tests in the crossflow system, the decrease in the rates of permeate flux through the coated membranes and the controls were essentially the same. Since this indicated that the coating probably had no effect on biofilm formation, a second test was run utilizing a half-coated membrane to allow for a better comparative imaging analysis. In this test, biofilm formation was not accelerated by the addition of organisms or nutrients in order to more closely approximate the environment of a real RO system. The PS-QA1 coating was applied to half of the membrane (lengthwise) and the test was allowed to run for 60 hours in the crossflow system. After the test, the membrane was stained with SYTO® 9 to indicate the presence of both live and dead cells. Figure 5-9 shows concentration images from part of this sample and Figure 5-9a clearly shows a much greater concentration of bacteria on the coated portion of the membrane. Although an exact ratio of live to dead cells could not be determined, Figure 5-9b indicates that a great many of the cells (probably a majority) are dead. This means that the positively charged PS-QA1 coating attracted organisms (as we expected) and was effective at killing them (as indicated in the biotoxicity testing). However, the dead cells were not removed by the flow of water across the surface of the membrane, thus allowing them to become a protective barrier between the coating and any new cells that contacted the surface.

5.5 CONCLUSIONS

The polysulfone made with tetramethyl bisphenol A was successfully functionalized with several different quaternary ammonium groups. The resulting ionomers were able to be dissolved in methanol through the use of an anionic surfactant. The ionomer solutions could be sprayed onto RO membranes to form uniform, well-adhered, water-permeable coatings. The coatings were all found to have significant biotoxicity. In RO crossflow testing of the coated membranes, the

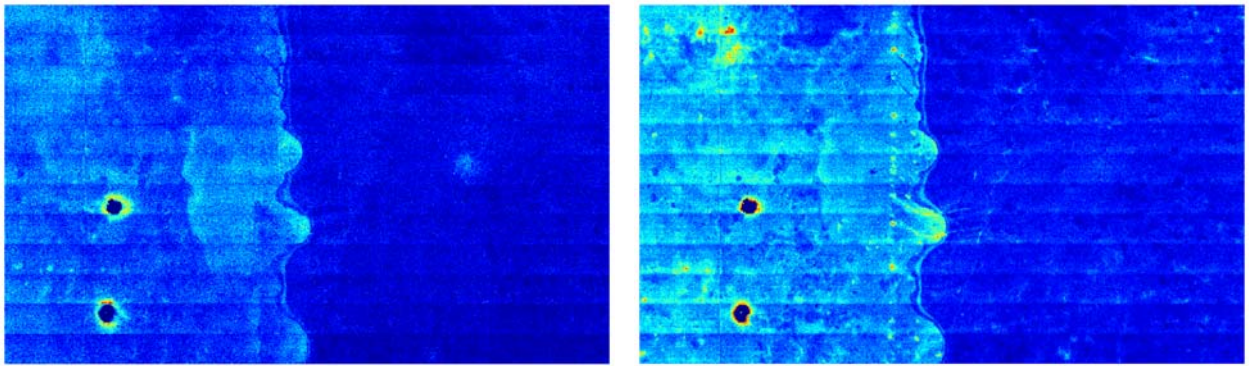

Figure 5-9. Concentration image of (a) SYTO® 9 stain and (b) PI stain on RO membrane after 60 hours in crossflow system test. The left half of the membrane was coated with PS-QA1. The right half was uncoated. SYTO® 9 stains both live and dead cells. PI stains only dead cells.

coatings did not prevent the formation of biofilms. The first cells to contact the surface in the RO tests were probably killed but they adhered to the surface and formed a barrier that prevented the coating from killing successive cells.

5.6 REFERENCES

Baker, J. S. and L. Y. Dudley (1998), Biofouling in Membrane Systems – A Review, *Desalination*, 118, 81.

Belfer, S., Y. Purinson, R. Fainshtein, Y. Radchenko, and O. J. Kedem (1998), Surface Modification of Commercial Composite Polyamide Reverse Osmosis Membranes, *J. Membr. Sci*., 139, 175.

Campbell, P. R. Srinivasan, T. Knoell, D. Phipps, K. Ishida, J. Safarik, T. Cormack, and H. Ridgway (1999), Quantitative structure-activity relationship (QSAR) analysis of surfactants influencing attachments of a Mycobacterium sp. to cellulose acetate and aromatic polyamide reverse osmosis membranes, *Biotechnol. and Bioeng*., 64, 527.

Cen, L., K. G. Neoh, and E. T. Kang (2003), Surface Functionalization Technique for Conferring

Antibacterial Properties to Polymeric and Cellulosic Surfaces, *Langmuir*, 19, 10295.

Dizman, B., M. O. Elasri, and L. J. Mathias (2006), Synthesis and Antibacterial Activities of Water-Soluble Methacrylate Polymers Containing Quaternary Ammonium Compounds, *J. Polym. Sci. Part A: Polym. Chem*., 44, 5965.

Haaland, D. M., J. A. Timlin, M. B. Sinclair, M. H. Van Benthem, M. J. Martinez, A. D. Aragon, and M. Werner–Washburne (2003), Multivariate curve resolution for hyperspectral image analysis: Applications to microarray technology, in *Spectral imaging: Instrumentation, applications, and analysis*, edited by R. M. Levenson, et al., International Society for Optical Engineering, San Jose, CA.

Hazziza-Laskar, J., G. Helary, and G. Sauvet (1995), Biocidal Polymers Active by Contact. IV. Polyurethanes Based on Polysiloxanes with Pendant Primary Alcohols and Quaternary Ammonium Groups, *J. Appl. Polym. Sci*., 58, 77.

Harrison, W. L., F. Wang, J. B. Mecham, V. A. Bhanu, M. Hill, Y. S. Kim, and J. E. McGrath (2003), Influence of the Bisphenol Structure on the Direct Synthesis of Sulfonated Poly(arylene ether) Copolymers, *J. Polym. Sci. Part A: Polym. Chem*., 41, 2264.

Ikeda, T. and S. Tazuke (1983), Biologically Active Polycations: Antimicrobial Activities of

Poly[trialkyl(vinylbenzyl)ammonium chloride]-type Polycations, *Makromol. Chem., Rapid Commun*., 4, 459.

Ikeda, T. and S. Tazuke (1984), Biologically Active Polycations 4, Synthesis and Antimicrobial Activity of Poly(trialkylvinylbenzylammonium chloride)s, *Makromol. Chem*., 185, 869.

Ikeda, T., H. Yamaguchi, and S. Tazuke (1990), Phase Separation in Phospholipid Bilayers Induced by Biologically Active Polycations, *Biochim. Biophys. Acta*, 1026, 105.

Isquith, A. J., E. A. Abbott, and P. A. Walters (1972), Surface-Bonded Antimicrobial Activity of an Organosilicon Quaternary Ammonium Chloride, *Appl. Microbiol*., 24, 859.

Isquith, A. J., E. A. Abbott, and P. A. Walters (1973), Method for Controlling the Growth of Algae in an Aqueous Medium, U. S. Patent 3,730,701.

Ju, H., B. McCloskey, A. Sagle, Y.-H. Wu, E. Van Wagner, H. B. Park, B. D. Freeman, L. Shimko, D. F. Lawler, and M. M. Sharma (2006), Synthesis and characterization of surface coated ultrafiltration membranes to enhance oil/water fouling resistance, *PMSE Preprints*, 95, 973.

Kang, S., M. Herzberg, D. F. Rodrigues, and M. Elimelech (2008), Antibacterial Effects of Carbon Nanotubes: Size Does Matter!, *Langmuir*, 24, 6409.

Kotula, P. G., M. R. Keenan, and J. R. Michael (2003), Automated analysis of sem x-ray spectral images: A powerful new microanalysis tool, *Microscopy and Microanalysis*, *9*, 1-17.

Krishnan, S., C. J. Weinman, and C. K. Ober (2008), Advances in Polymers for Anti-biofouling Surfaces, *J. Mater. Chem*., 18, 3405.

Lee, S. and M. Elimelech (2006), Relating Organic Fouling of Reverse Osmosis Membranes to Intermolecular Adhesion Forces, *Environmental Science and Technology*, 40, 980.

Louie, J. S., I. Pinnau, I. Ciobanu, K. P. Ishida, A. Ng, and M. Reinhard (2006), Effects of Polyether-polyamide Block Copolymer Coating on Performance and Fouling of Reverse Osmosis Membranes, *J. Membr. Sci*., 280, 762.

Mickols, W. E. (2001), Composite Membrane with Polyalkylene Oxide Modified Polyamide Surface, U.S. Patent 6,280,853.

Nakagawa, Y., H. Hayashi, T. Tawaratani, H. Kourai, T. Horie, and I. Shibasaki (1984), Disinfection of Water with Quaternary Ammonium Salts Insolubilized on a Porous Glass Surface, *Applied and Environmental Microbiology*, 47, 513.

Nurdin, N., G. Helary, and G. Sauvet (1993), Biocidal Polymers Active by Contact. II. Biological Evaluation of Polyurethane Coatings with Pendant Quaternary Ammonium Salts, *J. Appl. Polym. Sci.*, 50, 663.

Ottenbrite, R. M. and G. R. Myers (1973), Polyelectrolytes. Reaction of Ditertiary Amines with 2,3-Bis(bromomethyl)-1,3-butadiene, *J. Polym. Sci. Polym. Chem. Ed.*, 11, 1443.

Rao, A. P., N. V. Desai, and R. Rangarajan (1997), Interfacially Synthesized Thin Film Composite RO Membranes for Seawater Desalination, *J. Membr. Sci.*, 124, 263.

Rembaum, A., H. Rile, and R. Somoano (1970), Kinetics of Formation of High Charge Density Ionene Polymers, *J. Polym. Sci.*, B8, 457.

Rieser, T., K. Lunkwitz, S. Berwald, J. Meier-Haack, B. Kessler, and F. Simon (1997), Surface Modification of Microporous Polypropylene Membranes by Polyelectrolytes, *Polym. Mater. Sci. Eng.*, 77, 351.

Sinclair, M. B., J. A. Timlin, D. M. Haaland, and M. Werner-Washburne (2004), Design, construction, characterization, and application of a hyperspectral microarray scanner, *Applied Optics, 43*, 2079-2088.

Speier, J. L. and J. R. Malek (1982), Destruction of Microorganisms by Contact with Solid Surfaces, *Journal of Colloid and Interface Science*, 89, 68.

Tarboush, B. J. A., D. Rana, T. Matsuura, H. A. Arafat, and R. M. Narbaitz (2008), Preparation of Thin-Film-Composite Polyamide Membranes for Desalination Using Novel Hydrophilic Surface Modifying Macromolecules, *J. Membr. Sci.*, 325, 166.

Timlin, J. A., D. M. Haaland, M. B. Sinclair, A. D. Aragon, M. J. Martinez, and M. Werner-Washburne (2005), Hyperspectral microarray scanning: Impact on the accuracy and reliability of gene expression data, *Bmc Genomics*, 6.

Van Benthem, M. H., and M. R. Keenan (2004), Fast algorithm for the solution of large-scale non-negativity-constrained least squares problems, *Journal of Chemometrics, 18*, 441-450.

Walker, S. L., S. Bhattacharjee, E. M. V. Hoek, and M. Elimelech (2002), A Novel Asymmetric Clamping Cell for Measuring Streaming Potential of Flat Surfaces, *Langmuir*, 18, 2193.

Walters, P. A., E. A. Abbott, and A. J. Isquith (1973), Algicidal Activity of a Surface-Bonded Organosilicon Quaternary Ammonium Chloride, *Appl. Microbiol.*, 25, 253.

This page is intentionally left blank

6 DESIGN OPTIMIZATION OF ANTI-FOULING MICROMIXERS FOR REVERSE OSMOSIS MEMBRANES

Siri S. Khalsa and Clifford K. Ho

The following Section was published as part of the proceedings of the 23rd Annual WateReuse Symposium "***Water Reuse & Desalination: Solutions as Big as Texas***" held in Dallas, TX on September 7-10, 2008 (Khalsa and Ho, 2008) It is published with the permission of WateReuse.

6.1 Abstract

This paper describes a design analysis to optimize the shape of small protrusions (micromixers) fabricated on reverse-osmosis membranes with the objective of reducing biofouling by increasing the amount of turbulent mixing along the membrane surface. Micromixers have been experimentally and computationally shown to induce chaotic mixing and increase shear stress on the membrane surface. Computational fluid dynamics models of membranes imprinted with different micromixer patterns were developed to simulate the hydraulics and mass transfer within a membrane feed channel. The total simulated mass transfer of a tracer from the surface of the membrane and the pressure drop across the feed channel were used as metrics to compare the scouring effectiveness among the various micromixer patterns. The parameterization results indicate that the greatest scouring occurs when the chevron protrusion depth is maximized and the chevron pattern wavelength and spacing between chevrons are minimized. The same features that maximize scouring also increase the pressure drop. Operational factors and limitations need to be considered in real-world applications to maximize scouring while maintaining an acceptable pressure drop.

6.2 Introduction

Bacterial accumulation on membrane surfaces and the production of extracellular polymeric substance (EPS), or biofouling, is a significant problem for membrane-based separation processes, such as reverse osmosis and ultra- or nano-filtration. Biofouling decreases the efficiency of the filtration process by reducing flux through the membrane, decreasing the membrane lifetime, and consequently increasing energy and operational costs.

Conventional membrane modules employ spacers to physically separate the membranes and to potentially create additional mixing within the feed channel. Flow patterns and particle deposition around conventional spacer geometries and their effects on permeate flux and pressure drop have been simulated in both steady and unsteady models (Schwinge et al., 2004; Li et al., 2006). In addition, alternative shapes for spacers in membrane feed channels have been simulated (Karode and Kumar, 2001; Dendukuri et al., 2005). These studies focused on optimizing the hydraulics (i.e., minimizing the pressure drop) across the membrane feed channel for different spacer designs.

While computational analysis and evaluation of spacer designs has been prevalent in the literature, fewer studies have investigated biofouling and the impact of spacers (or turbulence promoters) on the onset and distribution of biofouling on membrane surfaces. Neal et al. (2003) performed experiments that illustrated the deposition pattern of particles in the vicinity of different filament orientations, but observed deposition patterns were not rigorously compared or correlated to computational simulations. Scott et al. (2000) performed experiments in a cross-flow test cell using flat and corrugated membranes. They found that the corrugated membranes yielded greater permeate flux than the flat membranes due to a combination of increased surface area and increased scouring via enhanced mixing, which Scott et al. (2000) postulated helped to disrupt the formation of concentration polarization and fouling. More recently, Ho et al. (2008) correlated simulated hydraulic metrics with biofouling on membrane surfaces.

The previous studies did not attempt to optimize the spacers or mixer designs based on performance metrics such as hydraulics or mixing. This paper describes a computational fluid dynamics (CFD) design analysis to optimize the dimensions of chevron-shaped micromixers that are fabricated directly on the membrane surface, with the objective of maximizing the amount of scouring and mixing along the membrane.

6.3 Development of CFD Model

Different micromixer designs were modeled and analyzed using SolidWorks 2004® and CFdesign v9®. The following sections describe the designs and methods associated with the development of the models.

6.3.1 Parameter Definitions

The flow of water through a membrane channel is modeled as a rectangular fluid slab. The top boundary of the slab represents the membrane surface (imprinted with micromixers), and the remainder of the volume represents the fluid region within the feed channel. Symmetry is employed so that only a small region of the feed channel is modeled.

A channel imprinted with micromixers is defined by seven parameters (see Figure 6-1). The array is symmetric about the channel length; hence the channel width is equivalent to the chevron wavelength. The number of chevron-shaped protrusions along the length of the channel is defined by the channel length, channel width, chevron spacing, chevron width, and chevron angle.

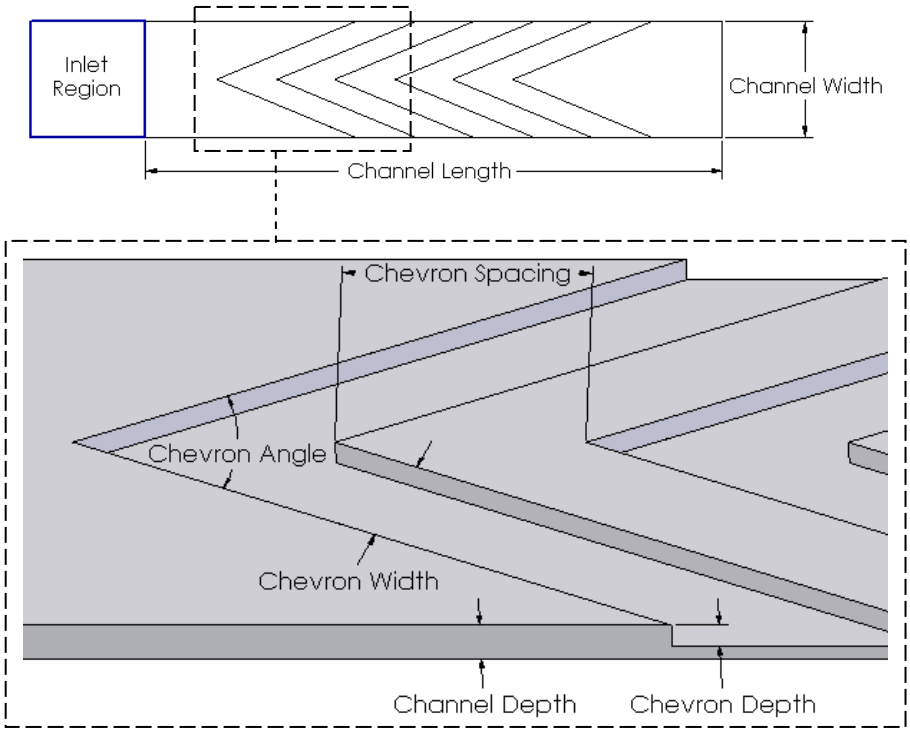

Figure 6-1. A membrane channel imprinted with micromixers is defined by seven dimensions. This figure shows one wavelength of the micromixer pattern.

6.3.2 Boundary Conditions

The boundary conditions along the top of the modeled domain (representing the membrane surface) are illustrated in Figure 6-2. The Slip / Symmetry boundary condition applied to all surfaces along the channel length prescribes symmetry along these surfaces (i.e., an infinitely repeating micromixer pattern). The flow solution is defined by a fixed velocity, applied by a channel width-dependent volume flow rate, at the inlet surface and a zero pressure at the outlet surface. The flow velocity is sufficiently low for laminar flow. No flow occurs through the top or bottom boundaries of the model domain. The permeate flux through the top boundary, which represents the membrane surface, is assumed to be negligible compared to the total cross flow through the channel. A normalized diffusive scalar, discussed below, is fixed with the value 0 on the inlet surface and 1 on the membrane surface. The scalar solution follows from the steady state flow solution.

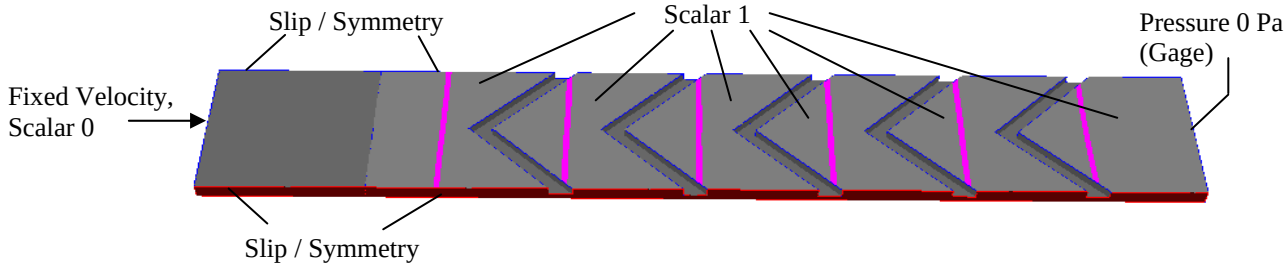

Figure 6-2. The boundary conditions applied to a 3D channel model in CFdesign®.

6.3.3 Performance Metrics

The simulated process of 'clean' incoming water (scalar = 0) mixing with the scalar applied along the membrane surface is analogous to clean water scouring bacteria from the membrane surface. The simulated bulk scalar concentration at the outlet surface, the *outlet scalar*, has been shown in some cases to be inversely proportional to the total microbial concentration on the membrane surface, measured experimentally (Ho et al., 2008). Hence, the outlet scalar is used as a measure of the amount of scouring along the membrane surface in this study.

The presence of micromixers demands an increased pressure drop across the channel in order to maintain a fixed flow rate through the system. Because the outlet pressure is prescribed to be zero (gage), the *inlet pressure* corresponds to the total pressure drop along the feed channel and is used as another performance metric.

The outlet scalar and inlet pressure are used in this study as metrics for comparing the potential scouring effectiveness and operational cost among configurations. The permeation flux and the impact of fouling on permeation flux were not modeled in these simulations.

6.3.4 Grid Development

Prior to running a CFdesign® analysis, the geometry was meshed using tetrahedral elements (to accommodate the complex geometries of the micromixers). If there are too few elements, a small change in the number of elements can significantly affect the analysis solution, and we say the solution is mesh-dependent. In order to ensure the mesh was sufficiently refined for the analysis solution to be considered mesh-independent, a grid convergence study was performed. Two different micromixer configurations were analyzed using a number of different mesh sizes, and the performance metrics were plotted against the number of mesh elements.

For the configurations used in this study, an element size of 0.5 mm (~100,000 elements) was found to be sufficiently refined for a mesh-independent solution. Figure 6-3 displays the mesh of a configuration with this refinement. The mesh is automatically enhanced near edges, which are

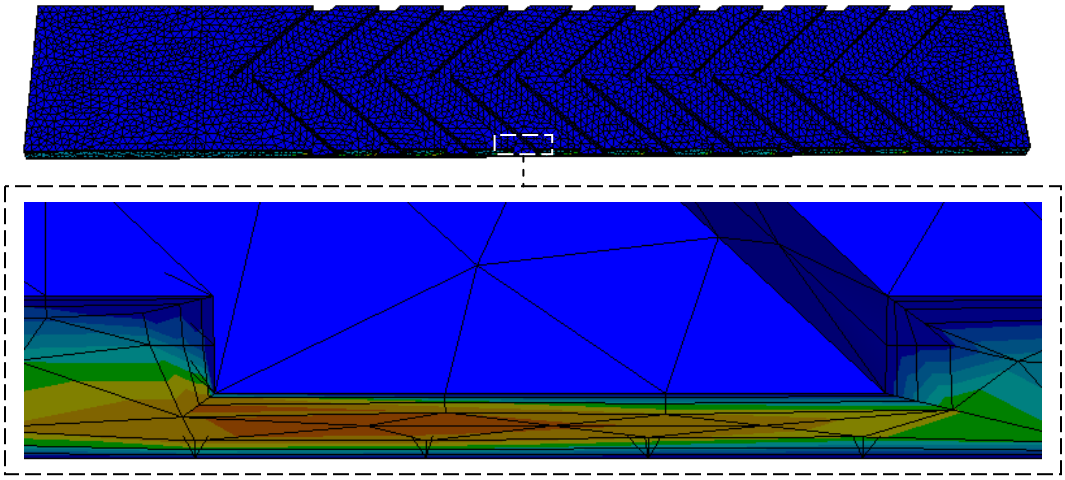

Figure 6-3. The mesh of a configuration with 0.5 mm tetrahedral elements. The mesh is enhanced in high-gradient regions.

high-gradient regions that require a greater resolution.

6.3.5 Parameterization

The design analysis described in this paper is a 4-factor, 3-level parameterization. The channel depth and channel length are held constant; while the channel width, chevron depth, chevron angle, and chevron spacing are varied with low, middle, and high values. At the time of this parameterization, the process of fabricating epoxy micromixers onto membranes required the chevron width to be twice the chevron depth. To simulate this process, the chevron width was set at twice the chevron depth for every configuration in this parameterization. The parameters used to generate the 81 different configurations are listed in Figure 6-4.

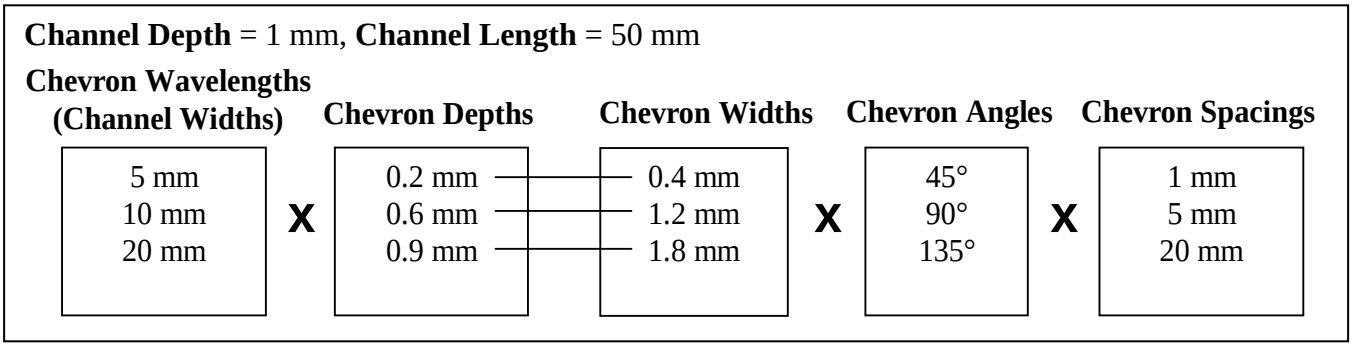

Figure 6-4. Four parameters are varied with low, middle, and high values. The chevron width is set at twice the chevron depth.

The parameterization results can be quantified by conducting an analysis of variance (ANOVA) on the results. This parameterization has four factors (channel width, chevron depth, chevron angle, and chevron spacing), each with three levels (low, middle, and high). One ANOVA method is to evaluate the mean of the dependent variable (outlet scalar) when each factor is set low, middle or high. For linear effects, the difference between these means when each factor is set high or low is called the effect estimate. If the factor does not impact the results, the difference between the two means should be small. For quadratic effects, the effect estimate is the difference between the mean response at the middle settings and the combined high and low settings for the respective factors. The ANOVA effect estimate was calculated using Statistica,™ a commercial statistical-analysis software package.

6.3.6 3D Model Examples

Figure 6-5a displays the configuration with all parameters set at their middle values. For an understanding of how each parameter influences the geometry, compare Figures 6-6 – 6-9 with Figure 6-5. The parameters altered from that of Figure 6-5 are printed in *italics*. Note that the number of micromixers is maximized for each configuration.

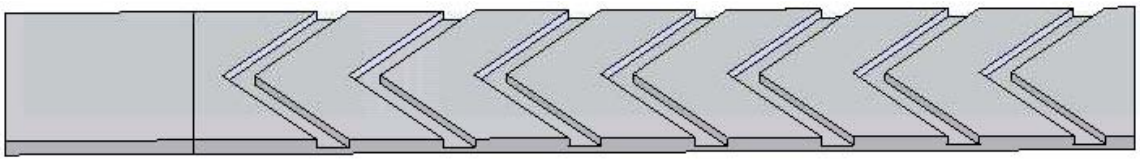

Figure 6-5. Depth = 1mm, Channel Width = 10mm, Channel Length = 50mm, Chevron Depth = 0.6mm, Chevron Width = 1.2mm, Chevron Angle = 90°, Chevron Spacing = 5mm

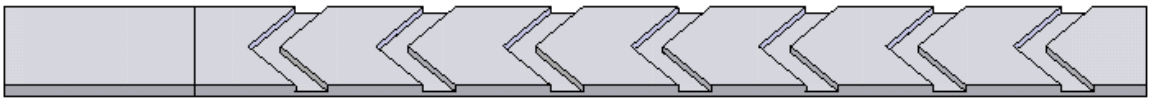

Figure 6-6. Channel Depth = 1mm, *Channel Width = 5mm*, Channel Length = 50mm, Chevron Depth = 0.6mm, Chevron Width = 1.2mm, Chevron Angle = 90°, Chevron Spacing = 5mm

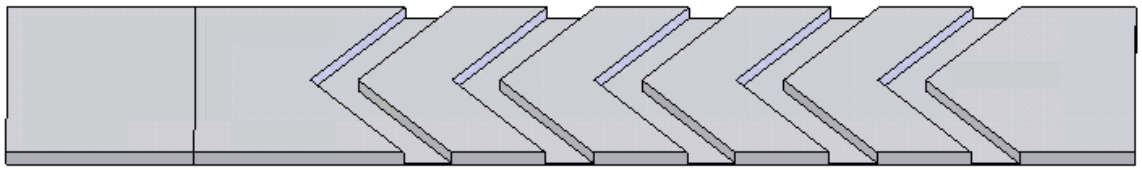

Figure 6-7. Channel Depth = 1mm, Channel Width = 10mm, Channel Length = 50mm, *Chevron Depth = 0.9mm, Chevron Width = 1.8mm*, Chevron Angle = 90°, Chevron Spacing = 5mm

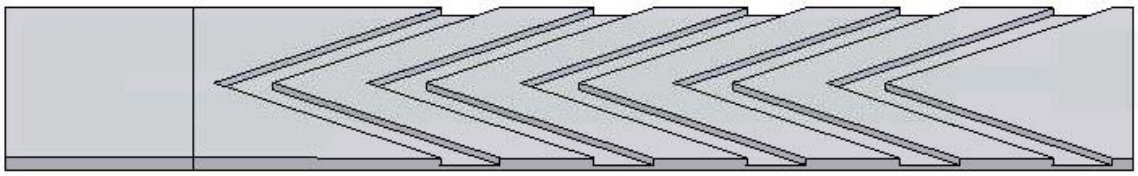

Figure 6-8. Channel Depth = 1mm, Channel Width = 10mm, Channel Length = 50mm, Chevron Depth = 0.6mm, Chevron Width = 1.2mm, *Chevron Angle = 45°*, Chevron Spacing = 5mm

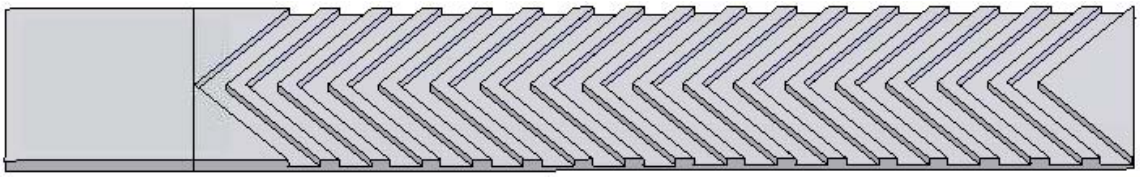

Figure 6-9. Channel Depth = 1mm, Channel Width = 10mm, Channel Length = 50mm, Chevron Depth = 0.6mm, Chevron Width = 1.2mm, Chevron Angle = 90°, *Chevron Spacing = 1mm*

6.4 Results and Discussion

6.4.1 Statistical Analysis

The effect estimate was standardized by dividing the effect by the standard error of the sample population (standard deviation divided by the square root of the sample size). The standardized effect on the outlet scalar was plotted using Statistica™ and is shown in Figure 6-6. The linear effect is marked with an L next to the factor name, and the quadratic effect is marked with a Q next to the factor name. The linear-by-linear interaction effect (marked by #L by #L, where each

number represents the factor it prefixes in Figure 6-10) can be interpreted as half the difference between the linear effect of one factor at the high and low settings of another. A greater standardized effect magnitude indicates a more statistically significant effect. The p-value, marked by a dotted red line, is associated with the probability that the test statistic for a given factor is significant relative to the intrinsic variability of the data. Effects that do not cross the p-value are considered statistically insignificant.

The significant effects on the outlet scalar indicated by Figure 6-6 are as follows, in decreasing order of statistical significance:

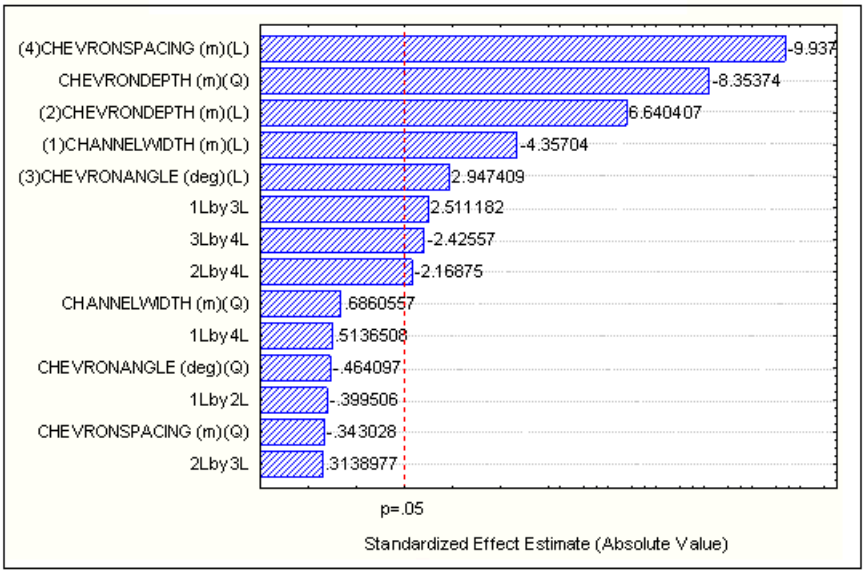

Figure 6-10. Pareto chart of standardized effects of the 4 3-level factors on the outlet scalar.

1) Chevron spacing linear effect: low chevron spacing results in a high outlet scalar.

2) Chevron depth quadratic effect: middle chevron depth results in a low outlet scalar. Given the flow analysis in the next section, we would expect that increasing the chevron depth always increases the outlet scalar. However, this quadratic effect most likely results from the chevron width-depth coupling (the chevron width was set to twice the chevron depth for each configuration). An increase in the chevron depth increases the chevron width, which reduces the membrane surface area available to supply the diffusive scalar. The increased chevron width also can reduce the number of chevrons that can fit on the fixed channel length, for some configurations. For the middle chevron depth, the scouring is not effective enough to compensate for the decreased membrane surface area and potentially fewer chevrons.

3) Chevron depth linear effect: high chevron depth results in a high outlet scalar. Scouring is effective enough in the case of high chevron depth to compensate for the decreased membrane surface area and potentially fewer chevrons.

4) Channel width (chevron wavelength) linear effect: low channel width results in a high outlet scalar.

Of less statistical significance are the linear effect of the chevron angle and its linear-by-linear interaction effects with the channel width and the chevron spacing. More data is needed to determine the effect of chevron angle on scouring effectiveness.

Figure 6-11 is the corresponding Pareto chart of standardized effects for the inlet pressure. Figure 6-11 indicates that the inlet pressure was most significantly affected by chevron depth, followed by the chevron spacing. High chevron depth or low chevron spacing resulted in a high inlet pressure. The linear effect of the chevron angle and its linear-by-linear interaction effect with the chevron depth have a relatively low statistical significance.

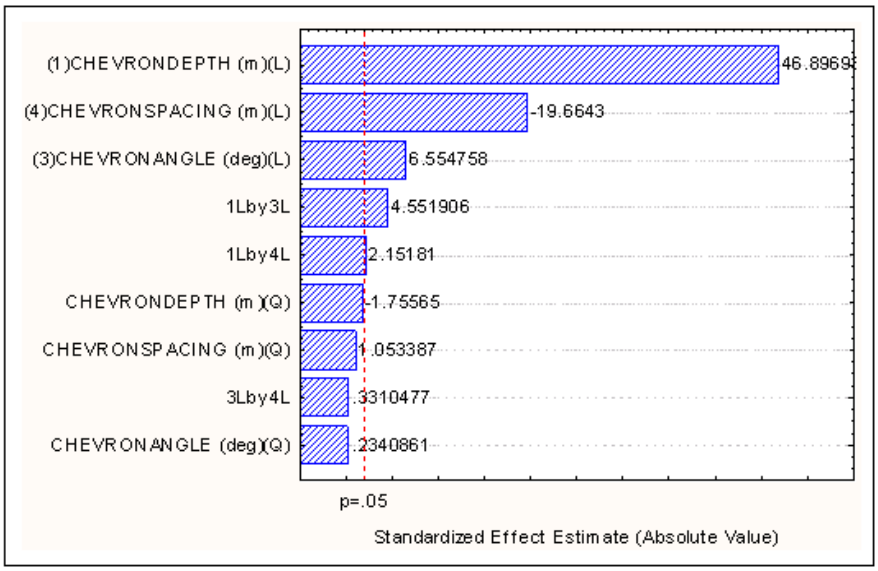

Figure 6-11. Pareto chart of standardized effects of the 4 3-level factors on the inlet pressure.

6.4.2 Flow Analysis

This section examines the physical basis for the increased scouring that results from a deeper chevron depth. Consider a configuration with a chevron depth of 0.9 mm and a channel depth of 1 mm. Figure 6-12 displays the velocity vectors along three planes perpendicular to the membrane. The flow downstream of the chevron peaks is accelerated toward the membrane

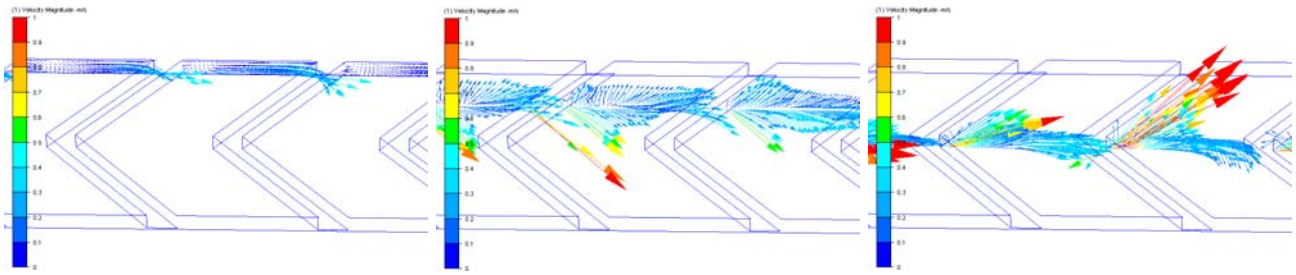

Figure 6-12. Velocity vectors indicate that flow downstream of peaks is accelerated toward the membrane in the case of deep chevron protrusions.

surface. We expect that this high velocity flow directed toward the membrane results in scouring on the membrane surface.

To understand the mechanism by which this acceleration takes place, consider the flow traces illustrated in Figure 6-13. The tracers are colored by the z-component of the velocity, which is the component normal to the membrane surface. The velocity is increased beneath the chevrons due to the decrease in the height of the flow. The flow thus follows the path of least action by bending perpendicular to the chevrons. This bending results in a convergence of the flow downstream of the 'peaks' (left-pointing chevrons), and a divergence of the flow downstream of the 'valleys' (right-pointing chevrons).

The flow convergence downstream of the peaks results in a high-gradient pressure distribution, as shown in Figure 6-14. A low pressure region immediately downstream of the peak and along the membrane is surrounded by higher pressure regions. The flow downstream of the peaks is thus forced toward the top of the channel. In contrast, no such high-gradient pressure distribution results from the flow divergence downstream of the valleys, so the flow downstream of the valleys does not accelerate toward the membrane surface.

Now consider a configuration with a chevron depth of 0.4 mm, but with all other dimensions identical to the deep chevron case. The flow traces for this configuration, again colored by the component of the velocity normal to the membrane surface, are shown in Figure 6-15. In this case of shallow chevron depth, the flow downstream of the peaks is not significantly accelerated toward the membrane surface. The velocity is not significantly higher beneath the chevrons, so the flow convergence downstream of the peaks is far less pronounced.

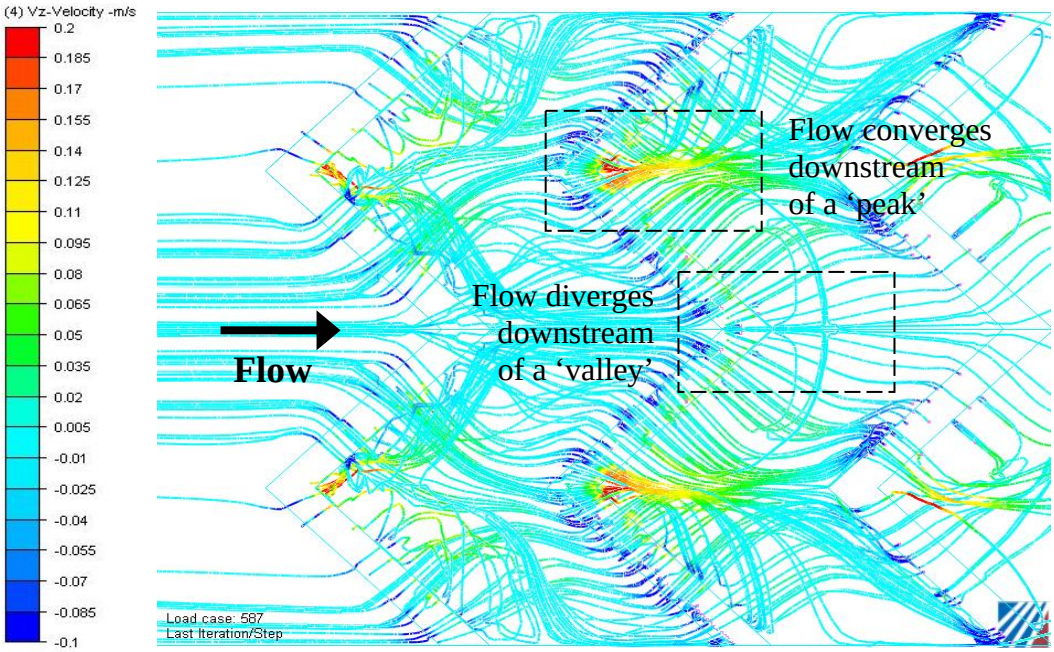

Figure 6-13. Flow traces for the deep chevron case, colored by the component of the velocity normal to the membrane surface. The flow converges downstream of the 'peaks' and diverges downstream of the 'valleys'.

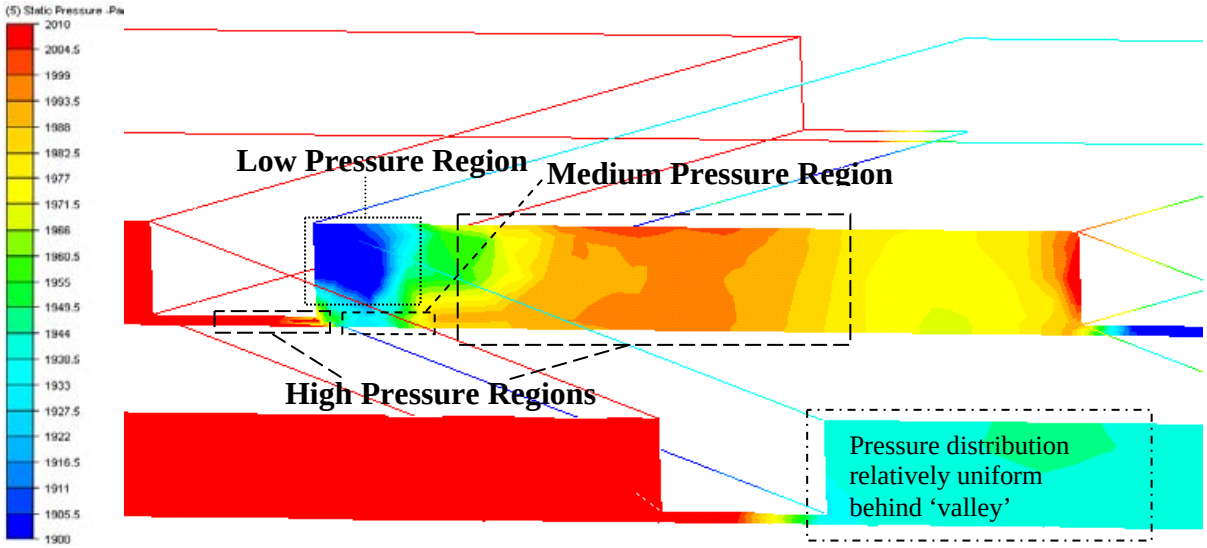

Figure 6-14. Pressure distributions downstream of a peak and a valley for the deep chevron case. The high pressure gradient downstream of the peak accelerates the flow toward the membrane surface.

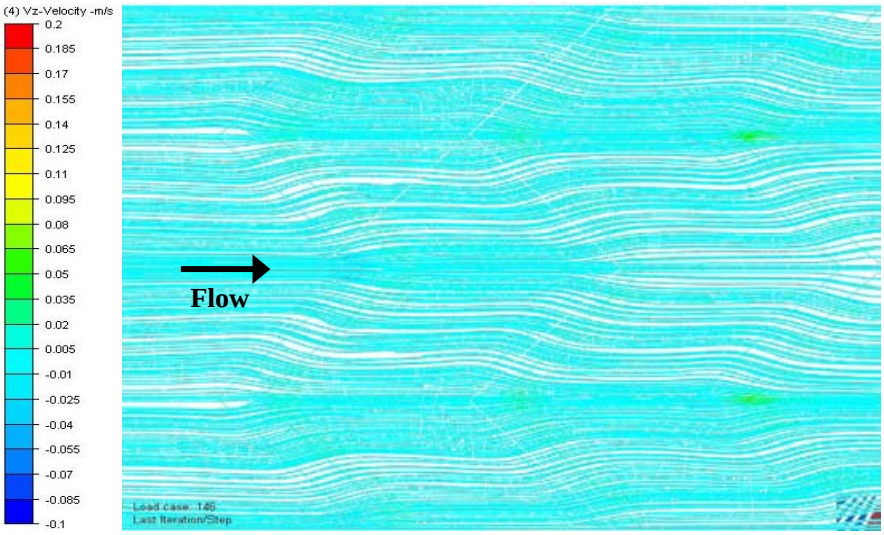

Figure 6-15. Flow traces for the shallow chevron case, colored by the component of the velocity normal to the membrane surface. The flow convergence is less pronounced, and the flow is not significantly accelerated toward the membrane surface.

As a result, the pressure gradient downstream of the peaks is not as steep, as shown in Figure 6–16. Hence, the flow is not significantly accelerated toward the membrane surface.

We can thus expect that maintaining a large number of deep chevron peaks per unit area of membrane would improve scouring, by creating more regions of high velocity flow toward the membrane surface. Both smaller chevron spacing and smaller channel width (chevron

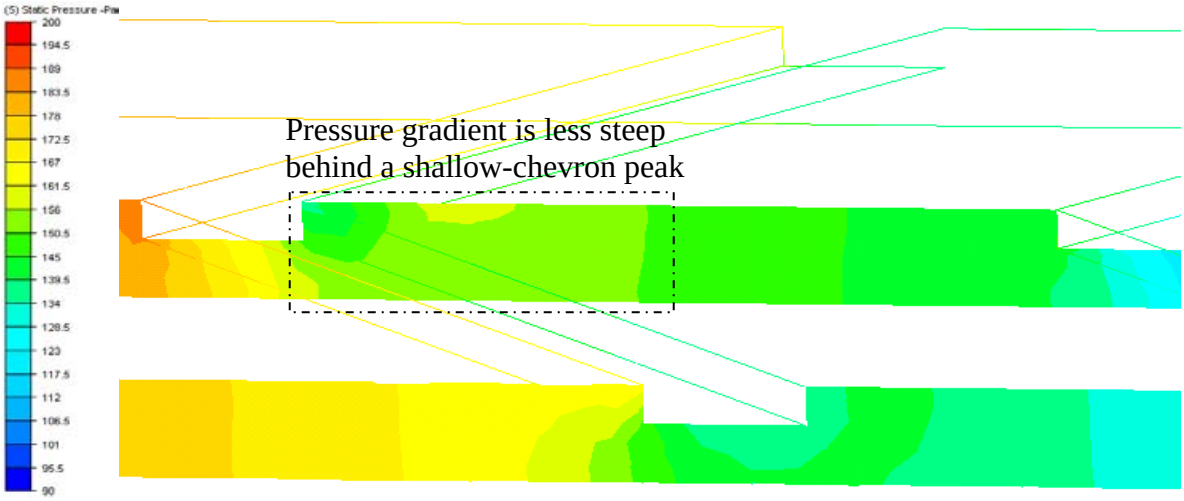

Figure 6-16. Pressure distributions downstream of a peak and a valley in the shallow chevron case. The pressure gradient is not steep enough to significantly accelerate the flow toward the membrane surface.

wavelength) provide a larger number of chevron peaks per unit area and hence increase scouring along the membrane, as indicated by the parameterization.

6.5 Conclusions

The most statistically significant effects on scouring effectiveness are, in decreasing order of importance, the chevron spacing, the chevron depth, and the chevron pattern wavelength. The parameterization results indicate that greater scouring occurs on the membrane when the chevron protrusion depth is maximized and the chevron pattern wavelength and spacing between chevrons are minimized. The correlations between these three parameters and scouring effectiveness were examined based on hydraulic considerations. The chevrons were found to focus the flow downstream of the peaks, producing high-gradient pressure distributions that accelerated the flow toward the membrane surface, resulting in increased scouring. Minimizing the chevron spacing and chevron pattern wavelength maintains a large number of chevron peaks per unit area of membrane, and each peak produces a region of high velocity flow toward the membrane surface, resulting in increased scouring. The effect of the chevron angle was found to be less statistically significant than the other three parameters, and more data is needed to determine the effect of chevron angle on scouring effectiveness.

The inlet pressure was most significantly affected by chevron depth, followed by chevron spacing. Greater chevron depth or lower chevron spacing resulted in a higher inlet pressure. Therefore, the same features that maximize scouring also increase the pressure drop. Operational factors and limitations need to be considered in real-world applications to maximize scouring while maintaining an acceptable pressure drop.

6.6 References

Dendukuri, D., Karode, S., Kumar, A., (2005) Flow visualization through spacer filled channels by computational fluid dynamics - II: improved feed spacer designs. J. Membrane Science. 249, 41-49.

Ho, C.K., Altman, S.J., Jones, H.D.T., Khalsa, S.S., McGrath, L.K., Clem, P.G., 2008. (in press). Analysis of Micromixers to Reduce Biofouling in Reverse-Osmosis Membranes. Accepted for publication in the Desalination - Outstanding Papers from NAMS 2007 special issue of Environmental Progress.

Karode, S.K., Kumar, A., (2001) Flow visualization through spacer filled channels by computational fluid dynamics - I: Pressure drop and shear rate calculations for flat sheet geometry. J. Membrane Science. 193, 69-84.

Li, Y.-L., Chang, T.-H., Wu, C.-Y. , Chuang, C.-J., Tung, K.-L., (2006) CFD Analysis of Particle Deposition in the Spacer-Filled Membrane Module. J. Water Supply Research and Technology –AQUA. 55(7-8), 589-601.

Neal, P.R., Li, H., Fane, A.G., Wiley, D.E., (2003) The effect of filament orientation on critical flux and particle deposition in spacer-filled channels. J. Membrane Science. 214, 165-178.

Schwinge, J. Neal, P.R., Wiley, D.E., Fletcher, D.F., Fane, A.G., (2004) Spiral wound modules and spacers: review and analysis. J. Membrane Science. 242, 129-153.

Scott, K., Mahmood, A.J., Jachuck, R.J., Hu, B., (2000) Intensified membrane filtration with corrugated membranes. J. Membrane Science. 173, 1-16.

7 COMPUTATIONAL FLUID DYNAMICS SIMULATIONS OF MEMBRANE PROCESSES

Stephen W. Webb and Darryl L. James

The FLUENT (Fluent, Inc., 2006a) computational fluid dynamics (CFD) code has been used to simulate membrane processes including water and salt flow across the membrane, concentration polarization, and particle trajectories. The model is part of a larger project to evaluate the use of micmicromixers to control biofouling on the surface of water-treatment membranes. Micromixers are defined as features that promote chaotic mixing. In this case, the micromixers are chevrons printed on the surface of the membrane. More details about the micromixers are presented in Sections 0 and 3. The chevrons change the local water and salt flow patterns across the membrane including the concentration polarization. Simulation of these membrane processes with chevrons, including detailed velocity and concentration fields, is important in evaluating the change in membrane salt rejection due to these chevrons and as flow conditions for particle tracking simulations. The ultimate goal is to have the CFD model fully linked to DAKOTA (see Section 8) for a complete optimization of the chevron configuration to minimize the attachment of the particles to the membrane surface.

In order to investigate the biofouling potential of various membrane configurations including chevrons, particle tracking has been added to the FLUENT membrane simulations. The biofouling potential is assumed to be related to the ability of particles to contact and stick to the membrane surface. The membrane template described below has been used to calculate the flow and salt concentration details for the membrane including chevrons. Particle tracking has been used to determine the affinity of micron-sized particles to the surface of the membrane including the spatial distribution.

7.1 Flow Across Membranes

The flow of water and brine across membranes is an important physical process that cannot be simulated by standard CFD codes including those discussed in Sections 2 and 6. The preferential flow of water across a membrane is essential to the desalination process and results in a buildup of brine concentration at the membrane surface (concentration polarization) that also affects the water flux across the membrane through the local osmotic pressure, which is approximately 380 psi for typical 3.5% seawater.

The flow of water and salt across membranes is simulated by the FLUENT computational fluid dynamics code (Fluent, Inc., 2006a). Code modifications were made to FLUENT to perform these calculations by adding water and salt mass sources and sinks to the membrane surface (Fluent, 2006b). The value of the sources and sinks for water and brine are described below.

The flux of water through the membrane is modeled as a function of the net pressure difference across the membrane including the solute osmotic pressure (Rautenbach and Albrecht, 1989).

$$J_w = A^* (P_u - P_d - (\pi(C_u) - \pi(C_d)))^*\rho_w \quad (7\text{-}1)$$

$$\pi(C) = K^*C \quad (7\text{-}2)$$

The salt flux across the membrane is dependent on the salt concentration difference between upstream (feed) and downstream (permeate) of the membrane.

$$J_s = B\,(C_u - C_d) \quad (7\text{-}3)$$

Salt and water concentrations needed in above expressions can be calculated as follows:

$$C = \rho_{mix}{}^*Y_s \quad (7\text{-}4)$$

The mixture density is calculated with a volume weighted mixing law:

$$\rho_{mix} = 1/(Y_s/\rho_s + Y_w/\rho_w) \quad (7\text{-}5)$$

where,

J = Flux across the membrane (kg/m^2-s)
ρ = Density (kg/m^3)
P = Pressure (Pa)
π = Osmotic pressure (Pa)
C = Salt concentration (kg/m^3)
Y = Mass fraction
Index w: water
Index s: salt
Index mix: mixture
Index u: upstream
Index d: downstream
K = Osmotic Pressure Factor (Pa-m^3/kg)
A = Membrane Constant (m/s-Pa)
B = Membrane Constant (m/s)

The modifications to FLUENT to simulate water and salt flow across membranes have been verified by comparison to various thermodynamic limits on membrane performance as by Song et al. (2003) and to a membrane performance curve by Song and Tay (2006) as detailed by Webb (2007).

7.2 Particle Tracking

In the particle tracking simulations, the particle is assumed to be spherical and 1 micron in diameter with the density of pure water. The particle will experience several forces of varying magnitude depending on the shape of the particle, distance to other objects, and the flow rate. The particle concentration is assumed to be dilute and therefore no particle-particle interaction was considered. The standard version of FLUENT includes particle tracking with numerous forces. However, forces for a particle as it approaches a wall, which are significant, are not

included in the standard force balance. In addition, electrostatic forces are not included in the standard approach. The lift force has also been modified from the standard definition. These forces have been added through existing user interfaces, or User-Defined Functions (UDFs).

The following forces are included in the particle momentum balance

- electrostatic forces, including van der Waals force
- drag including the effect of flow across the membrane,
- repulsion as the particle approaches the membrane surface, and
- lift near the membrane wall

as discussed in detail below.

7.2.1 Electrostatic Forces

The electrostatic properties of the particles are based on the particle and membrane surface properties discussed in Kang et al. (2004). As a charged particle nears a charged surface, Electric Double Layer (EDL) and van der Waals forces become significant (typically this distance is of the order 1 nm depending on the Debye length and other factors). As discussed in Kang et al. (2004), the zeta potential (ζ_p) is assumed to be – 20 mV for the particles and– 28 mV for the membrane (ζ_m). The ionic strength was assumed to be 0.001mol/l, pH ~ 6, and the corresponding Debye length (κ^{-1}) is about 10 nm.

The equation for the EDL and van der Waals forces was taken from Kang et al. (2004):

$$F_{EDL} = 2\pi b\varepsilon\varepsilon_o\kappa\left(\zeta_m^2+\zeta_p^2\right)\left(\frac{2\zeta_m\zeta_p}{\zeta_m^2+\zeta_p^2}-e^{-\kappa\hat{h}}\right)\left(\frac{e^{-\kappa\hat{h}}}{1-e^{-2\kappa\hat{h}}}\right) \tag{7-6}$$

where ε and ε_o are the relative permittivity of water and free space, 78.4 and $8.85\text{x}10^{-12}$, respectively, $\hat{h}$ is the interfacial separation distance, and κ is the inverse Debye length.

The van der Waals force expression between a sphere and a flat wall is calculated from

$$F_{vdW} = \frac{A_H b}{6h^2(1+5.3(h/\lambda))} \tag{7-7}$$

where the Hamaker constant, A_H, of 1kT is assumed, the characteristic wavelength, λ, is taken at 100 nm as given in Kang et al. (2004), and b is the particle radius.

7.2.2 Drag Force

Particle drag is the primary force that moves the particles through the fluid in the modeled RO system. The small diameter of the particle coupled with the bulk flow velocity results in a particle Reynolds number typically much less than 1 such that Stokesian drag can be used.

Morsi and Alexander (1972) developed an expression for the drag force per particle mass. This expression fits experimental drag data for a particle assuming no particle-particle or particle-wall interaction and is given by:

$$F_i = \tfrac{1}{2} C_d \rho_f A V_{s,i}^2 \tag{7-8}$$

where the subscript f denotes the fluid and s denotes slip. $V_{s,i}$ is the respective slip velocity in the i^{th} direction (for example in the x direction $V_{s,I} = U_f - U_p$, which is the difference between the fluid velocity and the particle velocity in the x-direction). *A* is the frontal area of the particle and the drag coefficient, C_d, is given by an expression that depends on the particle Re:

$$C_d = \frac{K_1}{\mathrm{Re}_p} + \frac{K_2}{\mathrm{Re}_p^2} + K_3 \tag{7-9}$$

The terms, K_1, K_2 *and* K_3, in the drag coefficient expression, Equation 7-9, are dependent on the Reynolds number up to a maximum particle Reynolds numbers of 50,000. In the Stokesian limit (Re < 1.0), the drag coefficient is given by 24/Re, so Equation 7-9 becomes the well know Stokesian drag,

$$F_i = 6\pi\mu b V_s \,. \tag{7-10}$$

As the particle nears a wall, or the RO membrane for the system being modeled, the particle drag given by Equation 7-9 needs to be modified. There are two effects that need to be added – the effect of the wall that leads to a repulsive force away from the wall, and the compensating effect of flow through the membrane wall that partially negates this repulsive force.

7.2.3 Repulsive Force

Brenner (1961) calculated a correction factor, λ, that is applied to the Stokes drag law in the presence of a solid wall for the case of negligible particle and fluid inertia for a particle moving in a stagnant fluid:

$$F = -6\pi\mu b V_p \lambda \tag{7-11}$$

where *b* is the particle radius, V_p is the particle velocity component normal to the wall, and λ is the correction factor determined by an infinite series expansion that is a function of h/b (h is the distance from the wall to the particle centroid). Brenner notes that this force is always repulsive (i.e. in the opposite direction of the outward wall normal), regardless of whether the particle is moving toward or away from the wall. The influence of the wall increases as the particle approaches the wall.

Cox, and Brenner (1967) revisited the problem to include fluid inertia. Their expression for the drag force correction, or repulsive force, near an impermeable wall is given by:

$$\frac{F}{6\pi\mu b V_p} = -\frac{1}{\varepsilon}\left[1 + \frac{1}{5}\left(1 + \frac{1}{2}\mathrm{Re}\right)\varepsilon \ln\frac{1}{\varepsilon}\right] \tag{7-12}$$

where ε = (h-b)/b; h is the distance from the wall to the particle center. The Reynolds number is positive as the particle moves toward the wall and negative as the particle moves away from the wall. Note that the right hand side of Equation 7-12 is effectively λ in Equation 7-11.

The two expressions (Equation 7-11 and 7-12) are compared in Figure 7-1 for two values of the Reynolds number, or Re = 0 and 1. From this figure, it is clear that the fluid inertial affects are negligible for Stokesian flow, and that Equation 7-11 and 7-12 predict essentially the same results for the presence of a non-permeable wall.

These results are for an impermeable wall. As discussed above, for the problem being modeled, the RO membrane is permeable and therefore some flow passes through the membrane. An additional correction to Brenner's repulsive force, which reduces the effect, is required due to flow through the membrane. Goren (1979) developed an analytical model to predict the repulsive drag force on a particle near a permeable surface for finite values of the Darcy group (γb), where γ is equal to the product of the membrane thickness and the inverse of the permeability, or

$$F_{\infty} = -6\pi\mu b V_p \tag{7-13}$$

$$F / F_{\infty} = \Phi(h/b, \gamma b) \tag{7-14}$$

Goren's expression for the drag force is not easily reproduced, but he provides a table and graph of his predictive drag force compared to an impermeable surface (i.e. force predicted by Brenner, see Eqs. 7-3 and 7-4) for values of the Darcy group (γb) up to a value of 10^6 as well as

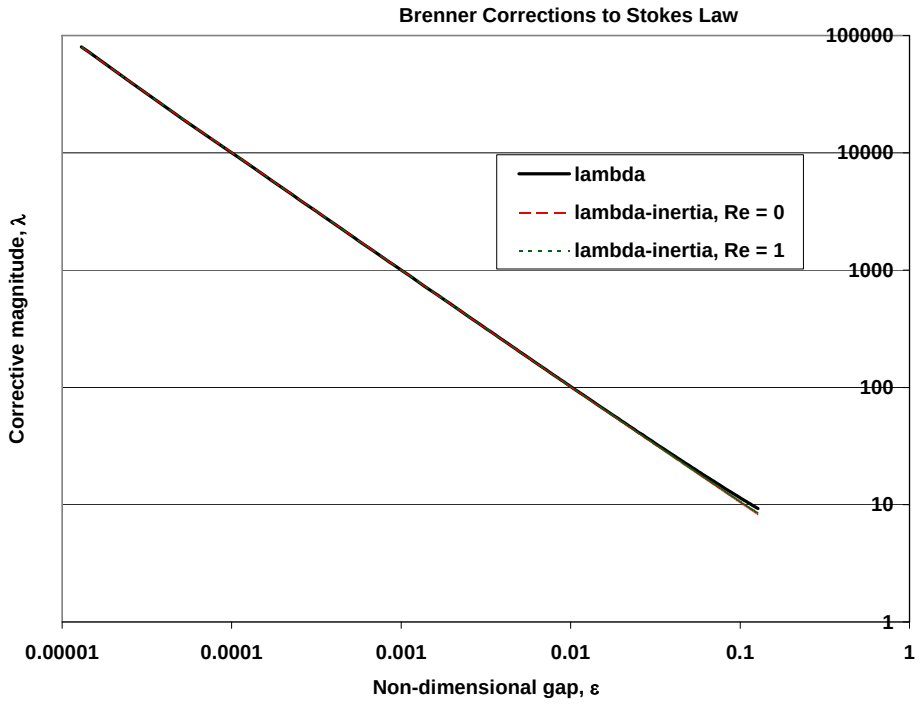

Figure 7-1. Comparison of predicted correction to Stokes drag law for Eqs. 7-11 and 7-12.

an equation for the asymptotic force as the gap goes to zero. Note that for a typical RO membrane with a membrane constant (A) of 8. x 10^{-12} m/s-Pa and a particle diameter of 1 micron, the Darcy group value is ~10^8, or well above the range of values included in Goren (1979). A plot of Brenner's and Goren's drag correction for two Darcy groups is given in Figure 7-2. The curve for the Darcy group value of 10^6 is based on the values given by Goren (1979). The curve for a Darcy group value of 10^8 is based on the asymptotic force value given by Goren (1979). This extrapolated curve is similar in shape to the other curve but with a discontinuity in slope as it approaches the Brenner limit. Continuity in the force multiplier functions is not deemed to be critical for this application.

7.2.3.1 Total Repulsive Force

The expressions given above are for the total force on the particle in the Stokes regime as the particle approaches the wall and are a function of the particle velocity. Because the drag force is already calculated by Eqs. 7-8 and 7-9, the net repulsive force (increase over the no-wall case) needs to be added to the particle momentum balance. Therefore, the net repulsive force is simply

$$F_{rep} = 6\pi\mu b V_p(\lambda - 1) \tag{7-15}$$

where the far-field value of this force equals the Stokesian value.

The total force is the sum of the drag force calculated by Eqs. 7-8 and 7-9 and the net repulsive force given above. The following net drag force equation is used for the component

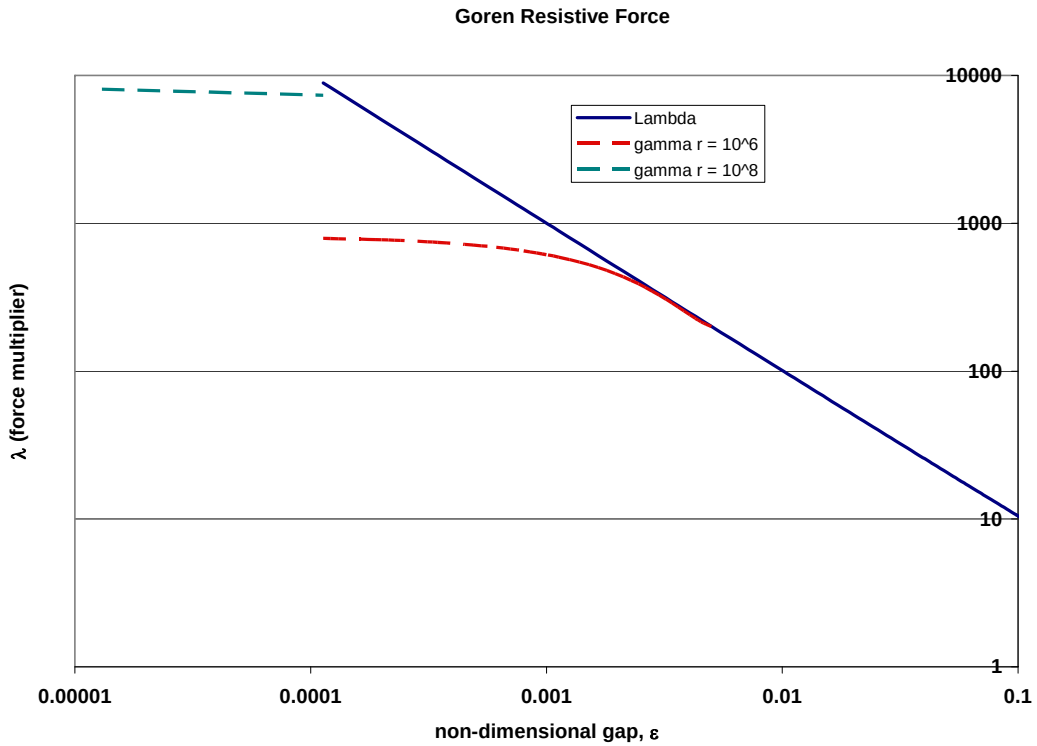

Figure 7-2. Predictions of Goren's corrective force for permeable surfaces.

perpendicular to the membrane wall

$$F_{net,\perp} = \tfrac{1}{2} C_d \rho_f A V_{s,i}^2 - 6\pi\mu b V_p(\lambda - 1) \tag{7-16}$$

where the first term on the RHS is generally pushing the particle to the wall due to the permeate velocity and the second term accounts for the repulsive nature of the permeable wall.

7.2.4 Lift force

A lift force is developed on a particle in the near-wall region due to fluid shear. Two different expressions are used to evaluate the lift force depending on the distance between the particle and the wall. If the Stokes length scale (ν/V_s) is less than the Saffman length scale ($\sqrt{\nu/G}$), where *G* is the wall normal velocity gradient, then Equation 7-17 from Cherukat and McLaughlin is used. Equation 7-17 does not suffer from the limitations imposed by Saffman's expression (i.e. that the Reynolds number based on the slip velocity be much less than the square root of the shear based Re) and is valid when the particle distance is less than the expression $\min\left\{\nu/u_s, \nu/\sqrt{\partial u/\partial x_i}\right\}$.

$$f_{lift} = \frac{-\rho_f b^2}{m_p}\left\{\begin{array}{l}\left[1.7631 + 0.3561\kappa - 1.1837\kappa^2 + 0.845163\kappa^3\right] \\ -\left[\dfrac{3.24139}{\kappa} + 2.676 - 0.8248\kappa - 0.4616\kappa^2\right]\Lambda \\ +\left[1.8081 + 0.8796\kappa - 1.9009\kappa^2 + 0.98149\kappa^3\right]\Lambda^2\end{array}\right\} \tag{7-17}$$

where $\kappa = h_p/b$, $\Lambda = \dot{\gamma} b / V_s$, and $\dot{\gamma}$ is the strain rate and V_s is the slip velocity. Otherwise, the lift force expression is taken from Wang et al. and is given by:

$$f_{lift} = \frac{3\pi\rho_f b^2 V_s}{32}\left(6V_s - 11Gh\right) \tag{7-18}$$

where all the variables have been defined previously.

7.2.5 Motion of particles

The equation of motion for the particles is:

$$\frac{du_{p,i}}{dt} = F_{drag} + F_{lift} + F_{vdW} + F_{EDL} + \frac{1}{2}\frac{\rho}{\rho_p}\frac{d}{dt}\left(u_i - u_{p,i}\right) + \left(\frac{\rho}{\rho_p}\right) u_{p,j}\frac{\partial u_i}{\partial x_j} \tag{7-19}$$

where the drag and lift force on the particle are given by Eqs. 7-5 – 7-7, and the electric double layer and van der Waals forces are given by Eqs. 7-6 and 7-7, respectively. The last two terms on the RHS of Equation 7-19 represent the force required to accelerate the fluid surrounding the particle and the effects of the pressure gradient on the undisturbed flow.

Integration of Equation 7-19 yields the position of the particle. The particle-fluid interaction is included in the flow field equations. If the particle reaches the membrane surface, it is "trapped" and particle tracking is terminated for that particle. No re-entrainment or resuspension of the particles that are trapped on the wall due to the wall shear stress is included. No particle-particle interaction is considered, thus in the simulation each particle is released independently and tracked until the particle either escapes the domain, is trapped by the membrane, or the maximum number of integration stepa were exceeded.

7.3 Model Domain Description

The generalized model geometry is shown in Figure 7-3, with the surface of the membrane shown in Figure 7-4. Fluid enters the domain through a feed channel on the left, passes through the feed channel, and exits on the right.

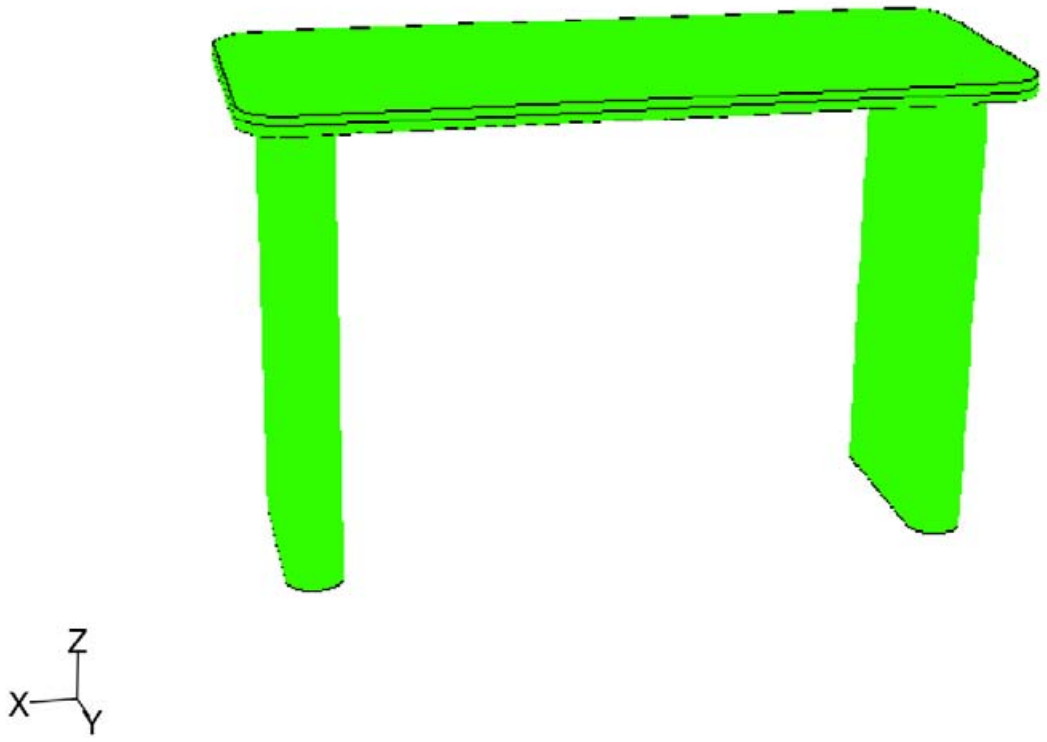

Figure 7-3. Generalized modeled geometry for all cases.

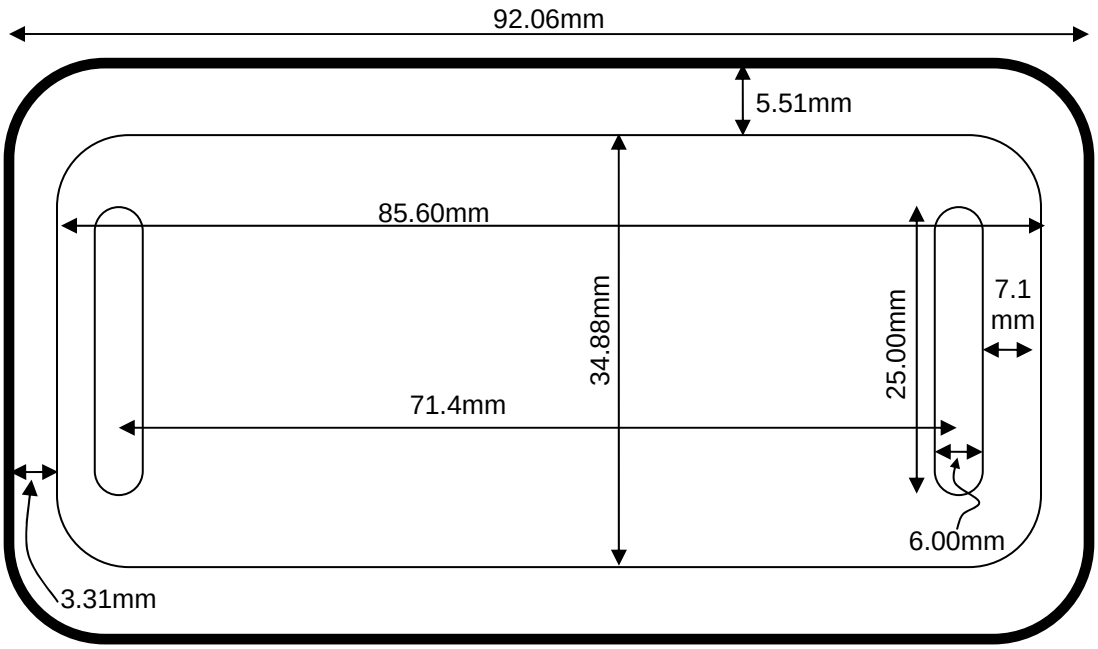

Figure 7-4. Schematic and dimensions of the flow cell. Membrane chevrons are not shown.

Simulations have been run for three different membrane surfaces: one surface with no chevrons (base case) and two different chevron configurations as shown in Figure 7-5. The chevron configuration has 7 lines of chevrons with 7 peaks per line. The wavelength of the chevrons is 4.29 mm. The angle of the chevrons is 90˚ and the spacing between rows is 8.6 mm. The height of the chevron into the channels is 0.5 mm and the width of the chevrons is 0.25 mm. Refer to Figure 3-1 for an explanation of the parameters describing the chevron configurations. The only difference between the two chevron configurations chosen for this study is that one is in-phase (Figure 7-5A) and the other is out-of-phase (Figure 7-5B). These two designs are the median designs used in the cross-flow experiments (Section 3). Preliminary results have been presented by Webb (2008) and James and Webb (2008).

In order to automate the simulation of a membrane with chevrons, a membrane template has been developed for the membrane flow cell geometry that is used in the experimental portion of this project. Once these parameters are specified, the problem geometry, fluid mesh, and appropriate boundary conditions are defined, and appropriate FLUENT input files are constructed. The FLUENT flow simulation is automatically run and post-processed including parameters such as the salt rejection coefficient of the membrane including the chevrons (Fluent, 2008).

7.4 Simulation Results

Initial simulations were performed for each case with flow only (no particles) to establish steady-state flow and salt concentration fields. The feed inlet ia a brine solution with 1 wt % salt at a flow rate of 4.8 g/s. The membrane characteristics used for the simulations are for the DOW FILMTEC BW30-400 membrane. The water permeation factor (A) is 8.07 x 10^{-12} m/s-Pa while

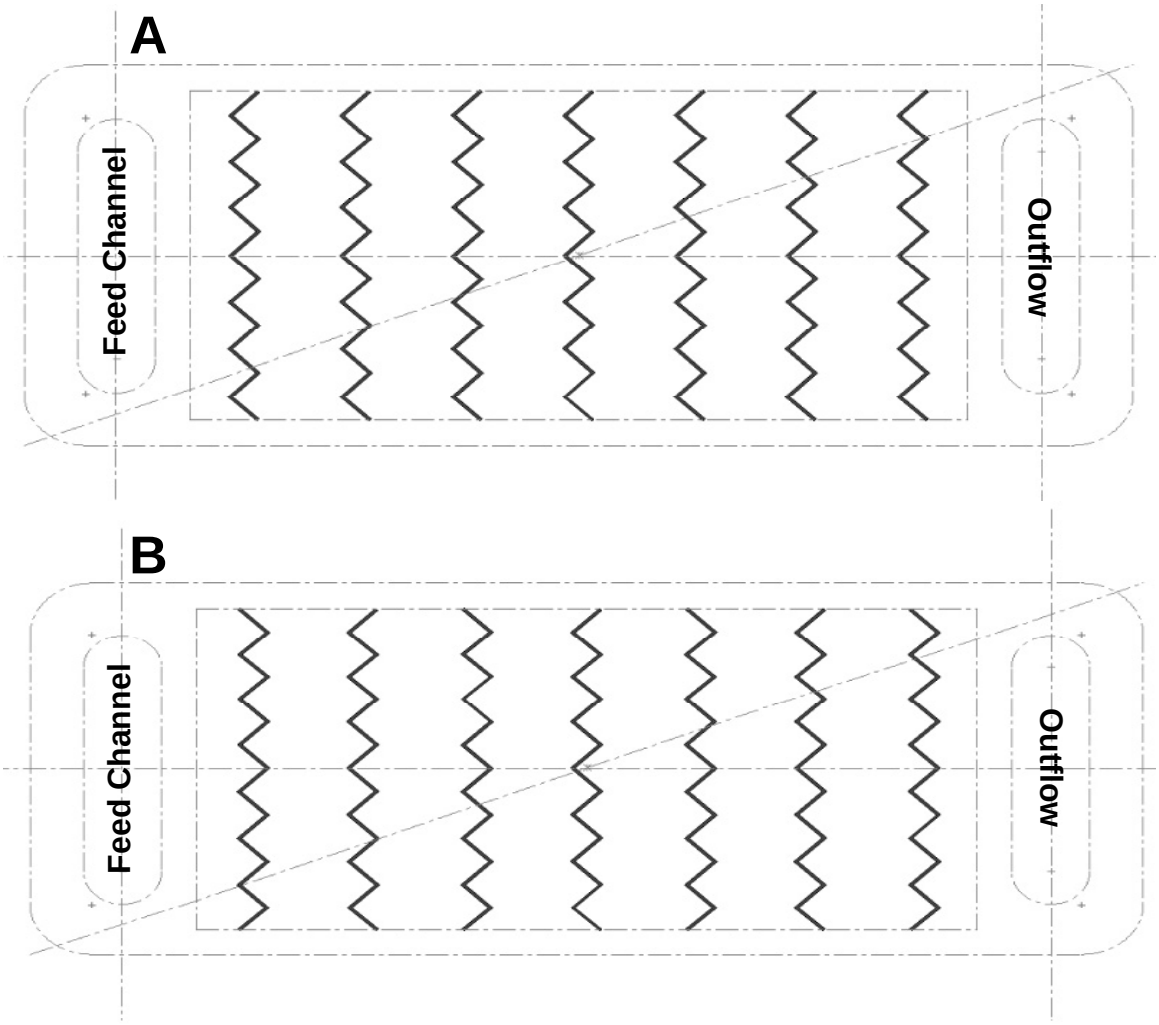

Figure 7-5. In-phase (A) and out-of-phase (B) chevron configuration on RO membrane. Chevron height is 5 mm

the salt factor (B) is 6.29 x 10^{-8} m/s. The osmotic pressure is modeled as linear with concentration with a constant of about 69,000 Pa-m^3/kg. Once a steady flow field is established, 1-micron diameter spherical particles are released from the inlet and tracked as described above. Initially simulations of the three cases were run with all forces included in Equation 7-19. Approximately 8000 particles were released into the flow field for each of the cases considered. The results for all of these simulations were such that all of the particles were incomplete. Upon further investigation, it turned out that several terms in Equation 7-19 and the integration scheme of Fluent caused the problem. As can be seen in Figure 7-2, the repulsive force becomes quite large as the particle-wall distance becomes small. The permeate drag force that pushes the particle to the wall is also reduced as the is the distance becomes small. When Fluent tries to numerically integrate Equation 7-19, the particle position oscillates resulting in the selection of extremely small time steps to track the position of the particle thereby increasing the number of iterations.

In order for particles to reach the wall, the net repulsive force given by Equation 7-15 was not included in the final simulations. As reported by Kleinstreuer (2006), inclusion of this repulsive force prevents particle-wall contact. Kleinstreuer subsequently developed a near-wall residence time parameter to characterize the potential for particle deposition based on particle trajectories within 50 μm of the wall. In the present set of simulations, the net repulsive force is neglected in order to achieve deposition of particles on the wall. The problem of simulating particle-wall deposition needs further investigation.

Figures 7-6 – 7-8 show the deposition pattern of the particles on the membrane surface where the flow goes from left to right. The results are also summarized in Table 7-1.

For the no chevron case, there is some particle deposition near the inlet and outlet due to the flow changing directions, but essentially none on the membrane surface. Only 0.25% of the particles are trapped in this case. For cases with chevrons, particle deposition is higher for the out-of-phase chevron configuration (4.6% trapped) compared to the in-phase case (2.3% trapped). These results are inconsistent with the numerical results reported in Ho et al., (2008) (Section 2) and with the experimental data shown in Section 3. In addition, the location of particle deposition modeled in this study differs from the biofouling pattern observed in the experiments described in Section 3 and the biofouling predicted by Ho et al. (2008) (also described in Section 2). In that numerical study, biofouling is correlated with the local shear stress. Lower shear stress occurs downstream of a "V" opening in the *downstream* direction, so increased biofouling is predicted in this region. In contrast, our study predicts greater deposition and biofouling where the "V" is opening in the *upstream* direction (Figure 4 in Section 2).

The differences between the biofouling simulations of Ho et al. (2008), and the present computations are significant. Both approaches use computational fluid dynamics, but they differ in the approach to predicting biofouling. Ho et al. (2008), assumes that biofouling is correlated with the local wall shear stress. Based on the experimental data, there seems to be a reasonable correlation. However, as shown by Longest and Kleinstreuer (2003), correlation with wall shear stress alone does not adequately predict particle deposition in a number of situations. Therefore, the more mechanistic approach of particle tracking, which was shown to be an improvement over wall shear-stress models by Longest and Kleinstreuer (2003) was implemented.

Table 7-1. Results from particle tracking simulations with no repulsive force.

Case	Tracked	Escaped	Aborted	Trapped	Incomplete	% trapped*
No Chevrons	8024	7080	0	18	926	0.25
In-Phase Chevrons	8024	6006	0	143	1875	2.3
Out-of-Phase Chevrons	8024	5776	0	279	1969	4.6

* - % trapped is defined as the number trapped divided by the number tracked minus incomplete.

The disagreement between the model results and the experimental data points to missing physics in the particle tracking model. Two areas come to mind 1) the exclusion of near-wall particle forces as discussed in Section 6.4 and 2) resuspension.

Other particle tracking efforts similar to those described in this study have noted that when the near-wall repulsive forces are included in the particle force balance, particle-wall contact will not

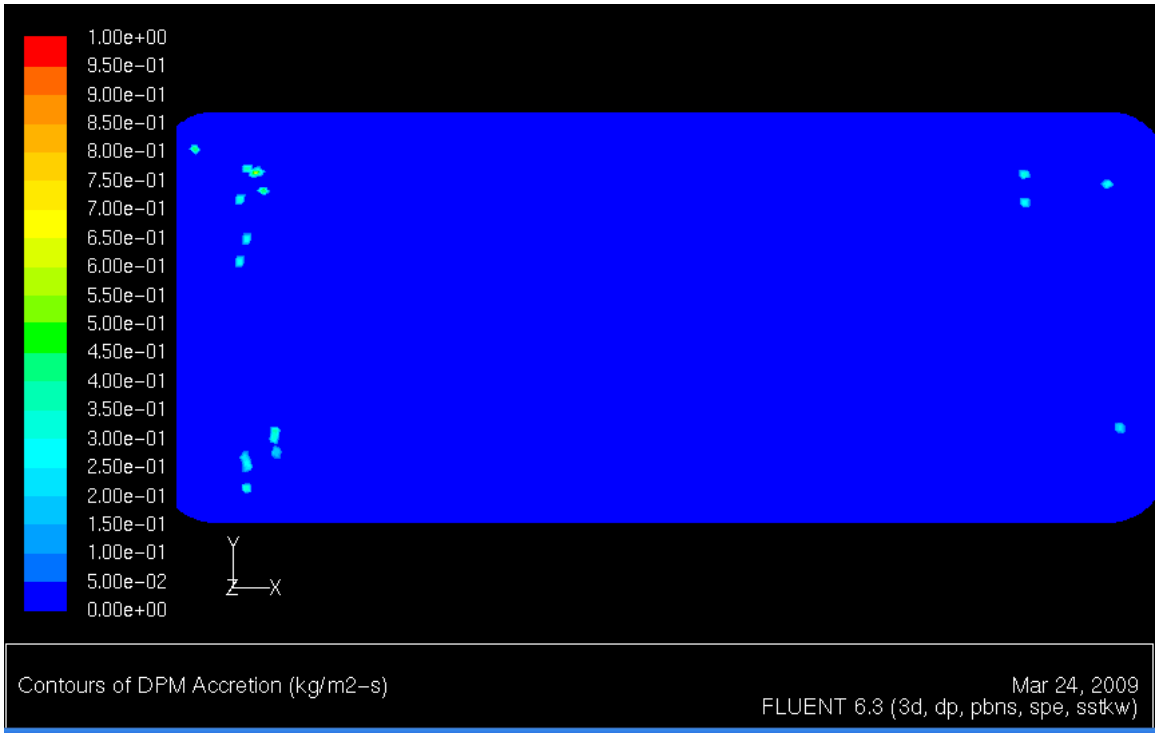

Figure 7-6. Particle tracking results for no chevron case.

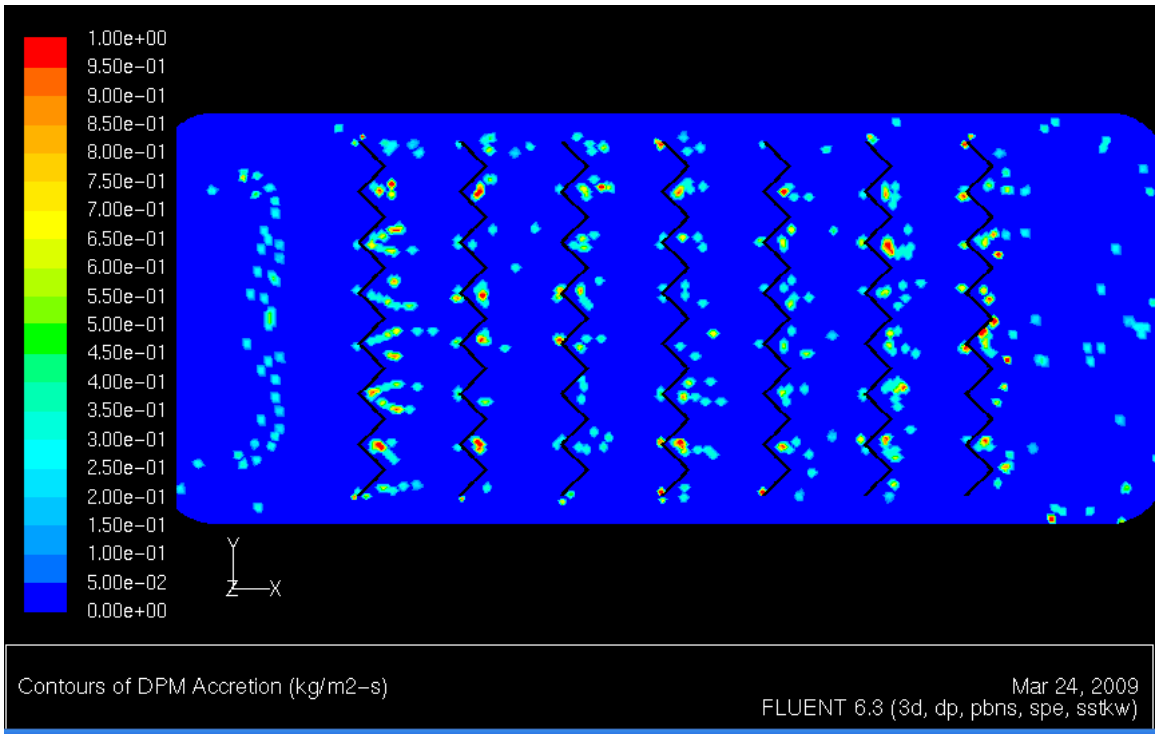

Figure 7-7. Particle tracking results for in-phase chevron case.

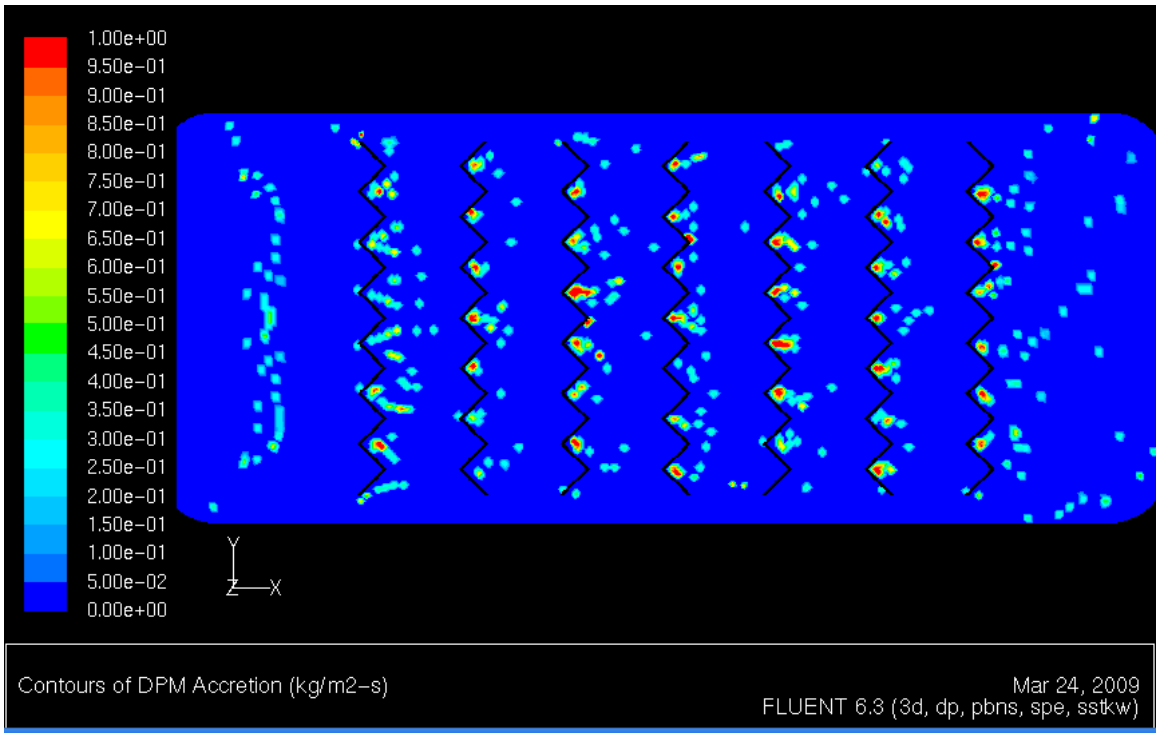

Figure 7-8. Particle tracking results for out-of-phase chevron case.

occur (Kleinstreuer, 2006) similar to our experience. In response to these observations, Longest and Kleinstreuer (2003) developed a Near Wall Residence Time (NWRT) approach that quantifies the effect of particles that approach the wall within a number of particle diameters. The form of the NWRT parameter includes a number of variables that need to be fit to experimental data. Longest and Kleinstreuer (2003) fit these variables to experimental data for blood platelet deposition in transient laminar flow conditions. Obviously, these parameters may not apply to our current configuration that includes turbulent flow conditions, so the NWRT approach has not been used in the present investigation.

Longest and Kleinstreuer (2003) also evaluated the effect of not including the near-wall forces in the particle tracking scheme similar to the final approach described above. While these data-model comparisons are not as good as the NWRT approach, the modeling results without the near-wall forces compare reasonably well to the experimental data. While there are areas of significant disagreement, the model results downstream of an abrupt expansion compare well to the experimental data. The abrupt expansion geometry is similar to that which occurs for flow over a chevron. The results of Longest and Kleinstreuer (2003) provide confidence that the present approach of excluding near-wall particle forces is reasonable.

The second possible reason for the discrepancy in the predicted particle deposition and the observed biofouling for the cases with chevrons is the lack of a re-entrainment or resuspension model. The area downstream of the convergent chevrons is a region of high shear as noted earlier, so any particles that reach the surface may not remain trapped due to the high local fluid shear. Re-entrainment should be considered in any future work on this problem and is a possible cause for the large disagreement.

Additional forces that are not included in the present particle tracking scheme but that might influence the results include turbulent deposition and modification of the drag parallel to the membrane surface due to the presence of a wall. The present model used a steady-state flow field to track the particles. Using a transient flow field would change the results due to the unsteady nature of turbulent flow. In addition, the particle tracking approach assumes inert particles, where the experiments described in Section 3 use bacteria. The use of bacteria leads to addition complexity in the system as well as variability in results that the particle tracking method does not capture. In conclusion, particle tracking is still considered to be a reasonable approach to predicting biofouling because particle tracking has been shown to predict particle deposition by Longest and Kleinstreuer (2003) among others. However, the inclusion of additional phenomena such as re-entrainment or resuspension should be explored in any future work. These additional factors would be expected to significantly improve the predictions.

7.5 References

Brenner, H., (1961) The slow motion of a sphere through a viscous fluid towards a plane wall. Chemical Engineering Science. 16, 242-251.

Cox, R.G., Brenner, H., (1967) The slow motion of a sphere through a viscous fluid towards a plane surface-II Small gap widths, including inertial effects. Chemical Engineering Science. 22, 1753-1777.

Fluent, Inc., 2006a, (2006) FLUENT 6.3 User's Guide.

Fluent, Inc., 2006b, (2006) Desalination UDF.

Fluent, Inc., 2007, (2007) User's Guide – Template for Desalination Membrane.

Goren, S., (1979) The hydrodynamic force resisting the approach of a sphere to a plane permeable wall. J. Colloid and Interface Science, 69(1) 78-85.

Ho, C. K., S. J. Altman, H. D. T. Jones, S. S. Khalsa, L. K. McGrath, and P. G. Clem, (2008) Analysis of micromixers to reduce biofouling on reverse-osmosis membranes. Environmental Progress, 27(2), 195-203.

James, D., and S. Webb, (2008) Particle Tracking for Membranes Including Filtration, Division of Fluid Dynamics Annual Meeting, The American Physical Society, San Antonio, TX, November 23-25.

Kang, S-T, Subramani, A., Hoek, E.M.V., Deshusses, M.A., and Matsumoto, M.R., (2004) Direct observation of biofouling in cross-flow microfiltration: mechanisms of deposition and release. J. Membrane Science 244, 151-165.

Kleinstreuer, C., (2006) BIOFLUID DYNAMICS – Principles and Selected Applications, CRC Press, Taylor and Francis, Boca Raton.

Longest, P.W., and C. Kleinstreuer, (2003) Comparison of blood particle deposition models for non-parallel flow domains. J. Biomechanics. 36 421-430.

Morsi, SA and Alexander AJ, (1972) An investigation of particle trajectories in two-phase flow systems. J. Fluid Mech. 55(2) 193-208.

Rautenbach, R. and R. Albrecht, (1989) Membrane Processes. John Wiley & Sons.

Song, L., J.Y. Hu, S.L. Ong, W.J. Ng, M. Elimelech, and M. Wilf, (2003) Emergence of thermodynamic restriction and its implications for full-scale reverse osmosis processes. Desalination. 155 213-228.

Song, L., and K.G. Tay, (2006) Performance prediction of a long crossflow reverse osmosis membrane channel. J. Membrane Science. 281 163-169.

Wang, Q., Squires, K.D., Chen, M. and McLaughlin, J.B., (1997) On the role of the lift force in turbulence simulations of particle deposition, Int. J. Multiphase Flow. 23(4) 749-763.

Webb, S.W., (2007) Preliminary MIOX Recovery Results for Change in Water Permeation Parameter. Sandia internal report April 10, 2007.

Webb, S.W., (2008) Biofouling Potential of RO Membranes including Micromixers. IWA Biofilm Technologies Conference, Singapore, January 8-10, 2008.

This page is intentionally left blank

8 OPTIMIZATION OF MICROMIXER DESIGN TO MINIMIZE BIOFOULING

Amy C. Sun, Stephen W. Webb, and William E. Hart

8.1 Introduction

The goal of this project is to find the optimal micromixer design to minimize biofouling. Both experimental (Sections 2 – 4.5) and numerical studies (Sections 2 and 6 – 7) have been conducted to reach this goal. Experimentally and with numerical sensitivity studies, only a small subset of the potential designs can be tested. This Section describes an automated search algorithm for geometries that either maximizes fluid mixing while minimizing the area covered by the chevrons (GOMA study) or maximizing the trans-membrane flux (FLUENT study). The computational domain is modeled after a laboratory-scale flow cell that is used to collect experimental data for various surface designs (Sections 2 and 3). The trade-off between the available membrane area for filtration and enhanced mass transfer due to the micromixers is evaluated by coupling the CFD model to an optimization algorithm.

Two numerical studies have been conducted, one two-dimensional (2D) and the second three-dimensions (3D). The two-dimensional representation uses GOMA (Schunk et al., 2002) for the CFD calculations, where as the three-dimensional representation uses FLUENT (*Fluent, Inc.*, 2006). The tradeoff between the available membrane area for filtration and enhancement in mass transfer due to enhanced mixing is evaluated by coupling the CFD model to an optimization algorithm. The objective of work is to demonstrate the coupling between a rigorous, parallel CFD analysis tool and a parallel optimization tool, which has not been carried out for this type of application. With improvements in the model described in Section 7 it is anticipated that the automated search algorithm for geometries will be used to minimize the number of particles that attach to the membrane surface.

8.2 Optimization of Mixer Design in 2D Flow Channel using GOMA and DAKOTA.

Figure 8-1 is a schematic of the flow cell as viewed from the top. Fluid enters the 2D domain through a feed channel on the left, passes the plenum before it exits on the right. Figure 8-2 shows a side view, which represents the simulation domain. The embossed epoxy lines form ridges along the membrane surface, which in 2D are represented as hemispherical features within the fluidic channel. For the model, the permeate flow is assumed to be small relative to the bulk flow; hence, the membrane is assumed impermeable in the 2D simulation. There are two channel heights that have been simulated for the problem, 1 mm, as shown in Figure 8-2, and 2.5 mm.

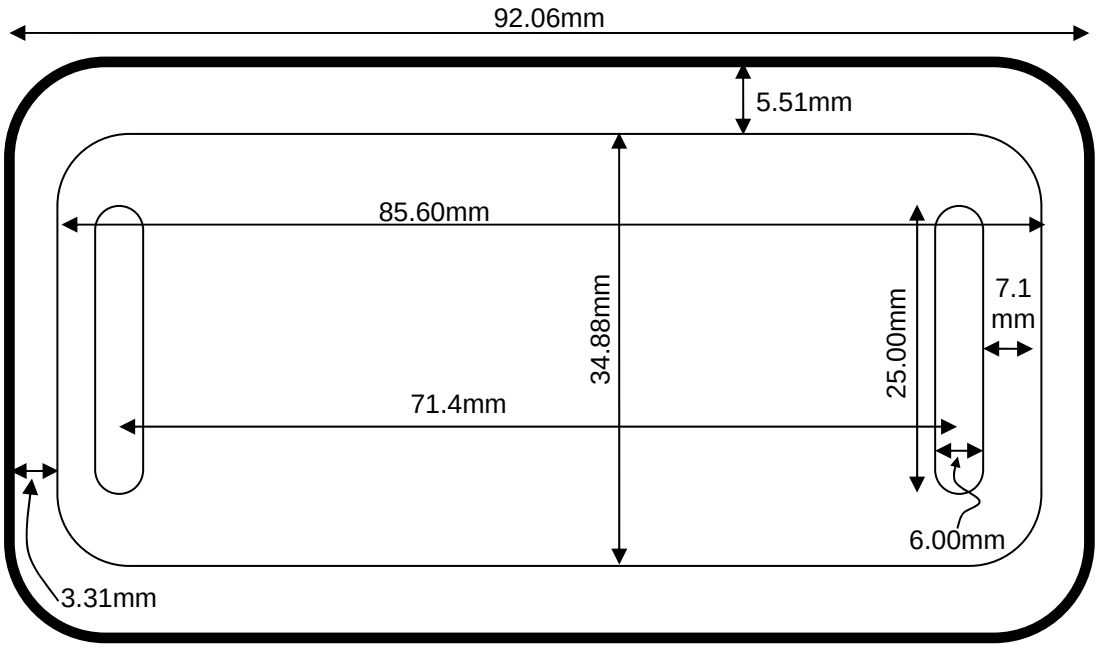

Figure 8-1. Schematic and dimensions of the flow cell. Membrane chevrons are not shown.

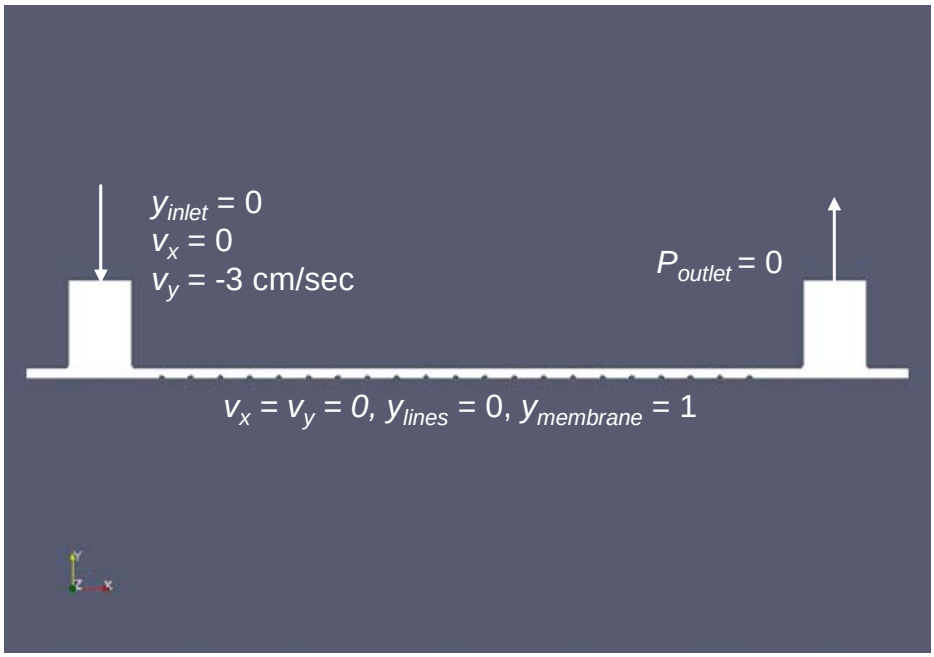

Figure 8-2. Two dimensional side view of the flow cell with chevrons (seen as lines in 2D).

Navier-Stokes equation, equation of continuity, and species balance are solved for the model using GOMA. GOMA is a finite-element based fluid dynamics code that specializes in multiphase, coupled-physics problems (Schunk et al., 2002). For the purpose of evaluating the extent of mixing, Dirichlet boundary conditions are set for mass transfer, meaning the mass fraction is set to one on the membrane side and zero everywhere else (except the exit). The boundary conditions for the momentum balance are also listed in Figure 8-2. In addition to the fluid boundary conditions, the fluid properties are defined by $\rho = 1$ cm^3/gm, $\mu = 1.$ poise, and D

= 0.025 cm^2/sec. The Peclet number, a dimensionless group reflecting the relative magnitude between convective and diffusive forces in a mass transfer problem, is on the order of 10^3; i.e.,

$$Pe = \frac{\langle v \rangle L}{D} = \frac{(3)(7.1)}{(0.025)} = 852 \tag{8-1}$$

Even though the diffusivity of the material is considered large relative to self-diffusivity of water molecules (2.7×10^{-5} cm^2/sec), the resulting Peclet number indicates a convection-dominated problem.

8.2.1 Optimization Description

The amount of epoxy lines (chevrons in 2D) embossed on the membrane is based on two parameters, the diameter of the lines *d* and the percentage of coverage on the membrane *p*. While maximizing mixing may not correlate directly with minimizing biofouling, it is well known that an improvement in microfluidic mixing leads to savings in process time for fluidic delivery systems due to enhancement in mass transfer (Brotherton et al., 2006).

For this study, the objective function contains two parts, a metric for enhanced mixing, and a metric for area of coverage.

$$\begin{aligned} &\max_{d,\,p} \quad F(d,\,p) \\ &s.t. \quad d_{\min} < d < d_{\max} \\ &\qquad 5\% < p < 50\% \\ &where \\ &F(d,\,p) = \frac{\Delta y_{flux}}{\Delta y_{flux0}} + (1 - 0.01p) \end{aligned} \tag{8-2}$$

The change in species flux between inlet and outlet, Δy_{flux}, is normalized against the change of species flux when the channel contains no lines, Δy_{flux0}. The lower and upper bounds (d_{min} and d_{max}) are 0.5mm and 1.5mm for the 1mm-gap channel and 1mm and 3.75mm for the 2.5mm-gap channel. Note that in the absence of epoxy lines, the objective function reduces to two; i.e., $F_0 = 1 + 1 = 2$. The species flux is calculated at the end of each steady-state run. Both of the convective and diffusive fluxes are accounted for in the objective function.

$$\begin{aligned} &convective\ flux \quad \int \rho (n \bullet v) y \, dA \\ &diffusive\ flux \quad \int -D(n \bullet \nabla y) dA \end{aligned} \tag{8-3}$$

where ***n*** is the normal vector emanating from the exit boundary. The optimization problem is solved via DAKOTA, an in-house optimization code. DAKOTA consists of multiple state-of-the-art optimization and uncertain quantification algorithms that are readily accessible via user-

defined interface routines (Eldred et al., 2002). Furthermore, DAKOTA is designed to interface with large-scale simulations that run on high performance computing platforms.

When solving the model based on finite-element analysis, the domain of interest must be meshed. Because the channel gap is small relative to the entrance region, the mesh generated via the default scheme may not capture enough resolution in the channel region. For this study, all of meshing is carried out by CUBIT, a Sandia software for mesh generation (Mitchell et al., 2002). Three output variables are monitored while conducting mesh convergence study: the outlet species flux, the average outlet concentration, and the shear stress. The output converged on element size on the order of 0.1mm, or ten elements across the gap. Table 8-1 summarizes the values of the model as a function of the number of elements across the channel gap.

Table 8-1. Mesh refinement study for the 1mm-gap 2D model.

# elements	Y_flux	Shear stress	Avg y
2	0.2487	-7.05×10^4	0.0327
5	0.857	-7.14×10^4	0.0626
8	0.878	-7.16×10^4	0.0633
*10	0.878	-7.18×10^4	0.0632
11	0.878	-7.18×10^4	0.0632

Unless noted, the subsequent flow simulations are based on a resolution that yields at least ten-elements across the channel.

8.2.1 Coupling between GOMA and DAKOTA

Once the two-dimensional model has been finalized, it is interfaced with the optimization routine. Figure 8-3 shows the schematic of how the CFD model and the optimization algorithm are coupled. CUBIT and GOMA constitute an inner loop of the optimization problem, where they execute a prescribed set of input variables given by DAKOTA to obtain the appropriate mesh and objective function. The calculated objective function exits the inner loop to be evaluated by DAKOTA.

There are two simple routines to pass the information between the two loops. For each optimization loop, the routine *i_filter.f* takes the geometric parameters and converts them to a format that can be integrated into the mesh input file while *o_filter.f* processes the species flux and formats the objective function that is readable by DAKOTA. The inner and outer loops are all managed by shell scripts (Simmermacher, T., Personal Communication, March, 1999).

Once interfaced correctly, additional parameters are defined to run the optimization problem: the optimization approach, step size and tolerance. For this study, a non-gradient based optimization algorithm is preferred over gradient-based optimization method. This is due to occasional failure of inner loop routines, where either the mesh cannot be generated or no convergence is achieved for a steady-state calculation. This failure in the inner loop can jeopardize calculations of feasible search directions within the optimizer. Hence, non-gradient based routines, where the topology of the objective function need not to be continuous, are preferred for this problem.

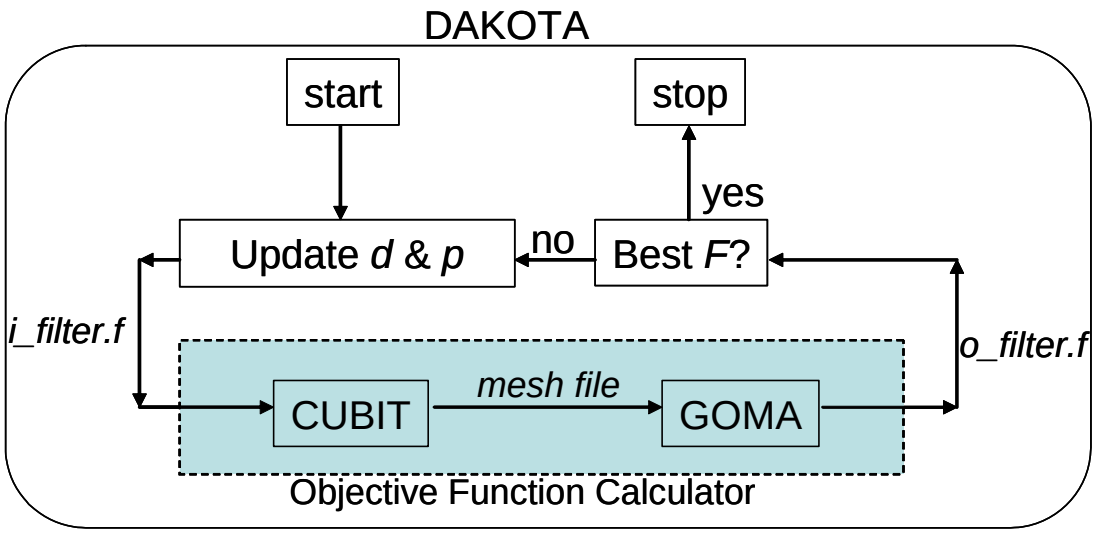

Figure 8-3. Simple schematic of DAKOTA-GOMA coupling.

Nevertheless, a flawless execution of the optimization problem requires flawless objective function evaluations. In cases where no convergence is sought for the steady-state problem, a false objective function is given to keep the optimizer functional.

8.2.2 Discussion

Figures 8-4 show mass fraction and velocity profiles of a typical simulation run. The optimization iteration history with respect to each of the two design parameters are shown in Figure 8-5. The objective functions of failed runs are intentionally set to be lower than the converged runs in order to avoid false search directions, which result in some solutions clustered around $\boldsymbol{F}<1$. The final optimal solution resides near the lower bounds of both parameters, 0.521mm and 5%, indicating smaller line size with least coverage are best. In Figure 8-5b, the linear dependence of the $\boldsymbol{F}$ relative to the percentage of covered area is apparent. The iteration histories for the 2.5mm-gap optimization runs are similar and not shown. The probable cause for poor convergence during function evaluation is due to the large flow within the channel. Alternatively, transient runs would be more stable and guarantee convergence, but the cost in time may become prohibitive for optimization runs where hundreds of function evaluations are required.

Note that the maximum objective function sought is not an improvement over a channel with no lines, which takes on a value of $\boldsymbol{F} = 2$. This is due to the way the concentration is defined initially, which is dependent upon the area of uncovered membrane. The mass available for mixing should be consistent in every function evaluation so the extent of mixing becomes a true measure of the system's response.

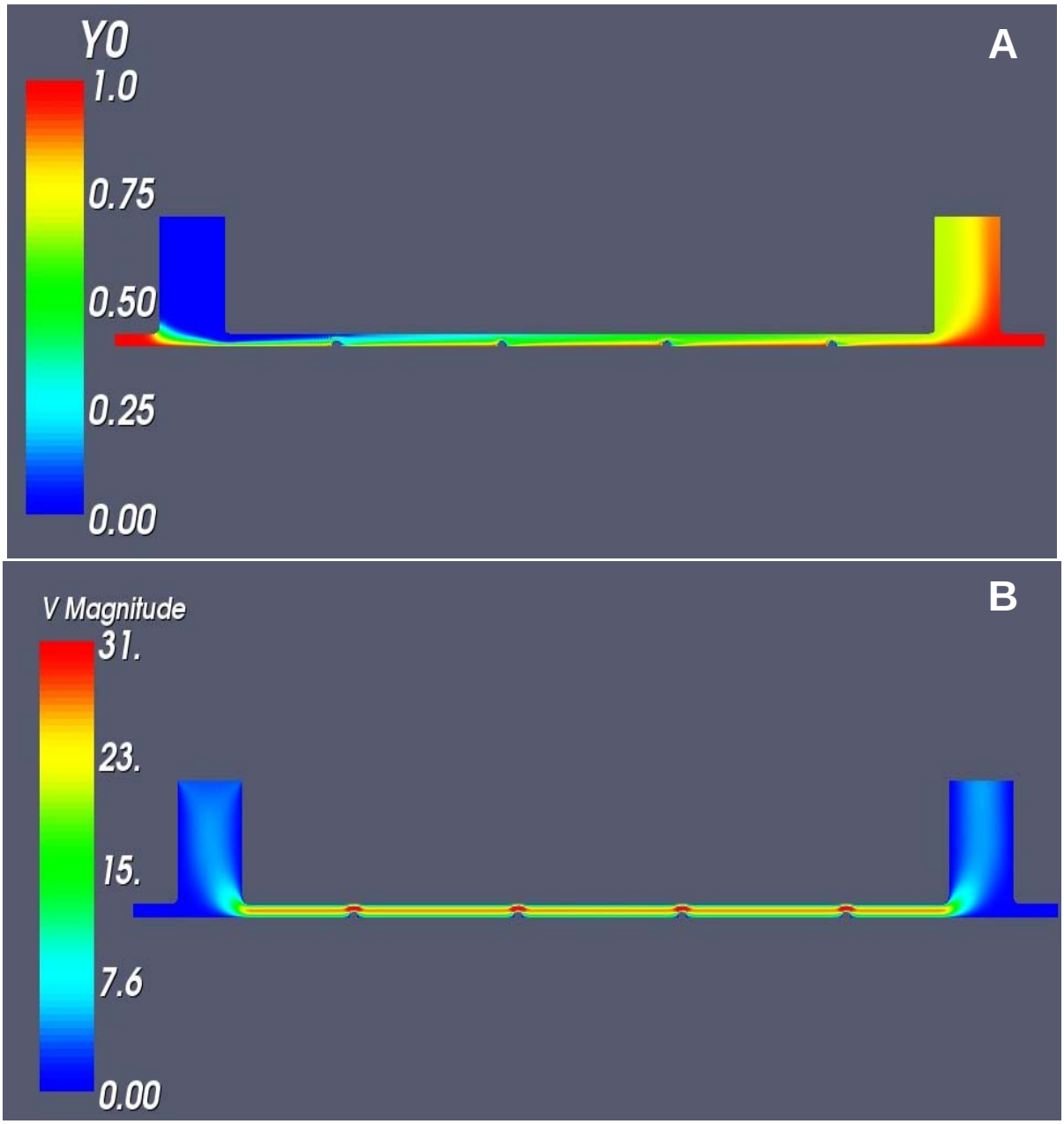

Figure 8-4. Mass fraction (A) and velocity (B) profiles of a 1-mm channel simulation.

8.3 Optimization of Mixer Design in 3D Flow Channel using FLUENT and DAKOTA.

8.3.1 Membrane Description

The membrane geometry studied in 2D is further extended to 3D in order to incorporate transmembrane flux in the calculations described in section 6.1. As such, the optimization

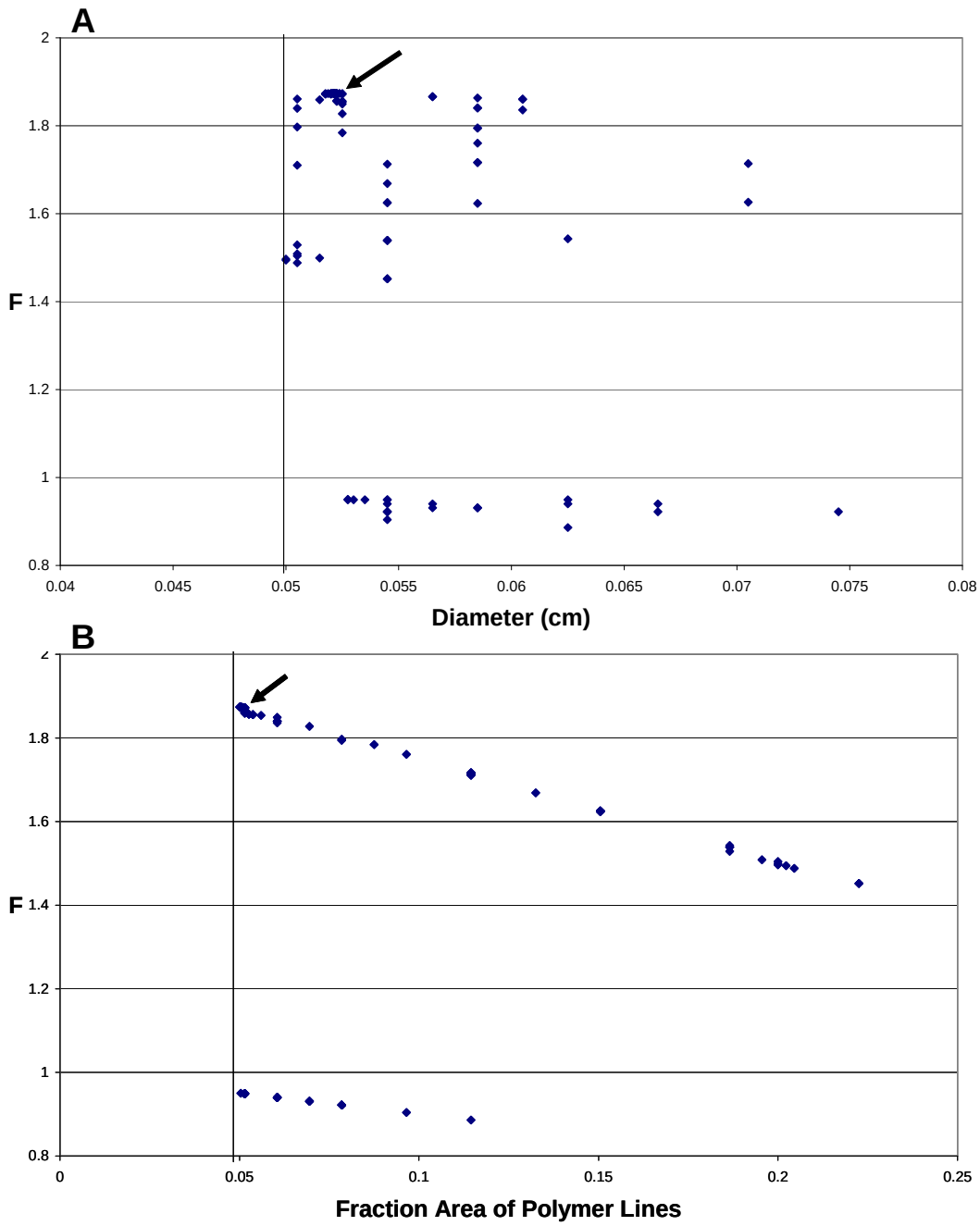

Figure 8-5. Optimization history as a function of line diameter (A) and area coverage (B). Simulations used a 1-mm channel depth.

problem is again solved using coupled FLUENT-DAKOTA model. The 3D computational domain identical to Figure 7-3 is used and meshed for this purpose.

Navier-Stokes equation, equation of continuity, and species balance are solved for the model and its modification to resolve trans-membrane flux [Webb, 2006]. The boundary conditions for velocity and species equations are further extended to accommodate full 3D domain.

Various geometric constants are specified to create the *3D* chevrons on the membrane. The process for creating the mesh requires multiple steps. First, geometric constant file is defined in the *inputfile.txt* and processed to yield a mesh definition file that can be executed in GAMBIT. The constants specified by the users include the following (refer to Figure 3-1 for an explanation of the parameters describing the chevron configurations):

- chevron height,
- chevron width,
- number of chevron peaks on a line,
- spacing between lines,
- distance to leading edge,
- chevron amplitude,
- direction of chevrons (in-phase or out-of-phase).

Second, the membrane definition file is created and further processed by GAMBIT. A failed mesh will yield an external warning file from GAMBIT (*warning.txt*). This is important for the optimization routine as the existence of such warning file is the sole indicator of whether FLUENT will be launched.

8.3.2 Optimization Description

Figure 8-6 shows the schematic of how DAKOTA is coupled to the FLUENT. The geometric constants defined in *inputfile.txt* have been further abstracted into *inputfile.template* and *params.in* which allows DAKOTA to dictate the changes in chevron geometry within its own framework. This was a necessary step in coupling the two codes. FLUENT returns with the apparent rejection coefficient, which becomes the objective function value for the optimizer. The optimization can be run in parallel asynchronously. FLUENT parallelization is run on either *layla* or *gramma*.

Table 8-2 shows the results of a complete DAKOTA-FLUENT run and the associated apparent salt rejection coefficient, R_{app}. [Rautenbach, 1989].

$$R_{app} = 1 - \frac{\rho_{s3}}{\rho_{s1}} \tag{8-4}$$

where ρ_{s1} is the bulk salt concentration and ρ_{s3} is the permeate salt concentration. The seventh evalutation yields the parameters which the highest apparent salt rejection coefficient, or the lowest transmembrane concentration ratio. This is consistent with the earlier recommendation by manual evaluation. A value d = 1 defines lines pointing towards the outlet. The tenth evaluation shows an unrealistic objective function. This is a case where the mesh program did not provide an adequate mesh and FLUENT run was automatically bypassed. This failure mechanism must be programmed in DAKOTA or the optimization run grinds to a halt. The incomplete mesh and the subsequent failure-capture scheme have also been implemented in an earlier study involving 2D membrane flow optimization, hence reflecting the inherent challenge associated with optimization of complex flow (and geometry) problems.

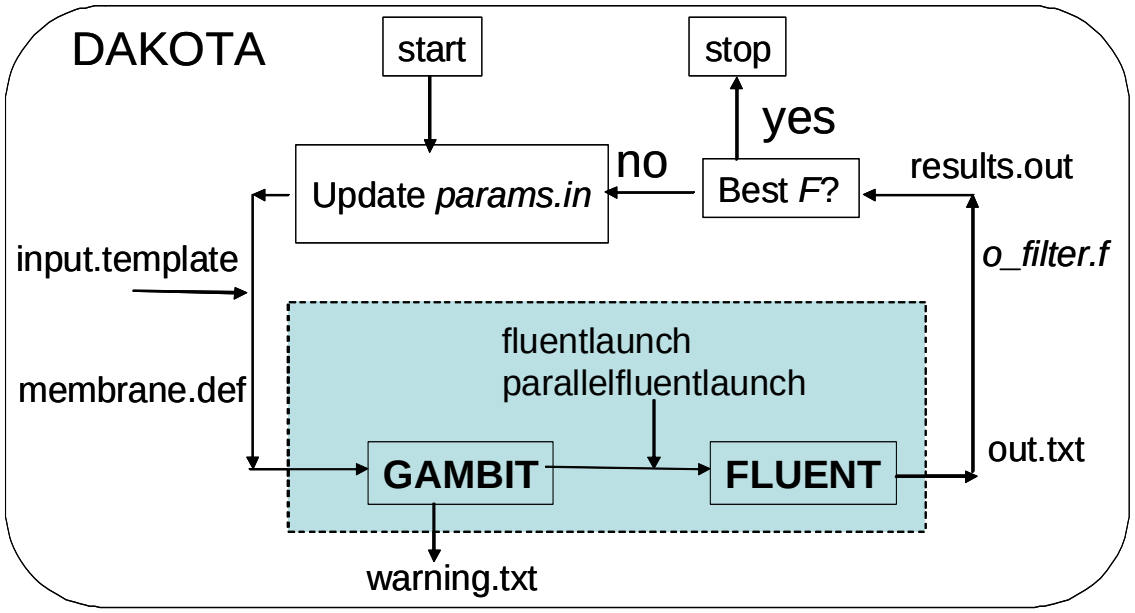

Figure 8-6. Coupling schematic of DAKOTA-FLUENTcodes.

In this preliminary study, no gradient-based optimization algorithm has been implemented. When the mesh routines fail too often, the gradient information is corrupt and should not be used in these CFD applications.

Table 8-2. Summary of geometries that have been tested for highest salt rejection. In all of the runs, height = 0.25 mm, width = 0.3 mm, and the lines are out-of-phase.

%eval_id	#waves	spacing (mm)	amplitude (mm)	direction	objective func
1	4	15	5.36	1	0.9899
2	10	15	2.14	0	0.9884
3	10	6	2.14	1	0.9819
4	4	15	5.36	0	0.9819
5	10	15	2.14	1	0.9884
6	10	6	2.14	0	0.9806
7	10	15	1.05	1	0.9917
8	4	15	2.63	1	0.9914
9	10	6	1.05	0	0.9894
10	4	15	2.63	0	1000
11	7	6	2.14	1	0.9868

8.3.3 Discussion

Despite the various interruptions in coupling the two codes, a complete, fully coupled run between FLUENT and DAKOTA is automated in the 6310 cluster. The potential for this application is high given the number of high-fidelity models Sandia create. In this study, point-by-point algorithm is used to seek the mixer geometry that maximizes salt rejection. A gradient-based algorithm is not recommended unless there is confidence that each search point generates an acceptable finite-element mesh. The geometry that yields the highest apparent salt rejection coefficient have parameters that reflect a high number of waves, large spacing, and small amplitude.

8.4 References

Brotherton, C. M., Davis, R. H. Sun, A. C., Schunk, P. R., (2006) Mixing in polymeric microfluidic devices. Sandia National Laboratories, Albuquerque, NM. 35.

Eldred, M. S., Giunta, A.A., van Bloemen Waanders, B.G., Wojtkiewicz, J., Hart, W.E., Alleva, M.P., (2002) Dakota, a multilevel parallel object-oriented framework for design optimization, parameter estimation, uncertainty quantification, and sensitivity analysis, version 3.0, users manual. Sandia National Laboratories, Albuquerque, NM. 205.

Fluent, Inc., (2006) FLUENT 6.3 User's Guide. September.

Ho, C. K., Altman, S.J., Jones, H.D.T., Khalsa, S.S., McGrath, L.K., Clem P.G., (2008) Analysis of micromixers to reduce biofouling on reverse-osmosis membranes. Environmental Progress. 27 195-203.

Khalsa, S.S.S., Ho, C.K., (2008) Design optimization of anti-fouling micromixers for reverse osmosis membranes. paper presented at Water Reuse and Desalination. Dallas Texas. September 7-10.

Mitchell, S.A., Sjaardema, G.D., Tautges, T. J., Wilson, T. J., Owen, S. J., Blacker, T. D., Bohnhoff, W. J., Edwards, T. L., Hipp, J. R., Lober, T. R., (2002) Cubit mesh generation toolkit user documentation. Sandia National Laboratories, Albuquerque, NM.

Schunk, P. R., Sackinger, R.R., Rao, R.R., Chen, K.S., Baer, T.A., Labreche, D.A., Sun, A.C., Hopkins, M.M., Subia, H.K., Moffat, H.K., Secor, R.B., Roach, R.A., Wilkes, E.D., Noble, D.R., Hopkins, P.L., Notz, P.K., (2002) Goma 4.0 – a full-newton finite element program for free and moving boundary problems with coupled fluid/solid momentum, energy, mass, and chemical species transport: User's guide. Sandia National Laboratories, Albuquerque, NM. 262.

Rautenbach, R., Albrecht, R., (1989) Membrane Processes. John Wiley & Sons.

Simmermacher, T., (1999) Slot coating optimization. Sandia Internal Memo. March.

Webb, S.W., (2006) Simulation of the Pressure Drop and Flow in the MIOX Membrane Including Permeate Flow and Concentration Polarization. Sandia Internal Memo.

This page is intentionally left blank

DISTRIBUTION

Internal (Electronic Copy)

1 LDRD Office
1 Technical Library
1 J. Merson, 6730
1 C. K. Ho, 6731
1 L. Costin, 6731
1 S. W. Webb, 6732
1 D. J. Borns, 6732
1 R. Finley, 6733
1 S. Altman, 6736
1 M. Rigali, 6736
1 A. Sun, 6327
1 J. B. Kelley, 6327
1 S. Khalsa, 6337
1 J. Tillerson, 6337
1 M. Hibbs, 6338
1 J. Nelson, 6338
1 W. Hart, 1412
1 M. D. Rintoul, 1412
1 J. Johannes, 1810
1 R. Stinnett, 1821
1 P. Clem, 18152
1. A. Cook, 18152
1 W. Hammetter, 18152
1 H. Jones, 8622
1 A. Martino, 8622
1 L. K. McGrath
1 A. Sanchez

External (Electronic Copy)

1 M. Elemelech, Yale University
1 D. James, Texas Tech
1 M. Cappelle, University of Texas, El Paso